TECHNISCHE UNIVERSITÄT GRAZ

DIPLOMARBEIT

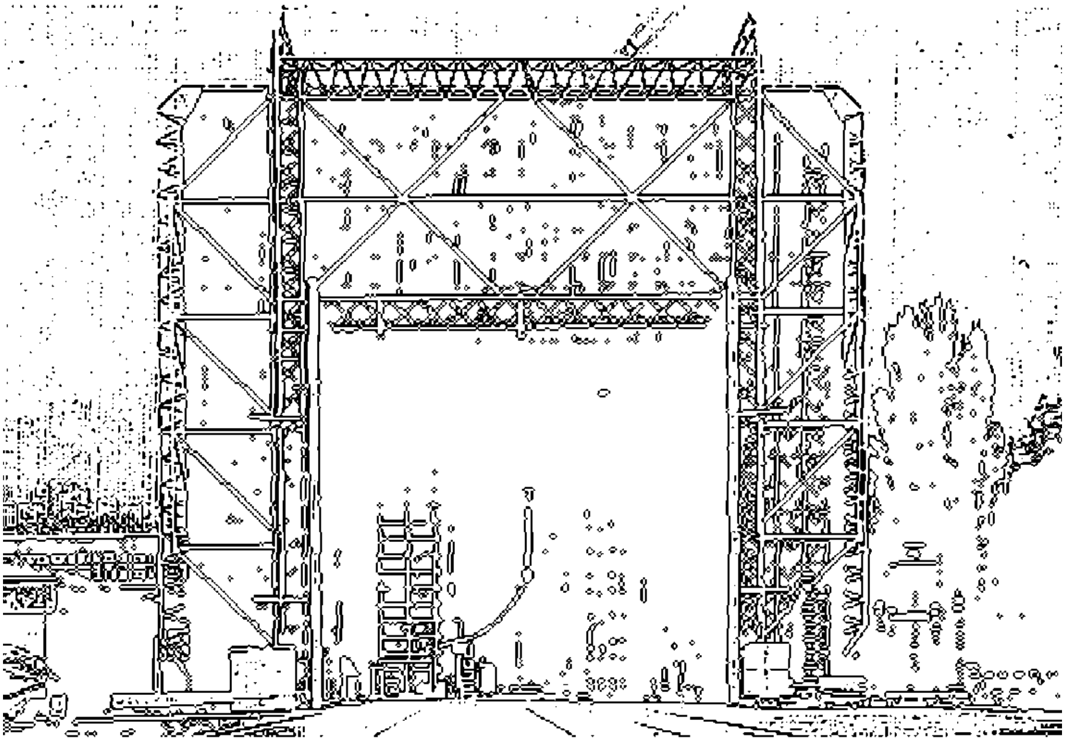

INSTITUT FÜR HOCHSPANNUNGSTECHNIK
UND SYSTEMMANAGEMENT

Infrasound radiations from lightning discharges

Diploma Thesis

conducted at

in cooperation with

Author: Daniela Beiser

Supervisor: Ao. Univ.Prof. Univ.Doz. Dipl.-Ing. Dr.tech. Stephan Pack (TUG)

DI Dr. Gerhard Diendorfer (ALDIS)

DI Ulrike Mitterbauer (ZAMG)

Graz, November 2011

Acknowledgements

I would like to thank those, who made this thesis possible. I am grateful to my supervisors Ao. Univ.Prof. Univ.Doz. Dipl.-Ing. Dr.tech. Stephan Pack, DI Dr. Gerhard Diendorfer and DI Ulrike Mitterbauer for their support and guidance throughout my thesis.

Many thanks to Dr. Roman Leonhard, head of the Conrad Observatory, and the members of research group OVE-ALDIS for the pleasant cooperation and everybody from ZAMG for the pleasant atmosphere during the research project.

Furthermore I would like to show my gratitude to Dr. Wolfgang Hofer, who shared his house with me during my work in Vienna.

Lastly, my gratefulness to my parents, family and friends for their support and encouragement in any situation.

Statutory Declaration

I declare that I have authored this thesis independently, that I have not used other than the declared sources / resources, and that I have explicitly marked all material which has been quoted either literally or by content from the used sources.

Graz, November 2011 ……………………………………………..

(Daniela Beiser)

Abstract

The purpose of this work is a comparison between lightning parameters and infrasound data. There is a great variety of atmospheric sources to produce infrasound. In this study lightning discharges as source of infrasonic signals and their behavior are investigated. There are two different theories of possible source mechanisms producing different waveforms described in the first part of this work. A short overview of propagation effects is also given in this part. Lightning location systems (LLS) are used to observe lightning discharges and gather some important lightning parameters. ALDIS (Austrian Lightning Detection and Information System) operates such a LLS and provides the data concerning lightning for this study. ALDIS sensors are integrated in the multinational network EUCLID (European Cooperation for Lightning Detection). The IMS (International Monitoring System) is operated by CTBTO (Comprehensive Nuclear Test Ban Treaty Organization) to detect all kinds of nuclear explosions. 60 infrasound stations are part of the IMS and one of them (IS26 Freyung, Germany) is used to gather infrasound data for this study. Austria´s meteorological service ZAMG operates two infrasonic elements at Conrad Observatory (CO) and provides the software tools to process and analyze the infrasound data. Lightning discharges 50km around CO and IS26 and their parameters are used to gather associated infrasound signals. The observed waveforms are compared to the predicted waveforms from theory. Pressure amplitudes of the IS signals are picked for further evaluation. The pressure amplitudes and the detectability of infrasound from lightning as a function of distance and current amplitude are plotted to have a look at possible relations.

Keywords:

Lightning discharge, audible thunder, infrasonic thunder, infrasound detectability, Conrad Observatory, IS26 Freyung

Kurzfassung

Diese Arbeit befasst sich mit der Gegenüberstellung von Blitz-Parametern und Infraschall-Daten. Es gibt eine große Vielfalt an atmosphärischen Quellen, die Infraschall produzieren. In dieser Studie werden Blitzentladungen als Quelle der Infraschall-Signale und deren Verhalten untersucht. Zur Erzeugung von IS Signalen durch atmosphärische Entladungen gibt es zwei verschiedene Theorien, die verschiedene Wellenformen vorhersagen und im ersten Teil dieser Arbeit beschrieben werden. Weiters beinhaltet dieser Teil der Arbeit einen kurzen Überblick über Ausbreitungseffekte von Schall und Infraschall. Blitz-Ortungssysteme (Lightning Location Systems, LLS) werden verwendet, um Blitzentladungen zu lokalisieren und einige wichtige Blitz-Parameter zu sammeln. ALDIS (Austrian Lightning Detection and Information System) betreibt ein solches LLS und liefert die Daten über Blitze für diese Studie. ALDIS Sensoren sind im multinationalen Netzwerk EUCLID (European Cooperation for Lightning Detection) integriert. Das IMS (International Monitoring System) wird von der CTBTO (Comprehensive Nuclear Test Ban Treaty Organization) betrieben, um alle Arten von nuklearen Explosionen zu erkennen. 60 Infraschall-Stationen sind Teil des IMS und eine von ihnen (IS26 Freyung, Deutschland) wird verwendet, um Infraschall-Daten für diese Studie zu sammeln. Österreichs Wetterdienst ZAMG (Zentralanstalt für Meteorologie und Geodynamik) betreibt zwei Infraschall-Elemente am Conrad Observatorium (CO) und stellt die Software zur Verarbeitung und Analyse der Infraschall-Daten zur Verfügung. Blitzentladungen 50km rund um CO und IS26 und deren Parameter werden verwendet, um zugehörige Infraschall-Signale zu sammeln. Die beobachteten Signale werden mit den aus der Theorie vorhergesagten Wellenformen verglichen. Für die weitere Auswertung werden die Druck-Amplituden der IS-Signale aufgenommen. Die Druck-Amplituden und die Nachweisbarkeit von Infraschall durch Blitzschlag in Abhängigkeit von der Entfernung und der Stromamplitude werden in Diagrammen dargestellt, um mögliche Zusammenhänge zu erkennen.

Schlagwörter:

Blitzentladung, hörbarer Donner, Donner im Infraschallbereich, Nachweisbarkeit von Infraschall, Conrad Observatorium, IS26 Freyung

Table of Contents

Introduction

Lightning is a natural phenomenon that is both beautiful and dangerous. Therefore human being has been trying to elucidate the processes comprising lightning for a long time. Some parts of lightning physics are still not fully understood and research remains to be conducted. Infrasound radiation from lightning discharges is one of those subjects and investigations on this object are made in this study. The object of research contains several areas of sciences such as high voltage engineering, physics and acoustics.

This study was conducted in cooperation of several institutions. Austrian Lightning Detection and Information System (ALDIS) provided the lightning data used in this work and Central Institute for Meteorology and Geodynamics (ZAMG) provided the infrasound data as well as the software tools necessary to evaluate the data. Comprehensive Nuclear Test Ban Treaty Organization (CTBTO) operates Infrasound Stations all over the world to monitor nuclear explosions and therefore it is important to associate the detection of an infrasound signal with its proper source. Data from one of the operating CTBTO Infrasound Stations was used in this work.

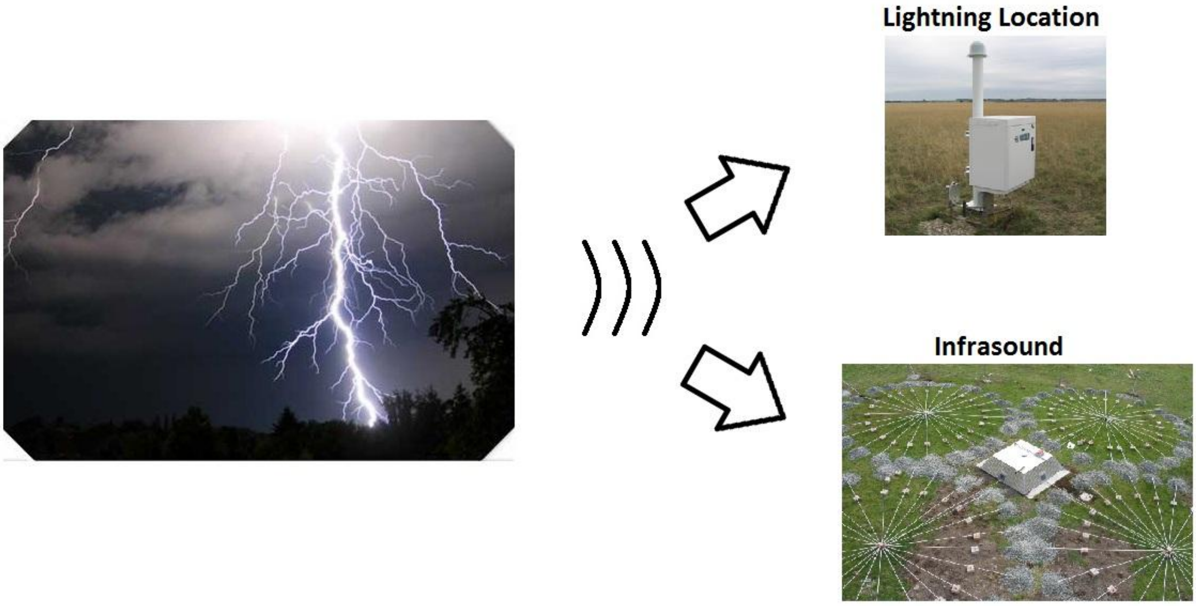

Figure 1: Schematic representation of the relation between a lightning discharge, lightning location and infrasound observation (ALDIS, 2011; http://www.flickr.com/photos/ctbto/)

Theory

1. The lightning discharge

Lightning is a transient, high-current electric discharge. It´s path length is measured in kilometers and the most common source is the electric charge separated in thunderstorm clouds (see also Chapter 3). The total discharge has a duration of about half a second and is termed a flash. An average flash is typically made up of three to four high-current pulses called strokes, lasting for about one millisecond and being separated by several tens of milliseconds. Because the human eye can just resolve the individual light pulse associated with each stroke lightning often appears to "flicker".

Lightning discharges from cloud to ground are of great practical interest (as they can cause injuries and death, disturbances of power and communicating systems) and therefore have been studied more extensively than other forms of lightning discharges although the majority of the discharges occur within the confines of the clouds. The most common cloud-to-ground discharge lowers negative cloud charge toward ground (about 90% of all CG discharges).

The processes occurring during one negative CG flash illustrated in *Figure 1-1* are thought to be as follows: Between the positive (P) and the negative (N) charged layers inside the cloud a so-called preliminary breakdown takes place and sets the stage for negative charge to be lowered toward ground by the stepped leader. Leader steps are typically tens of meters in length and 1µs in duration. The pause time between the steps is about 50µs and the average downward leader speed is about $2*10^5$m/s. The attachment process begins as the electric field on the ground (at sharp objects for example) exceeds the breakdown value of air and one or more upward-moving discharges are initiated. At the moment one of them contacts the downward-moving leader, the leader tip is connected to ground potential. The leader channel is discharged as the first return stroke propagates up the previously ionized and charged leader path. The upward speed of a return stroke is typically between one-third and one-half of the speed of light ($1*10^8$m/s to $1.5*10^8$m/s). After the return stroke current has ceased to flow, the flash may end.

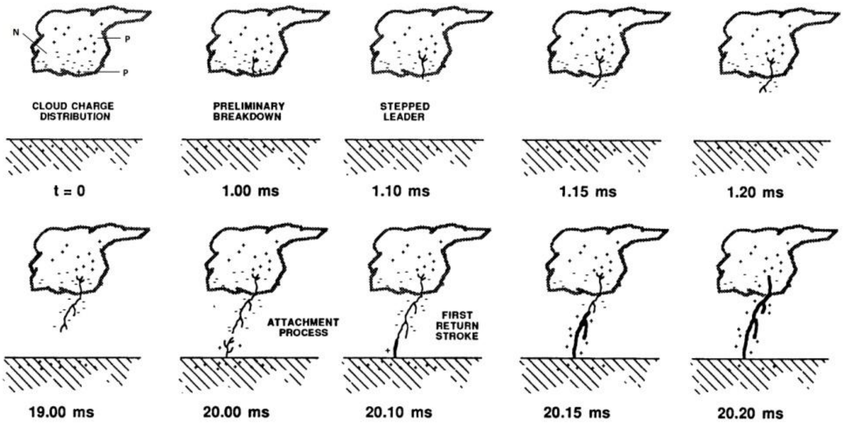

Figure 1-1: Processes comprising a negative single stroke cloud-to-ground flash (Uman, 2001)

If additional charge is available at the top of the channel, a continuous dart leader may propagate down the residual first-stroke channel at a speed of about $3*10^6$m/s. The dart leader then initiates the second or any subsequent return stroke as shown in *Figure 1-2* (Uman, 2001).

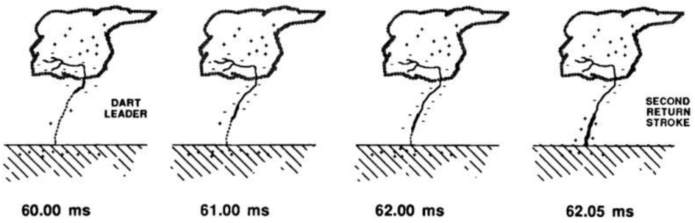

Figure 1-2: Dart leader and second (or any subsequent) return stroke of a negative CG flash (Uman, 2001)

Video observation of CG lightning has shown that one-third to one-half of all CG discharges strike ground at more than one point with a spatial separation between the points being up to some kilometers.

The energy per unit length deposited by a lightning return stroke can be estimated as follows:

$$E_l = \frac{Q * U}{l} \qquad [1]$$

E_l … energy per unit length in J/m
U … potential between ground and the negative charged layer inside the cloud in V
Q … amount of charge lowered toward ground during the lightning process in As
l …. length of the lightning channel in m

For $U=10^8$V, Q=5As and l=5km Eq. [1] yields 10^5J/m as the deposited energy per unit length.

2. Audible thunder: The acoustic radiation from hot channels

Thunder is probably the most common of all loud natural sounds and it originates in the expansion of the rapidly heated lightning channel. There may be differences in the breakdown and propagation of lightning inside and outside of clouds, but once a discharge is formed, there is no reason to believe the thermodynamics and hydrodynamics are basically any different, other than differences in energy input. For this reason the theory of thunder generation can be treated equally for CC and CG discharges (Few, 1995).

2.1. Shock wave formation and expansion

The return stroke channel attains a temperature of about 30,000 K in a time less than 10 µs (Uman, 2001). Since there is insufficient time for the channel particle density to change appreciably, the channel pressure must rise in response to the temperature rise. According to Uman the channel reaches an average pressure of about 10 bar during the first 5 µs. Such a channel overpressure results in an expansion of the channel behind a shock wave.

A shock wave is a type of propagating disturbance. It carries energy and can propagate through a medium (solid, liquid, gas or plasma) or in some cases in the absence of a material medium, through a field such as the electromagnetic field. Shock waves are characterized by an abrupt, nearly discontinuous change in the characteristics of the medium. Across a shock there is always an extremely rapid rise in pressure, temperature and density of the flow. A shock wave travels through most media at a higher speed than an ordinary wave (Wikipedia, 2010).

As the lightning channel expands, its pressure decreases toward atmospheric pressure on a time scale of tens of microseconds. The channel remnant cools slowly by conduction, convection and radiation and becomes nonconducting at temperatures between 2,000 and 4,000 K (Few, 1995).

The development of the shock wave can be divided into three periods: strong shock, weak shock and acoustic:

2.1.1. Strong shock

The shock wave has to do thermodynamic work (P*dV) on the surrounding fluid which is at constant pressure P_0 during its expansion. The distance at which all of the internal thermal energy has been expended in doing the work of expansion is the maximum distance up to which the strong shock wave can expand. This distance is called “Relaxation Radius” R_S and is given by:

$$R_s = \sqrt[3]{\frac{3E_t}{4\pi P_0}} \qquad [2]$$

where
E_t is the total input energy in the spherical case,
R_S is the spherical relaxation radius and
P_0 is the atmospheric pressure.

For a cylindrical geometry, like a lightning channel, the Relaxation Radius R_C is given by:

$$R_c = \sqrt{\frac{E_l}{\pi P_0}} \qquad [3]$$

where
E_l is the energy per unit length in the cylindrical case (Few, 1995).

Since the energy of the radiated radio frequency and the optical radiation had been measured to be relatively small it is assumed that essentially all of the lightning input energy is transferred to the hot gas driving the shock wave (Uman, 2001).

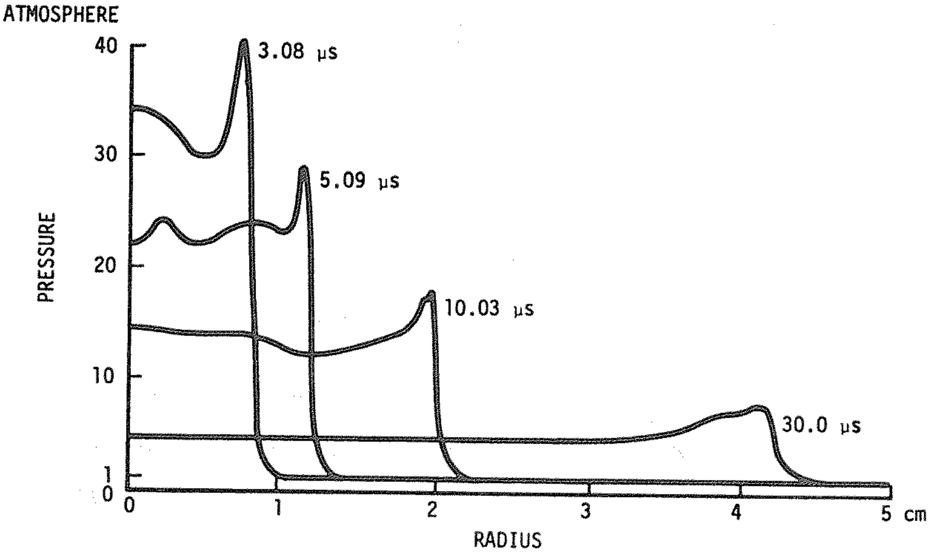

*Figure 2-1: Strong shock wave development for a simulated lightning return stroke using cylindrical geometry (Hill, 1971). The computed electrical energy input into this simulated channel was 1.5*10^4 J/m. Early development of the shock wave shows several internal waves prior to final shaping of the shock wave.*

Figure 2-1 displays the strong shock solution for cylindrical case from Hill (Hill, 1971). It shows numerous internal waves travelling back and forth between the shock front and the origin due to the very high internal temperatures. Since the shock front itself is moving into cold stationary air it has to advance somewhat slower than these internal waves which have to organize the fluid behind the shock, so that the resulting distribution of pressure and temperature allows the steady progression of the strong shock.

A nondimensional coordinate $X_{s,c}$ is defined as

$$X_s = \frac{r_s}{R_s} \qquad [4]$$

$$X_c = \frac{r_c}{R_c} \qquad [5]$$

r_s …. Distance from the spherical source
r_c …. Distance from the cylindrical source
R_s and R_c are as defined in Eqs. [2] and [3].

The solution to the hydrodynamic equations for the shock wave in either geometry in terms of $X_{s,c}$ is independent of the input energy because $X_{s,c}$ is normalized in terms of that energy. When X_s=X_c=1, the pressure pulses from cylindrical and spherical sources have similar magnitudes and waveshapes.

Figure 2-2 from Few (Few, 1995) shows the propagation of the strong shock into the transition region (X~1) and beyond into the weak shock region. Throughout this region of strong shock expansion (0.2<X<1) the shape of the pressure profile is essentially that of the similarity solution by Sakurai (Sakurai, 1954).

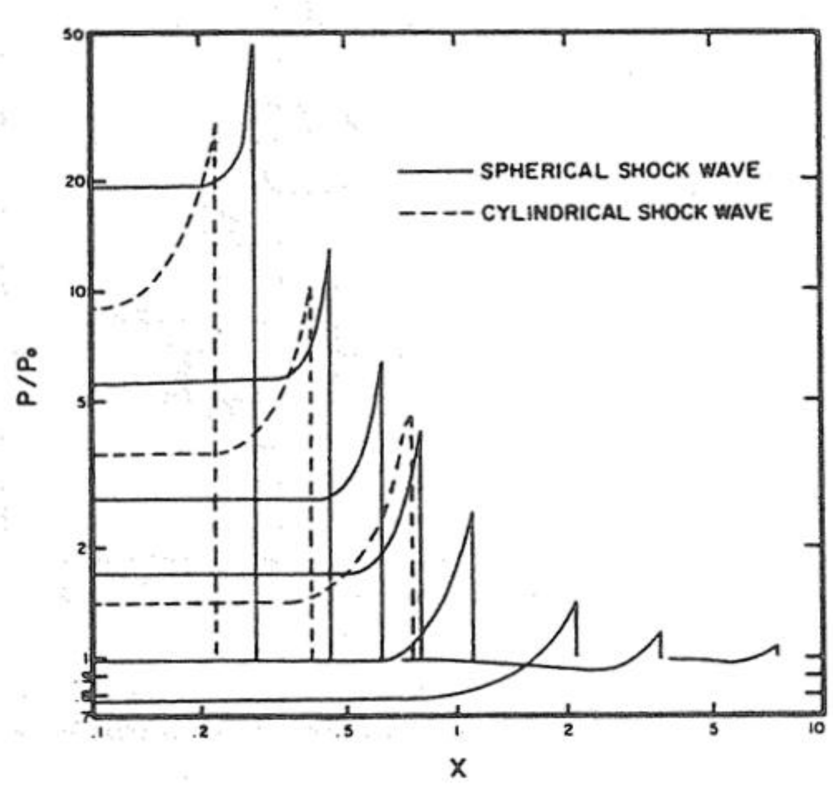

***Figure 2-2: The expansion of spherical and cylindrical shock waves from the strong shock region into the weak shock region. The radii of both spherical and cylindrical geometries have been nondimensionalized using the relaxation radii defined in Equation [2] and [3]. The spherical shock wave is that of Brode* (Brode, 1956) *and the cylindrical shock wave is from a similarity solution by Sakurai* (Sakurai, 1954).**

2.1.2. Transition region and weak shock

As the shock front passes the relaxation radius (X=1) the central pressure passes through ambient pressure as postulated in the definition of the relaxation radii in Eqs. [2] and [3] and shown in *Figure 2-2*. The momentum gained by the gas during the expansion carries it beyond X=1 and forces the central pressure to momentarily go below atmospheric. At this point the now weak shock pulse decouples from the hot channel remnant and propagates outward as an "N"-wave (Few, 1995). The N-wave is so named for its N-like shape as shown in *Figure 2-8*.

Figure 2-3 shows the final output from Brode's numerical solution (Brode, 1956), the weak shock pulse or N-wave at a radius X=10.5.

Figure 2-4 from Few (Few, 1995) presents a graphically summary of the various transitions that are thought to take place. The initial strong shock will behave cylindrically following the dashed line based upon Plooster (Plooster, 1968); this must be the case for the line source regardless of the tortuosity, because the high speed internal waves depicted in *Figure 2-1* will hydrodynamically adjust the shape of the channel during this phase. The transition from strong shock to weak shock occurs near X=1 and the transitions from cylindrical divergence to spherical divergence will occur somewhere beyond X=0.3 and X=1, depending upon the particular geometry of the channel at this point. The family of lines labeled χ in *Figure 2-4* represents transition occurring at different points.

$$\chi = \frac{L}{R_c} \qquad [6]$$

L …. effective length of the cylindrical source
R_c as defined in Eq. [3].

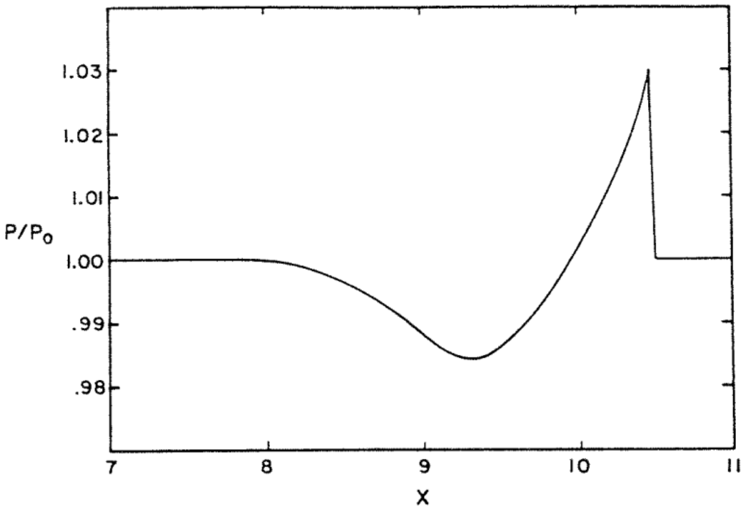

Figure 2-3: The weak shock wave formed from the spherical strong shock wave. This is the final pressure profile computed by Brode (Brode, 1956). *For an energy input for 10^5 J/m (Rc=0.56 m for P0=10^5 Pa) this weak shock wave would be approximately 6 m from the lightning channel.*

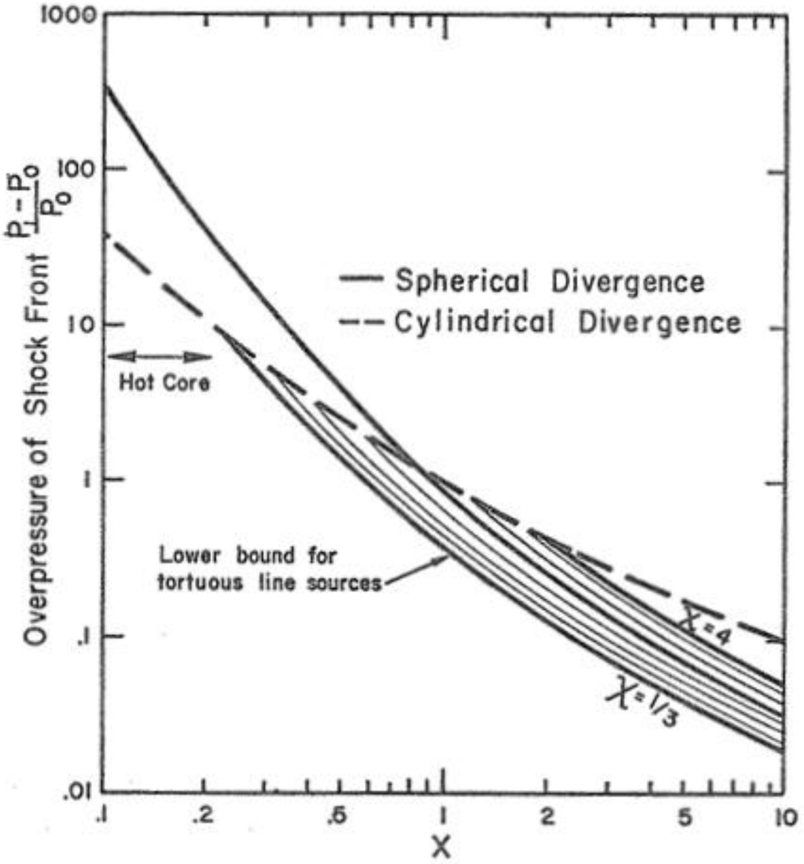

Figure 2-4: Line source shock wave expansion (Few, 1995) *. The overpressure of the shock front is given for spherical* (Brode, 1956) *and cylindrical* (Plooster, 1968) *shock waves. Line sources must initially follow cylindrical behavior, but upon expanding to distances of the same size as line irregularities, they change to spherical expansion following curves similar to the curves depicted in this figure.*

2.1.3. The sound wave

The shock wave emitted by the return stroke channel relaxes to a sound wave at a distance of a few meters from the channel. The length of a sound wave resulting from relaxation of a cylindrical shock wave was found to be

$$l = 1.47\sqrt{\frac{E_l}{P_0}} \qquad [7]$$

E_l .... Energy per unit length
P_0 .... Ambient pressure
l .... Wave length of the sound wave

The distance from the channel at which the weak shock wave relaxes to a sound wave is apparently in the same order of magnitude as l (Uman, 1984).

Observations of thunder spectra lead to the prediction that the acoustic spectrum has a maximum at frequency fm

$$f_m = 0.63c_0\sqrt{\frac{P_0}{E_l}} \qquad [8]$$

where c_0 is the speed of sound (340m/s). The constant (0.63) should be decreased for measurements made in the kilometer or greater range since observed peak frequencies will decrease with distance from the channel. For E_l values around 10^5J/m Eq. [8] leads to f_m values in the range of 200Hz. Furthermore Eq. [8] points out that the theory described in the preceding sections cannot predict infrasonic frequency peaks with any reasonable constant without requiring unrealistically large channel energies and therefore can only be used to describe the sonic peaks. For f_m = 5Hz an input energy to the channel of $E_l = 1.84*10^8$J/m would be required according to Eq. [8].

Thunder is usually inaudible for an observer on the ground at distances greater than 25km because the sound rays are refracted upwards resulting from the usual atmospheric temperature gradient (Uman, 2001).

The velocity of sound is proportional to the square root of the temperature (Eq. [9]) and the temperature decreases as a function of height in the domain of the lightning channel. The generalized vertical distribution of temperature and pressure up to an altitude of 80km is shown in *Figure 2-5*.

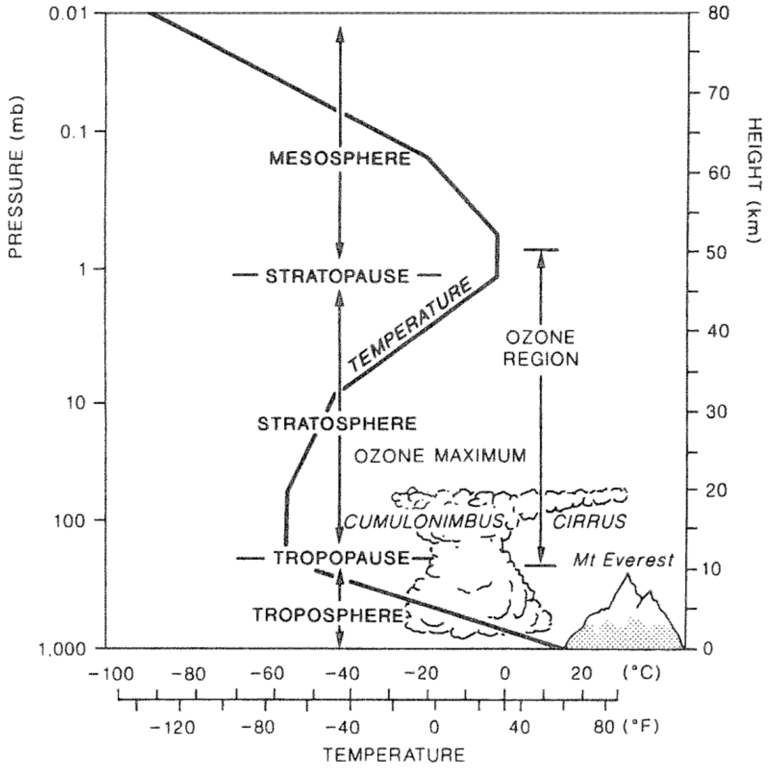

***Figure 2-5: Generalized vertical distribution of temperature and pressure up to an altitude of 80km adapted from "Atmosphere, weather and climate"* (Barry, et al., 1998)**

$$c = \sqrt{\frac{\gamma * R * T}{M}} = \sqrt{\frac{\gamma * k * T}{m}} \qquad [9]$$

c …. Velocity of sound in m/s
γ …. Heat capacity ratio, 1.4 in this case
R …. Molar gas constant (approximately 8.3145 J·mol^{-1}·K^{-1})
k …. Boltzmann-constant (1.3806504×10^{-23}J/K)
M .. the molar mass in kilograms per mole (mean molar mass for dry air is about 0.0289645 kg/mol)
m … the mass of a single molecule in kilograms
T …. Absolute temperature in K
(Wikipedia, 2010)

Considering the velocity of sound as a function of decreasing temperature with height Snell's law

$$\frac{\sin\theta_1}{\sin\theta_2} = \frac{c_1}{c_2} \qquad [10]$$

indicates that sound waves usually will be refracted upward.

The path of the sound ray through an atmosphere with constant temperature gradient was calculated by Fleagle (Fleagle, et al., 1980).

$$\frac{\mathrm{dx}}{\mathrm{dz}} = \sqrt{\frac{\mathrm{T}}{\gamma \mathrm{z}}} \qquad [11]$$

Integration of Eq. [11] yields

$$\mathrm{x} - \mathrm{x}_0 = 2\sqrt{\frac{\mathrm{Tz}}{\gamma}} \qquad [12]$$

With lapse rate γ=7.5K/km and temperature T=300K Eq. [12] yields approximately 25km for the maximum distance a sound wave emitted at z=4km height is heard by an observer on the ground (*Figure 2-6*).

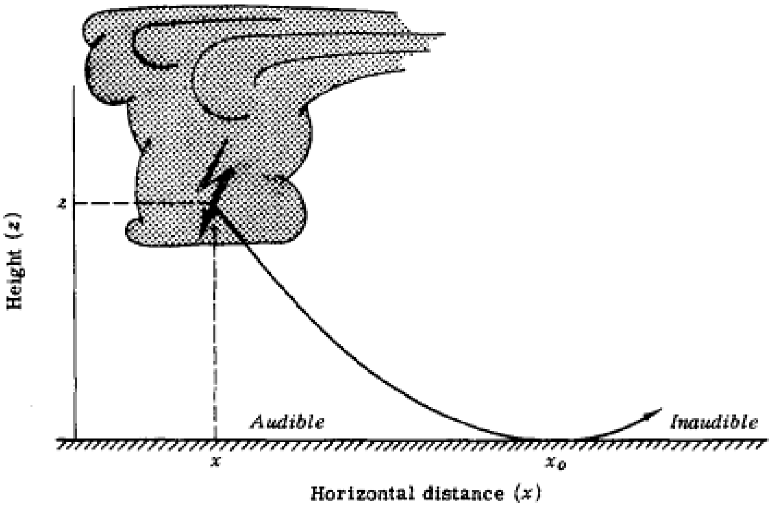

Figure 2-6: The Path of a sound ray emitted by a lightning flash at height z (Fleagle, et al., 1980)

2.2. Comparison of the theory with experiments and numerical solutions

In the preceding section return strokes are supposed to be the generators of thunder. Even if optical, spectroscopic and electromagnetic radiations indicate that the return stroke is the most energetic part of the event there is some controversy about the energy deposited by lightning return strokes. The numerical solutions of Hill and Plooster for example use energy inputs of $1.5*10^4$ J/m (Hill) and $2.4*10^3$J/m (Plooster) while the value for the energy should be approximately 10^5J/m if the potential between the ground and the negative charge of the cloud is 10^8V, the lightning process (leader included) lowers -5C and the channel is 5km long.

For the acoustic processes it doesn't make any difference if the energy is deposited by the return stroke or the leader as long as the deposition process is sufficiently fast and concentrated to produce a strong shock.

If a strong shock is never formed because most of the lightning stroke energy is deposited in a large volume a new theory starting from weak shock initial conditions would need to be formulated. Rough calculations for this type of diffuse mechanism done by Hill (Hill, 1979) indicate a pressure amplitude much lower (factor 80) than the return stroke wave and therefore this is not a very likely possibility.

"Natural thunder does not provide a good source for testing the details of the shock wave theory of its origin because

- *The thunder signal is a superposition of multiple pulses from multiple leaders and strokes.*
- *The thunder signal also convolves the pulses from numerous tortuous channel segments and branches.*
- *The strike point is not controllable, making systematic investigation difficult.*
- *Each event is unique and the range of parameters is wide, making the experiment nonrepeatable.*
- *One rarely has the quantitative information on the lightning parameters needed for predicting the thunder signal.*

We can find some support for the theory by making enough simplifying assumptions regarding the nature of thunder signal to test it with real lightning; or, we can employ laboratory simulations for a more controlled test." (Few, 1995)

A series of such laboratory simulations has been performed at Westinghouse Research Laboratories with a $6.4*10^6$V impulse generator producing 4m spark discharges in air. Calibrated microphones were used to measure the shock wave as a function of distance. In addition the gap voltage and current were measured to compute the power deposition.

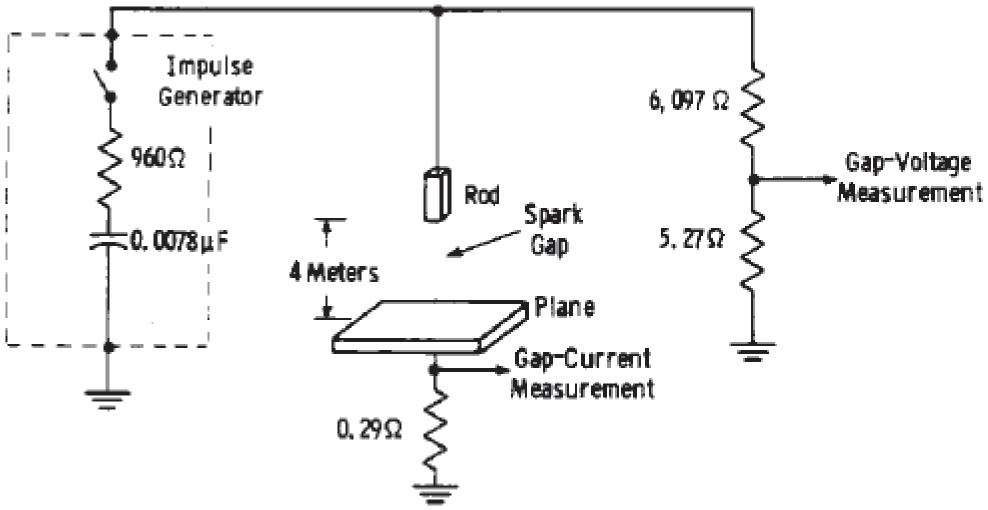

Figure 2-7: Schematic diagram showing the circuit for producing 4-m rod-plane-sparks and circuits for measuring spark gap voltage and current **(Uman, 1971).**

In general the results of the research were found to be consistent with the theory developed by Few (Few, 1995).

Figure 2-8 shows the comparison of a measured pressure pulse from a long spark with the profile that is predicted from theory. That the peak measured pressure exceeded the predictions could be an indication that χ=4 instead of χ=4/3 would be the appropriate value for the measured wave (Few, 1995).

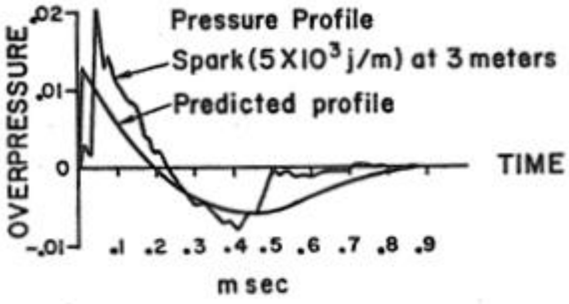

Figure 2-8: Comparison of the measured pressure wave of a long spark with the predicted pressure from a section of a tortuous channel having the same energy per unit length. χ (Equation [6]) is assumed to be 4/3.

Figure 2-9 and *Figure 2-10* from Uman (Uman, 1970) summarize the extensive series of spark measurements with the total electrical energy of $5*10^3$J/m computed from measurements of gap voltage and current. *Figure 2-9* is comparable to *Figure 2-4*, the center line labeled L=0.5m corresponds to χ=4 in *Figure 2-4* using the measured energy input of $5*10^3$J/m giving R_C=0.126m. The two boundary lines L=6.25cm and L=4.0m correspond to χ=0,5 (close to the lower bound χ=1/3 in *Figure 2-4)* and χ=32 (too large to be depicted in *Figure 2-4* where χ=4 is the last line shown). The data points corresponding to larger χ or L values in *Figure 2-9* could represent situations where the shock wave expansion was following the cylindrical behavior over a long distance.

But if the expansion was really cylindrical to that extent, the duration of the positive pulse should be much longer than it was in the measurements.

Figure 2-10 indicates that the data points clearly do not lie in the cylindrical regime, they tend to be even shorter than predicted from theory of spherical expansion. It is known that the spark is tortuous and produces multiple pulses. In the experiments it was found that the pulses show more multiplicity aspects and greater relative phase shifts at closer distances while they showed evidence of in-phase-superposition more distant from the spark. The distribution in *Figure 2-9 and Figure 2-10* is produced by this superposition. Relative to a single pulse the pressure amplitude would be increased but the wave length would not be substantially effected. The measured waveforms were systematically shorter than predicted by the theory. *Figure 2-8* shows that the tail of the wave is shortened and the duration of the positive pulse in *Figure 2-10* is also shorter than expected. A possible explanation could be that in the theory an instantaneous energy input is applied while the energy input to the spark is being of longer duration. The longer energy input causes the low density channel core to be kept at temperatures much higher than predicted by the theory. The higher temperature causes elevated speed of sound and therefore the wave following the shock front forms and propagates outward faster than predicted producing the shortened waveforms measured.

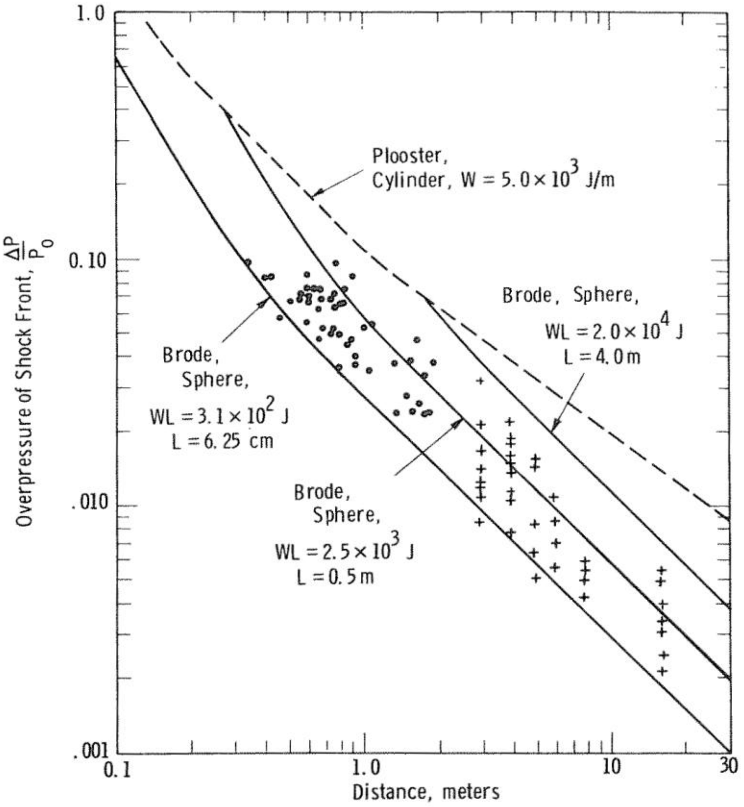

***Figure 2-9: Shock front overpressure as a function of distance from the spark. The dots represent data obtained with a piezoelectric microphone; the crosses represent data obtained with a capacitor microphone. Also shown are theoretical values for cylindrical and spherical shock waves* (Few, 1995).**

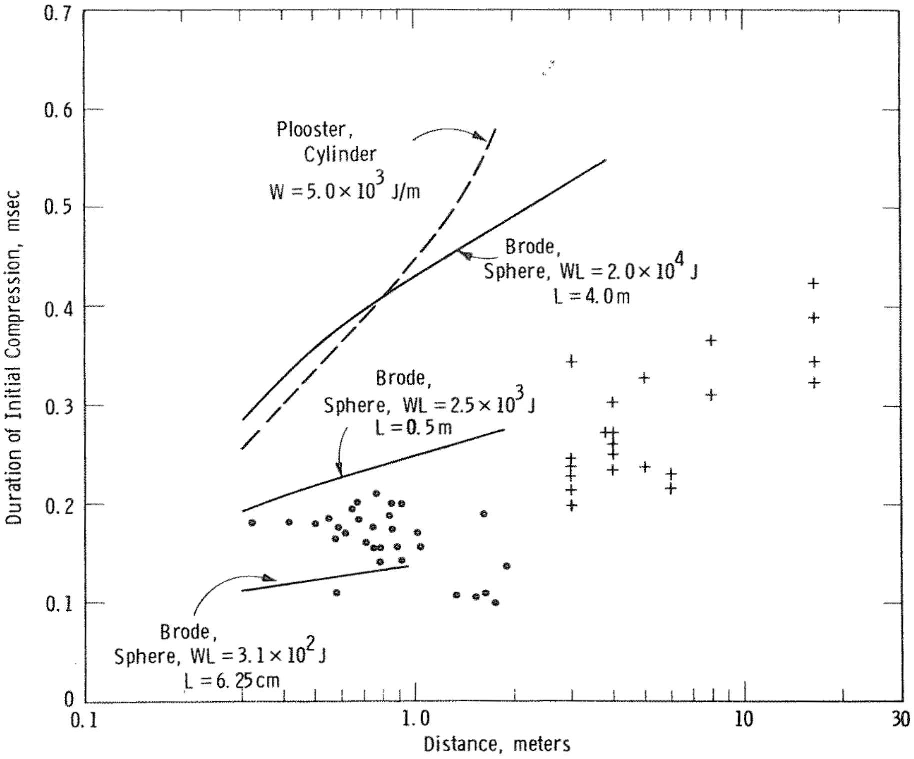

Figure 2-10: Duration of the positive part of the shock wave from the long spark at various distances **(Few, 1995).**

3. Infrasonic thunder: Electrostatic acoustic emission

Sound waves in general are mechanical waves that propagate through media as longitudinal waves causing a particle displacement in the direction of wave propagation. The amplitude of sound waves is measured in units of pressure. The human ear is able to distinguish pressure fluctuations in the frequency band of 20-20000Hz. Sound waves above this hearing range are called ultrasound, sound waves below are called infrasound. Infrasonic thunder is the low frequency sound wave generated by lightning discharges and one possible source mechanism is explained in this chapter.

3.1. Waveform

Infrasonic pulses were found in experiments made by Bohannon in 1977 (Bohannon, 1977) and 1978 (Bohannon, 1978) and Balachandran in 1979 (Balachandran, 1979) after the existence of infrasonic peaks in power spectra of thunder were reported by Holmes in 1971 (Holmes, 1971). The three experiments agree closely on the characteristics of the infrasonic pulses both in amplitudes and in periods but most importantly they agree in the shape of the waveform depicted in *Figure 3-1* and the direction of the wave. The pulses appear to be beamed from directly overhead.

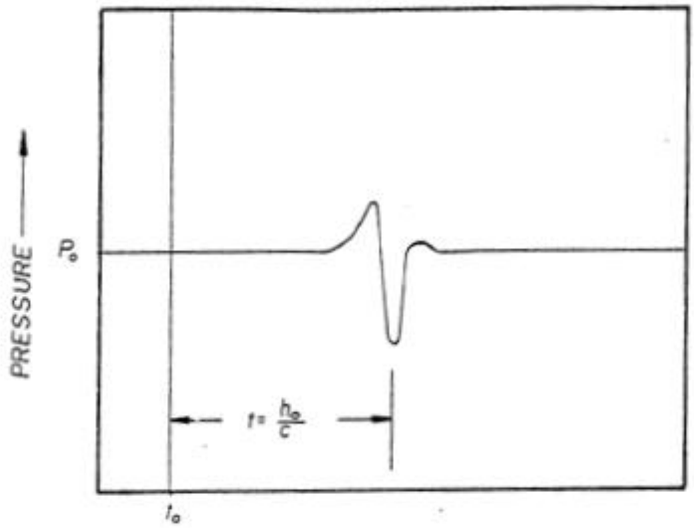

Figure 3-1: Idealized Waveform showing the general structure found in the experimental data **(Bohannon, 1980)*****. The infrasonic signal corresponds to a lightning flash occurring at t_0, the sound ray is expected to be produced at height h_0 and travels with speed of sound c toward ground.***

3.2. Theoretical explanation

The collision between heavier water droplets and lighter ice crystals inside the cloud is thought to be the reason for the particles to get charged. The positive charged ice crystals get to the upper part of the cloud because of strong updrafts while the negative charged water droplets concentrate in the lower part of the thundercloud. Near the base of the thundercloud there is another layer of positive space charge called shielding layer.

The negative charged particles repel each other and tend to move apart sweeping some of the air along with them. Therefore the atmospheric pressure in the charge storage region is reduced. The space between the particles is filled by the pressure field radiating from each particle, so the air molecules can't rush in between the cloud particles to restore atmospheric pressure equilibrium.

$$P_{inside} = P_{outside} - \frac{n}{2}\varepsilon_0 {E_0}^2 \qquad [13]$$

P …. Atmospheric pressure
ε_0 …. permittivity of free space (≈$8.854*10^{-12}$As/Vm)
E_0 …. Electric field produced by the charge in the region
n …. Geometric factor for the particular shape of the charged region (varying between 1 and 2)

A lightning flash causes the neutralization of some or all of the stored charge and the pressure balance of Eq. [13] is destroyed because of the sudden removal of the charge. The force that held the particles apart will be reduced and as pressure equilibrium is restored an outward propagating acoustic wave will be produced. For an observer on the ground a rarefactional wave produced by the lower side of the charged region will arrive first followed by a compressional wave that has to travel a longer distance and therefore arrives later produced by the upper side of the charged region. The waveshape seen by an observer on the ground is shown in *Figure 3-3*. Considering the charged volume to be disc-shaped the amplitude of the signal is

$$\Delta p = \frac{{Q_1}^2 - {Q_2}^2}{8\pi^2 \varepsilon_0 r^4} = 0.12Pa \qquad [14]$$

if
Q_1=40C ……………………….stored charge in the region before the flash
Q_2=15C ………………………. stored charge in the region after the flash
r=2km …………………………. radius of the volume
ε_0=$8.854*10^{-12}$ As/Vm …. permittivity of free space

Q_1-Q_2 and therefore the amount of neutralized charge by a flash and the relation shown in Eq. [14] is plotted in *Figure 3-4*.

It is worth to note that the pressure Δp depends on the stored charge before the flash and not only on the charge neutralized (Q_1-Q_2) by a given flash.

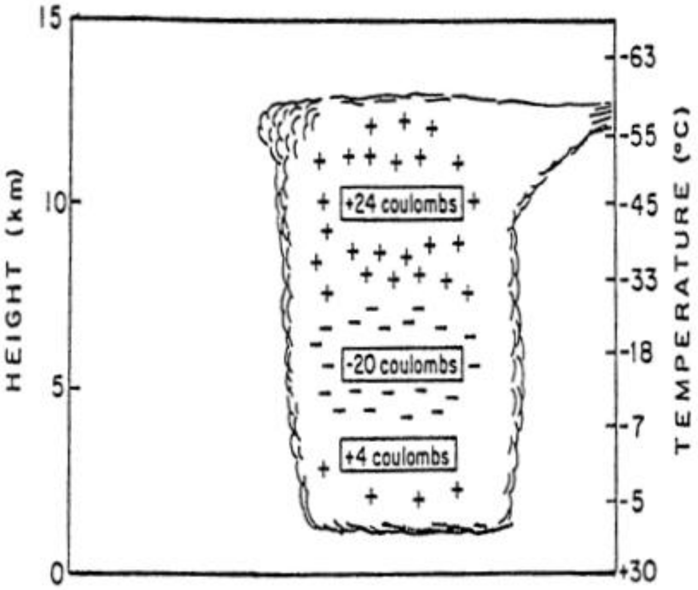

Figure 3-2: Schematic diagram to show the distribution of charges in a thunderstorm (Wallace, 1977).

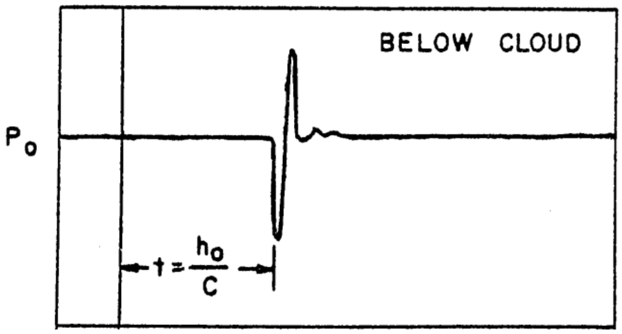

Figure 3-3: Acoustic signature expected from the release at time to of electrostatic pressure from a flat horizontal volume located at altitude h_0 (Dessler, 1973).

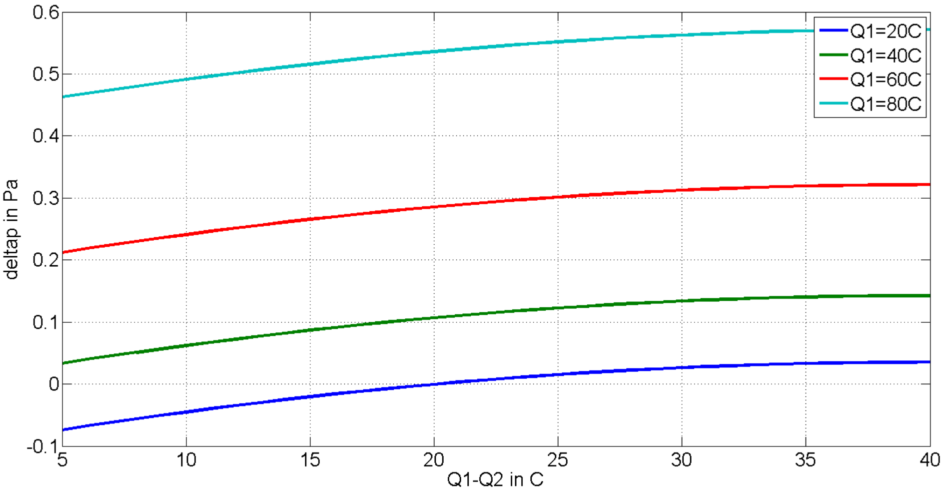

Figure 3-4: Dependency of the pressure amplitude on the disk-shaped charge as a function of neutralized charge (Q_1-Q_2), r=2km.

Comparing *Figure 3-1* and *Figure 3-3* shows that the compressional pulse preceding the rarefactional pulse found in the experimental data in *Figure 3-1* can't be explained with the theory developed so far.

Considering the shielding layer a similar explanation can be found for the initial positive excursion in the infrasonic waveform. The two regions of opposite space charge attract each other and the pressure balance equation becomes

$$P_{inside} = P_{outside} - \frac{n}{2}\varepsilon_0 E_+ E_- \qquad [15]$$

E_+ and E_- are the electric fields due to the positive and the negative space charges, respectively. Because of the charge distribution seen in *Figure 3-2* the electrostatic term will be negative and therefore P_{inside} has to be greater than $P_{outside}$ for the equation to balance. If a lightning flash neutralizes the charge this pressure will be released producing a positive acoustic wave. Because of the location of the shielding layer at a lower altitude the compressional pulse arrives first at an observer at the ground. This theory is valid for both cloud-to-ground lightning and intracloud lightning. Although experimental evidence shows that the charges are usually confined to thin horizontal layers and the use of spherical charges as a model of the thundercloud is a poor approximation of reality, it can be used to get an analytic solution.

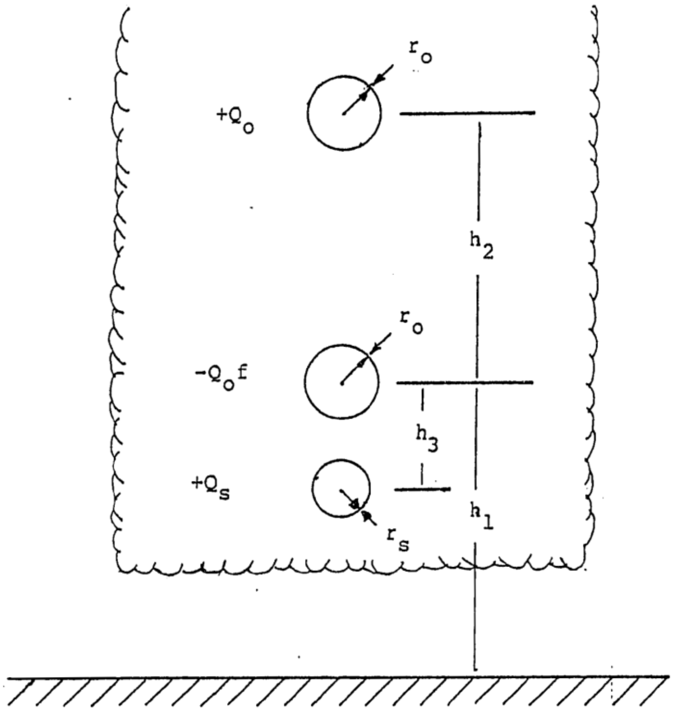

Figure 3-5: Location of the spherical charges as approximation of reality to find an analytic solution (Bohannon, 1980)

The action of the electric field of Q_2=-Q_0*f (as shown in *Figure 3-5*) on Q_s causes the pressure

$$p_s = -\frac{3}{2}\frac{Q_s Q_0 f}{4\pi^2 \varepsilon_0 r_s^2 h_3^2} \quad [16]$$

Q_0 …… initial charge present before a lightning flash
Q_0f …. the charge present at any time will be some fraction f of the initial charge
f ……… fraction before the flash

A lightning flash removes charge of the negative layer and therefore causes a pressure wave to be radiated with amplitude

$$\Delta p_s = p_{s|f=f_A} - p_{s|f=1} \quad [17]$$

f_A …. fraction after the flash

$$\Delta p_s = \frac{3}{2}\frac{Q_s Q_0 (1 - f_A)}{4\pi^2 \varepsilon_0 r_s^2 h_3^2} \quad [18]$$

An observer on the ground will see a positive pulse of this amplitude because the charged particles in the shielding layer will experience an impulse towards the ground while the particles in the negative charged region will move upwards and produce a negative pulse with amplitude

$$\Delta p_2 = \frac{3}{2}\frac{Q_s Q_0 (1 - f_A)}{4\pi^2 \varepsilon_0 r_0^2 h_3^2} \quad [19]$$

arriving at

$$t = \frac{h_3}{c} \quad [20]$$

after the positive pulse. The combined signal is characterized by wavelength 2*h_3 and period t. Neutralization of δQ=25C yields Δp_s=0.686Pa as amplitude of the pressure pulse radiated by the shielding layer (Eq. [16]) and Δp_2 =0.043Pa as amplitude of the pressure pulse radiated by the negative charged layer (Eq. [19]). (Bohannon, 1980)

The relations shown in Eq. [18] and Eq. [19] are plotted in *Figure 3-6*. The amplitude of the negative pulse p_2 is very small and therefore can easily be overwhelmed by wind noise and other infrasonic signals.

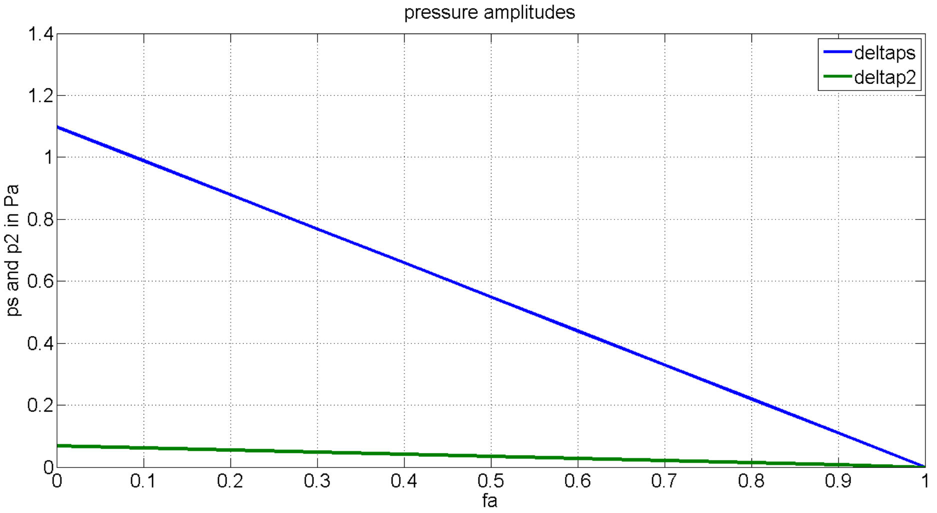

Figure 3-6: Dependency of the pressure amplitude on the fraction of charge remaining after a lightning flash. The charges are considered to be spherical.

3.3. Experimental observation of lightning produced infrasound

In 2008 a study on the correlation between infrasound signals and electro-magnetic signals from lightning was done in the Netherlands (Assink, et al., 2008). To detect infrasound signals two infrasound arrays with 145km distance in between were used. A microbarometer measuring pressure variation in the frequency band from 0.002 to 20Hz is connected to six porous hoses in a star-like configuration to reduce wind noise. Each array consists of six microbarometers. For the EM measurements the SAFIR (Surveillance et Alerte Foudre par Interférometrie Radioélectrique) lightning detection network consisting of four detection stations in the Netherlands and three in Belgium was used. Each SAFIR Station consists of five very high frequency (VHF) dipole antennas placed on a circular plane and one low frequency (LF) antenna, all sensitive to electromagnetic waves. To detect and localize CC discharges the VHF antennas are used. Interferometry and cross bearing the observations reported by different stations yields location, time and error of detection values. The LF antennas are used to detect CG discharges by means of hyperbolic intersection and time-of-arrival methods. At least four stations are needed to get explicit results. Location, time, error of detection, current peak, rise and decay time are detected for CG discharges.

A severe thunderstorm passing over the Netherlands on the 1st of October 2006 was taken to gather data for further investigations.

Figure 3-7: The left picture shows the top of a SAFIR station with VHF array and LF sensor. The right picture shows a microbarometer with noise reducer attached constructed of porous hoses. (Holleman, et al., 2006)

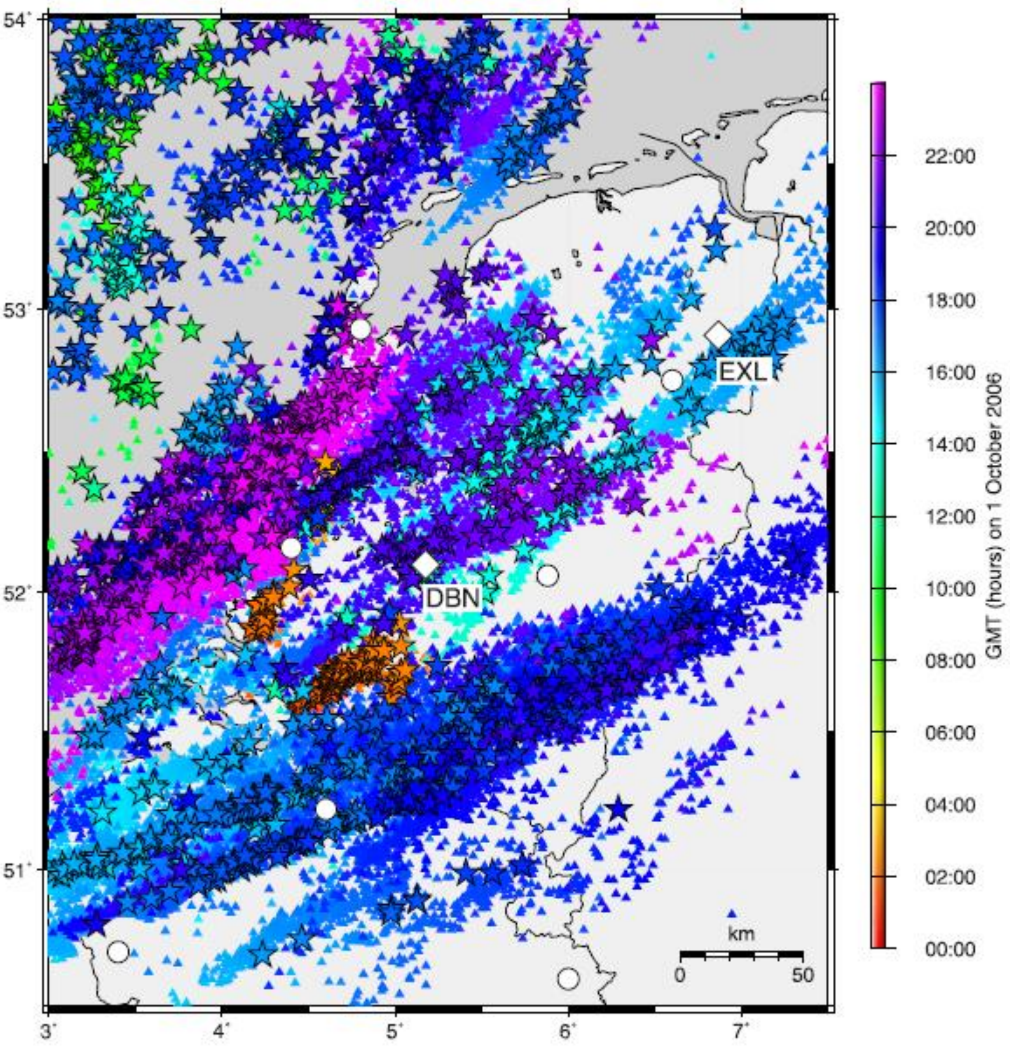

Figure 3-8: Map of the Netherlands, showing lightning activity on 1st October 2006. The stars represent CG discharges, the triangles represent CC discharges, detected by SAFIR. Color represents time of discharge, given in GMT. The SAFIR lightning detection network is plotted with circles; infrasound arrays DBN (De Bilt) and EXL (Exloo) are given. (Assink, et al., 2008)

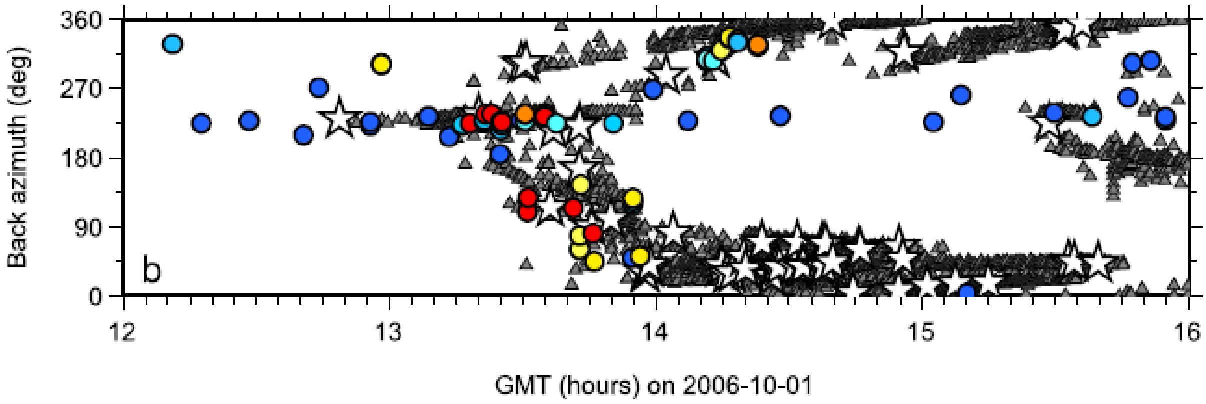

Figure 3-9: Lightning activity detected with SAFIR with infrasound detections (circles) overlaid. (Assink, et al., 2008)

Figure 3-9 shows the lightning activity detected by the SAFIR system representing CC discharges as triangles and CG discharges as stars with infrasound signals detected at DBN and represented as circles. The EM and infrasonic signals seem to correlate well especially between 13:00 and 14:00.

There was also an attempt to show the attenuation behavior of the infrasonic wave. Therefore infrasound amplitudes, peak and through of the infrasonic signal are picked for associated CG discharges within 50km around the two arrays to calculate the average RMS pressure p. Using Eq. [21] the sound energy density is calculated.

$$E = \frac{p^2}{\rho_0 c^2 I_{max}^2 \Delta\tau} \qquad [21]$$

E …… normalized sound energy density
p …… air pressure RMS
ρ_0 ….. air density (1.204kg/m^3 at 1013.25hPa atmospheric pressure and 20°C)
c ……. speed of sound (340m/s)
I_{max} … maximum CG discharge current
$\Delta\tau$ …. duration time of CG discharge

I_{max} and $\Delta\tau$ make up the CG strength and are measured by SAFIR.

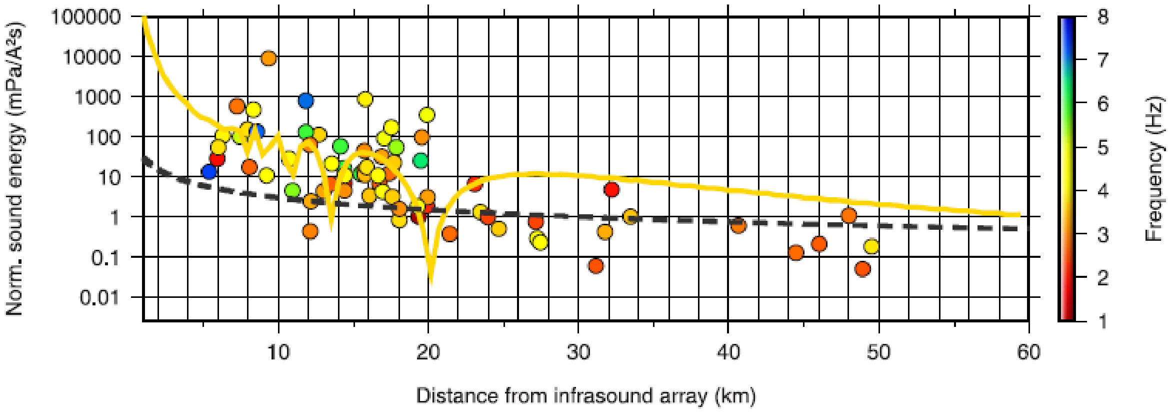

Figure 3-10: Experimental data is represented as circles, the yellow curve represents the model of a 4km long line source and the dashed line is a 1/r curve (Assink, et al., 2008).

Figure 3-10 shows the attenuation of the infrasonic wave due to geometrical spreading modeled for a 4km long line source in tropospheric conditions for f=3.9Hz (yellow line) and the amplitude-distance relation for infrasound from lightning. The amplitude is plotted as sound energy density normalized for CG strength (Assink, et al., 2008).

The credibility of the statement about the data filled into Equation [21] could be impeached for the following reasons:
SAFIR systems don't have calibrated field antennas and therefore the determination of I_{max} is questionable as well as the determination of $\Delta\tau$. The calculation of the energy out of $I_{max}^2 * \Delta\tau$ suggests I_{max} to be constant over $\Delta\tau$ which is not the case.

4. Propagation effects on acoustic signals (Few, 1995)

Once an acoustic pulse is generated it has to propagate through the atmosphere over long distances. Because the atmosphere is a nonhomogeneous, turbulent, anisotropic medium it has several effects on the acoustic signal.

4.1. Finite amplitude propagation

The shape of large amplitude acoustic waves such as thunder must evolve with time. A single pulse evolves to an N-wave (see 2.1) and the N-wave lengthens as is propagates further spreading the total energy over a longer distance. Therefore finite amplitude propagation describes the process of changing waveform with increasing distance to the source. It causes a doubling of the wavelength within the first kilometer but the wavelength remains approximately constant beyond this range if attenuation is not included. Otherwise the stretching of the wavelength would be smaller because of the decreasing wave energy (Few, 1995).

4.2. Attenuation

Attenuation describes the dissipation of wave energy because of the interaction of the sound wave with air molecules and is heavily dependent on the humidity. Therefore differences in results from thunder measurements in coastal areas with high surface humidity and measurements in dry or mountainous areas, where lower humidity is common, might be expected.

The interaction of attenuation with finite amplitude propagation mentioned above is the most important effect on thunder. While the N-wave is continuously attempting to maintain a sharp pressure jump attenuation is most effective for just this condition and produces a more rounded pressure wave.

The total attenuation is insignificant for thunder at frequencies below 100Hz. The high frequencies that can be heard close to the source are never heard at distances beyond a few kilometers (Few, 1995).

4.3. Scattering and Aerosol effects

Aerosols are the largest particles of the cloud and they are responsible for scattering. The scattered part of the incident beam is distributed broadly from the scatterer and therefore removes energy. Higher frequencies are preferentially scattered while the cloud is nearly transparent to low frequency thunder.

Turbulent eddies in the same frequency range as low frequency thunder cause attenuation that will be orders of magnitude greater than any of the effects mentioned before (proportional to ω^2). There is a difference between turbulences close to the receiver and the same turbulence close to the source which has a much greater scattering effect on the wave.

A totally different process of attenuation is due to changes in thermodynamic parameters. During the compressional part of the wave the pressure and air temperature increase while the relative humidity decreases with respect to equilibrium.

Therefore the droplets are partially evaporating in response and withdraw some energy from the wave to accomplish it. This process is very effective at lower frequencies.

Finally there is the mass loading effect that also attenuates the lower frequencies. The fluid displacement produced by an acoustic wave is proportional to 1/ω. Cloud particles with diameter much smaller than the fluid displacement come into dynamic equilibrium with the wave flow and add their mass to effective mass of the air affecting both impedance of the medium and speed of sound. Because of the impedance change the cloud boundary acts as a partially reflector for low frequency acoustic signals and the cloud is dispersive with respect to low frequency waves (Few, 1995).

4.4. Refraction

There are a lot of different refractive effects in the environment of thunderstorms. One of them is refraction due to turbulences. As mentioned in section 4.3 turbulences on the scale of the acoustic wavelength and smaller could be treated with scattering theory. Theoretically turbulences larger than this should be describable by geometric acoustics or ray theory but therefore temperature and velocity of the air at any point between source and receiver need to be known. Because turbulences are closed circulation elements a basic assumption that simplifies the problem can be made. Because of compensation effects there is a zero net effect on the acoustic ray travelling into and out of the turbulent eddy as long as the dimensions of the turbulence is equal or smaller than the path length of the ray.

One of the two strongest refractive effects is the thermal gradient and its influence on the raypath and the audibility of the sound wave discussed in chapter 2.1.

The other strong refractive effect is wind shear that also produces curved raypaths. Wind shear is much more difficult to describe than thermal refraction because of the need of using vectors to describe it compared to scalars used to describe thermal refraction. Close to the surface wind shears during thunderstorms are very strong and can effectively bend the acoustic rays that are nearly parallel to the surface.

Lightning produced infrasound

The purpose of this work is a comparison between lightning parameters and infrasound data. The data and infrasound analysis tools are made available by different organizations. Lightning data are provided by ALDIS (chapter 5). Infrasound data are provided by ZAMG (chapter 7.1), the official CTBTO (chapter 6) contact in Austria. Infrasound data are available for the test site at Conrad Observatory (chapter 8) and for the international monitoring station IS26 (chapter 0).

5. Lightning data provided by ALDIS

*"**ALDIS** (**A**ustrian **L**ightning **D**etection and **I**nformation **S**ystem) is a joint project of OVE, Siemens and Austrian Power Grid AG. The goal of this project is real-time monitoring of lightning activity in the area of Central Europe and providing this information to meteorological services, insurance companies and power utilities. In addition the results of lightning research activities by the ALDIS team are well acknowledged by the international research community and documented in numerous journal papers and conference contributions."* (ALDIS, 2011)

ALDIS provided the lightning parameters data used in this work.

5.1. LLS Methods and data characteristics

The ALDIS network consists of 8 sensors spread across Austria. Each sensor delivers GPS time stamped data to the lightning processor that correlates data of the same lightning stroke based on the time information. To be able to calculate a lightning location at least two sensor messages are required. Additional to the location of each stroke in a flash the lightning processor provides further data such as:

- Time
- Polarity (positive/negative)
- Stroke peak current in kA

The calculation of the location is done by combining the methods of **M**agnetic **D**irection **F**inding (MDF) and **T**ime **O**f **A**rrival (TOA). IMPACT (**IMP**roved **A**ccuracy using **C**ombined **T**echnology) provides the three estimated parameters latitude, longitude and discharge time even when only two sensors provide both time and angle information. (ALDIS, 2011)

Figure 5-1 illustrates the method of MDF using crossed loops (in both north-south and east-west direction) to detect the direction of incidence of the magnetic field and to find the location of the lightning discharge by triangulation. This method requires at least two sensors, if more sensors report a discharge the "angle disagreement" can be minimized.

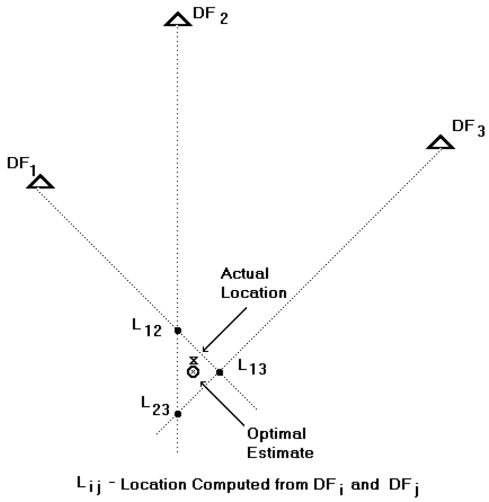

Figure 5-1: Lightning location using MDF **(CIGRE, 2000)**

Figure 5-2 illustrates the method of TOA. A constant difference in the arrival time at multiple stations defines multiple hyperbolas whose intersections define a lightning location. To avoid ambiguity problems (two intersections) at least four sensors should be taken into account.

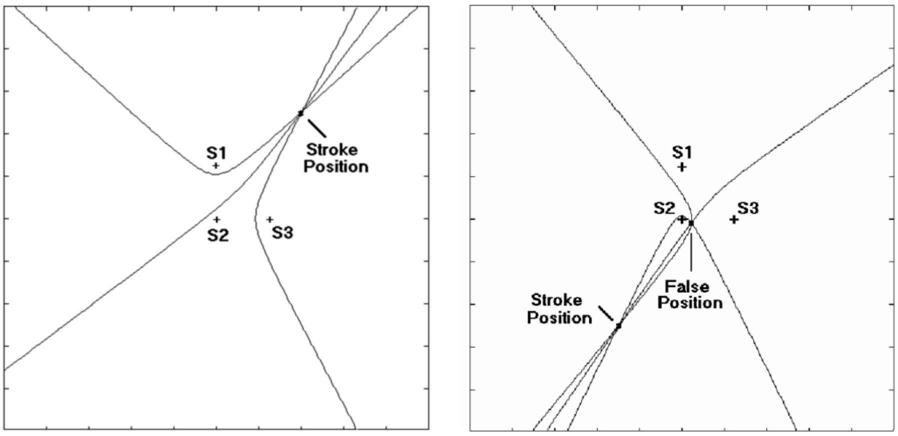

Figure 5-2: Lightning location using TOA method and possibility of false results by using only three sensors **(CIGRE, 2000)**

Because the lightning location system detects stroke-by-stroke a criterion to group strokes into a flash has to be found. Strokes are added to an active flash:

- for a time period of usually 1 second after the first stroke,
- as long as the additional strokes are within a clustering radius of usually 10 km around the first stroke, and
- the time interval from the previous stroke is less than a maximum interstroke interval (usually 500 ms).

In the unlikely event that a stroke is a candidate for more than one flash, it is assigned to the flash with the (spatially) closest first stroke. Additionally, in modern central processors, if a stroke is located more than the clustering radius from the first stroke but is not clearly separated from that stroke because their location confidence regions overlap, then the stroke is included in the flash as shown in *Figure 5-3*.

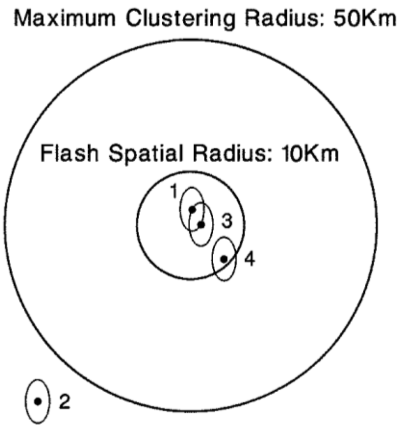

Figure 5-3: Spatial clustering method for grouping strokes into flashes (CIGRE, 2000)

The detection efficiency (fraction of flashes/strokes that are detected by a lightning location system) of ALDIS is 98% for CG flashes and 85% for CG strokes with peak currents higher than 2kA evaluated at Gaisberg tower (CIGRE, 2000).

The accuracy of the observed azimuth by a sensor is about 1° and the resolution of the GPS time is 100ns.

5.2. ALDIS lightning data

To investigate infrasound signals produced by lightning discharges ALDIS allocated a dataset including parameters of lightning discharges within a radius of 50km around Conrad Observatory and IS26 Freyung for August 2010. CO and IS26 were chosen because of their location in Austria and close to the border of Austria, respectively, where ALDIS lightning data is available. The dataset consists of the following parameters:

- Date,
- Time (UTC) accurate to nanoseconds,
- Latitude and Longitude,
- Amplitude in kA,
- Number of strokes and ongoing stroke number in a flash,
- CG or CC,
- Distance to Infrasound Station,
- Azimuth from Infrasound Station to lightning strike point.

An extract of ALDIS lightning data around IS26 is shown in *Table 1*.

The ALDIS system setup as it was in 2010 focused on detection of CG discharges and therefore most of the CC discharges were rejected by the ALDIS system.

Table 1: ALDIS data for IS26 Freyung on August 5th 2010

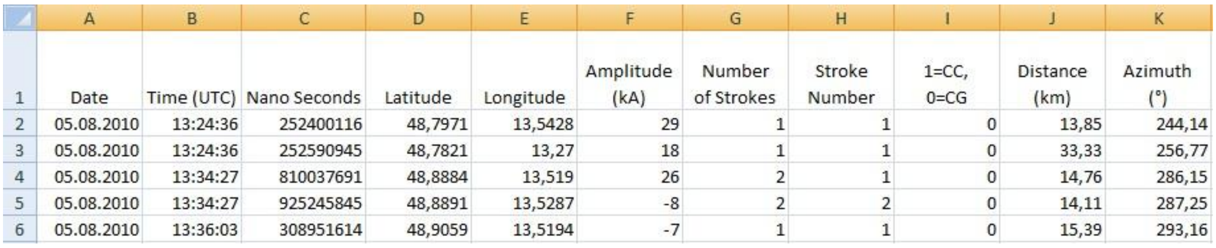

	A	B	C	D	E	F	G	H	I	J	K
1	Date	Time (UTC)	Nano Seconds	Latitude	Longitude	Amplitude (kA)	Number of Strokes	Stroke Number	1=CC, 0=CG	Distance (km)	Azimuth (°)
2	05.08.2010	13:24:36	252400116	48,7971	13,5428	29	1	1	0	13,85	244,14
3	05.08.2010	13:24:36	252590945	48,7821	13,27	18	1	1	0	33,33	256,77
4	05.08.2010	13:34:27	810037691	48,8884	13,519	26	2	1	0	14,76	286,15
5	05.08.2010	13:34:27	925245845	48,8891	13,5287	-8	2	2	0	14,11	287,25
6	05.08.2010	13:36:03	308951614	48,9059	13,5194	-7	1	1	0	15,39	293,16

5.3. Calculation of infrasound arrival time

To search for IS signals produced by lightning discharges it was necessary to get a time window for the signal of interest to be expected to arrive at the IS test site. If the signal travels with the mean velocity of sound, 340m/s according to Assink (Assink, et al., 2008), one can calculate the expected arrival time by dividing the distance (in meters) from ALDIS database by 340m/s. Instead of using a fixed window length of some seconds a minimum and a maximum velocity of 300m/s and 400m/s, respectively, for the IS signal to travel was assumed.

The calculation of the expected arrival times was done with Microsoft Excel. The travel time of the IS wave was calculated as follows:

$$t = \frac{r * 1000}{v * 86400} \qquad [22]$$

t …. travel time of the IS wave in seconds
r …. Distance from ALDIS database in km
v …. 300m/s, 340m/s, 400m/s respectively

Calculation of the time window requires some formal adjustments in EXCEL. 86400 is the number of seconds per day and this value has to be taken into account to set the accordant cells to “[s],00” format. The time (UTC) from ALDIS database has to be changed from “hh:mm:ss” format to “[s],00” format. Now the travel time can be added to time(UTC) and the format of the result has to be changed into “hh:mm:ss,00” to get the time window and the expected arrival time for the given mean velocity v. An extract of the dataset with the results of the calculation is shown in *Table 2*.

Table 2: Calculation of the time window for the IS signal to be expected to arrive at the test site

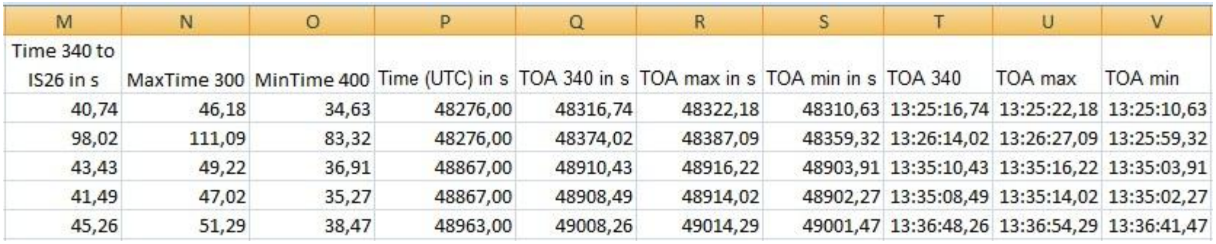

M	N	O	P	Q	R	S	T	U	V
Time 340 to IS26 in s	MaxTime 300	MinTime 400	Time (UTC) in s	TOA 340 in s	TOA max in s	TOA min in s	TOA 340	TOA max	TOA min
40,74	46,18	34,63	48276,00	48316,74	48322,18	48310,63	13:25:16,74	13:25:22,18	13:25:10,63
98,02	111,09	83,32	48276,00	48374,02	48387,09	48359,32	13:26:14,02	13:26:27,09	13:25:59,32
43,43	49,22	36,91	48867,00	48910,43	48916,22	48903,91	13:35:10,43	13:35:16,22	13:35:03,91
41,49	47,02	35,27	48867,00	48908,49	48914,02	48902,27	13:35:08,49	13:35:14,02	13:35:02,27
45,26	51,29	38,47	48963,00	49008,26	49014,29	49001,47	13:36:48,26	13:36:54,29	13:36:41,47

Column “M” in *Table 2* describes the time in seconds that takes the signal to travel the distance from the flash strike point to IS 26 if the signal propagates with 340m/s, while a propagation velocity of 300m/s and 400m/s is assumed for the travel time calculated in column “N” and “O”. The time in column “P” in *Table 2* is the same time as in column “B” in *Table 1* converted into seconds. Adding the different travel times to column “P” yields three different times of arrival of the signal at IS26 shown in column “Q”, “R” and “S”. Those times of arrival have to be converted from seconds to “hh:mm:ss,00” format to get the minimum time of arrival if the signal propagate with 400m/s (column “V”), the maximum time of arrival if the signal propagates with 300m/s (column “U”) and the time of arrival if the signal propagates with 340m/s (column “T”).

6. Infrasound data provided by CTBTO

CTBTO is the shortcut for Comprehensive Nuclear Test Ban Treaty Organization. CTBTO operates the Infrasound Station IS26 Freyung that yields the IS data considered in this work. The CTBTO operates at the moment (November 2011) 70% of the planned 60 Infrasound Stations. One among those stations is Infrasound Station IS26 Freyung located in Germany and data of that station is considered in this work.

6.1. Duties and responsibilities of CTBTO

6.1.1. The Treaty

The Comprehensive Nuclear Test Ban Treaty (CTBT) bans nuclear test explosions by everyone, everywhere. That means that no one is allowed to accomplish nuclear tests on the Earth's surface, in the atmosphere, underwater or underground. It is the aim of the treaty to make it very difficult for countries to develop nuclear bombs for the first time, or for countries that already have them, to make more powerful bombs. It also prevents the huge damage caused by radioactivity from nuclear explosions to humans, animals and plants. At the moment 182 Countries have signed the treaty but some important nuclear technology holder countries are still missing, for example the USA, Iran and others (CTBTO, 2011).

6.1.2. The Organization

CTBTO is an international organization financed by the signatory states. It has a strong technical focus with about 80% of its budget allocated to the establishment of the global verification regime. CTBTO is not part of the United Nations but entered into a relationship agreement with the UN in 2000. This agreement brings CTBTO as an independent organization with its own membership and budget into a formal relationship with the United Nations and provides a framework for cooperation and coordination between the two organizations (CTBTO, 2011).

6.1.3. Verification Regime

The purpose of the verification regime is to detect worldwide all kinds of nuclear explosions and to monitor countries compliance with the treaty. The International Monitoring System (IMS) operated by CTBTO is part of the verification regime and consists of 321 monitoring stations and 16 Radionuclide Laboratories built worldwide. The IMS uses four different technologies to monitor the planet for any sign of a nuclear explosion:

- Seismic monitoring: detection and location of underground nuclear explosions (50 stations sending data continuously in real time and 120 stations upon request only)
- Hydroacoustic monitoring: information about the location of a nuclear explosion underwater, near the ocean surface or near its coasts (11 stations)
- Infrasound monitoring: detection and location of atmospheric and shallow underground explosions (60 stations)
- Radionuclide monitoring: detection of radioactive particles and noble gases in the atmosphere (80 stations and 16 laboratories)

(CTBTO, 2011)

Lightning caused infrasound is a noise signal for the CTBTO IMS based on infrasound monitoring. In the following chapter an overview about the IS technology used by CTBTO is given.

6.2. Sources of Infrasound

Although this work focuses on the infrasonic signals produced by lightning discharges one should keep in mind that, as shown in *Figure 6-1*, there are a lot of different sources of infrasound (natural and manmade) showing different signal characteristics such as waveform, frequency, velocity and so on.

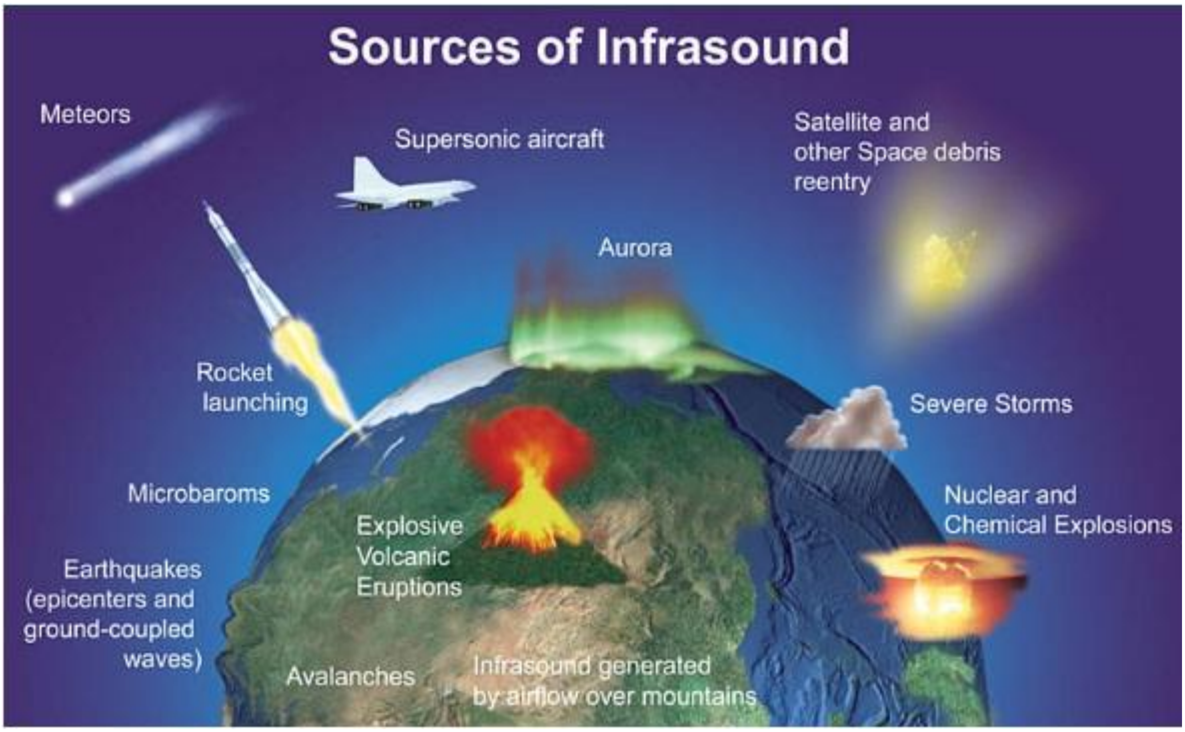

Figure 6-1: Different sources of infrasound (CTBTO, 2011)

6.3. Assembly and operating mode of IMS stations

Where possible, the Infrasound Stations in the IMS network have been established in sheltered areas located well away from infrasonic background noise such as coastal areas, airports, cities, consistently active volcanoes, to mention only some of them.

An IMS Infrasound Station basically consists of:

- Central recording facility (CRF),
- Infrasonic array of several elements with an aperture 1-3km,
- Data transmission system between the elements in the IS array and the CRF,
- Power supply systems (including backup power supply) for the array elements and the CRF,
- An online satellite system (Global Communications Interface, GCI) for the transmission of data in near real time to the International Data Center (IDC) in Vienna, Austria.

Figure 6-2 shows the components mentioned above for an IMS infrasound monitoring station with 7 array elements. A rosette wind-noise reducing system is connected to an infrasonic sensor at each array element and an UHF (Ultra High Frequency) data transmission tower at each element sends the data to the CRF.

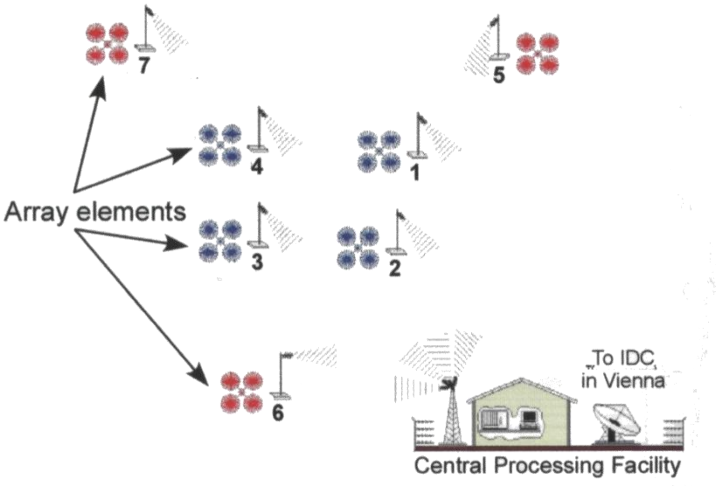

Figure 6-2: Schematic illustration of a typical IMS infrasound monitoring station with 7 array elements **(Le Pichon, et al., 2010)**

Wind-generated noise is by far the most important source of infrasonic background noise in the frequency range of interest (0.02-4Hz). A common method to reduce wind noise is based on spatial averaging of the micropressure field over a limited area surrounding the array element using pipe arrays with a large number of inlet ports. Since pipe arrays integrate the pressure variations at all inlet ports, higher frequency signals may be severely attenuated by large diameter pipe arrays. The degree of attenuation due to this effect is significant at frequencies above 2Hz in the case of 70-m diameter pipe arrays and 8Hz in the case of 18-m diameter pipe arrays (*Figure 6-3*).

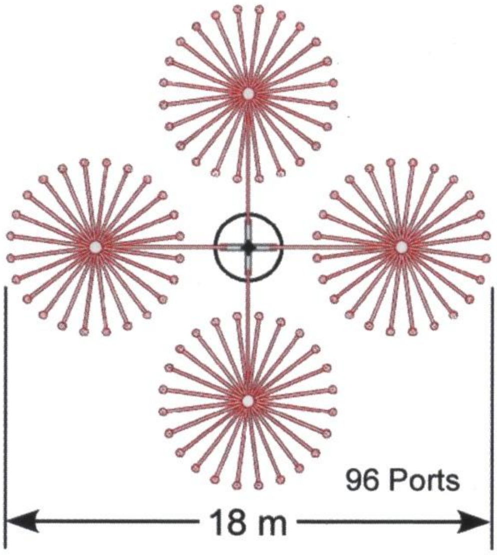

Figure 6-3: Infrasound element in form of a 18m diameter rosette pipe array wind-noise-reducing system with 96 inlet ports as used at IS26 and widely throughout the IMS network (Le Pichon, et al., 2010)

Infrasound sensors microbarometers used in the arrays are installed all over the world at a large range of altitudes. This means that infrasound sensor´s operating pressure range is several orders of magnitude larger than the infrasound range to measure. The sensors also have to be very robust since they have to operate in harsh environmental conditions including for example a very large temperature range (-20°C to 60°C) and no protection against short period temperature variations (Le Pichon, et al., 2010).

The microbarometers used at IS 26 are of type DASE MB2000. MB2000 microbarometers consist in a barometric capsule under vacuum made of so-called Durinval alloy which is deflected by atmospheric pressure variations. This type of capsule can measure pressure fluctuations around ambient pressure (1013hPa at sea level). Measurements are taken in a frequency range extending from continuous (static pressure) to a few tens of Hertz. Capsule micro-deformation (a few tens of nm/Pa) is measured by a high-resolution displacement sensor. The MB2000 can sense pressure variations under 1mPa. It´s instrumental noise is less than 2mPa at [0.02 – 4]Hz. Sensor's sensitivity is generally 20 mV/Pa to adapt it to digitizers range with maximum pressure level ± 5hPa and dynamic range of 108dB. The sampling rate is 20Hz.

As shown in *Figure 6-4*, the upper part of the watertight sensor houses the electronics. The lower part of the sensor consists in the measurement chamber (0.6 liters) containing the barometric capsule and the LVDT (Linear Variable Differential Transformer) displacement sensor. This chamber is connected to ambient pressure by four 10 mm diameter inlets (CEA/DAM, 2009).

Figure 6-4: MB2000 microbarometer (CEA/DAM, 2009)

7. Infrasound data and software tools provided by ZAMG

The ZAMG (Central Institute for Meteorology and Geodynamics) is the Austrian national authority for Meteorology and Geophysics and was founded in 1851.

7.1. ZAMG as the national data center for CTBTO infrasound data

CTBTO operates the IMS and each country that has signed the CTBT has access to the International Data Center (IDC). The national data center of Austria (NDC-AT) is located at ZAMG and requests for particular data can be sent from there.

Conrad Observatory is a part of ZAMG and CTBTO is already using this facility for tests and experimental purposes.

ZAMG also allocated the software tools Antelope and Progressive Multi-Channel Correlation (PMCC) to handle the infrasound data from Conrad Observatory (CO) test site (Antelope) and IS26 Freyung (PMCC).

7.2. Infrasound elements at Conrad Observatory

The Conrad Observatory (CO) is named after the Austrian geophysicist Victor Conrad (1876-1962) who was the first head of Seismological Service of Austria at ZAMG (Central Institute for Meteorology and Geodynamics). CO is located at a nature reserve at Trafelberg just above 1000m altitude 50km southwest of Vienna, Austria. The basic task for CO is the continuous monitoring of physical relevant parameters such as:

- Earthquake activity (seismology),
- Changes in gravity and mass distribution,
- Geomagnetic field variations,
- Geodetic parameters,
- Atmospheric waves,
- Meteorological data.

(Conrad Observatory, 2010)

Besides these geophysical measurements CO hosts an IS test site for CTBTO. The infrasound test site was established by the CTBTO at the CO to assess the efficiency of different geometries of wind noise reducing systems, to test new engineering solutions, and assess the added value deriving from the co-location of infrasound and seismic sensors.

It contains four co-located pipe array elements consisting of two rosettes and two close-packed hexagonal arrays each of them in 18m and 36m diameter (Conrad Observatory, 2010).

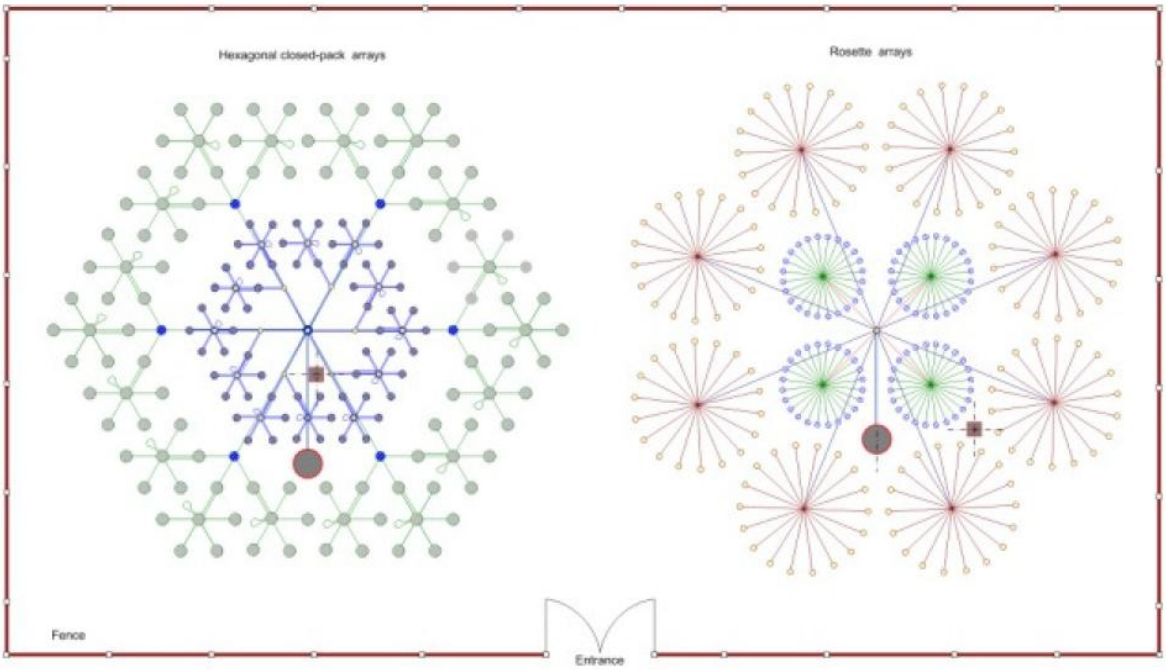

Figure 7-1: CTBTO´s infrasound test wind noise reductions systems and equipment vaults at Conrad test site **(Conrad Observatory, 2010).**

Figure 7-2: General view of the test site (Conrad Observatory, 2010)

7.3. Software used to access and analyze IS data

An infrasound signal arriving at an Infrasound Station with several elements has to pass the wind-noise-reducing system (rosette pipe arrays for example) before it arrives at the microbarometer.

In case of single elements (Conrad Observatory, 2 elements) the recorded data can be displayed directly using a software package called Antelope (8.2).

An array of sensors (IS26 Freyung, 5 elements) allows more sophisticated signal processing using Progressive Multi-Channel Correlation (9.2).

A flowchart of IS data processing as used throughout this work is given in *Figure 7-3*.

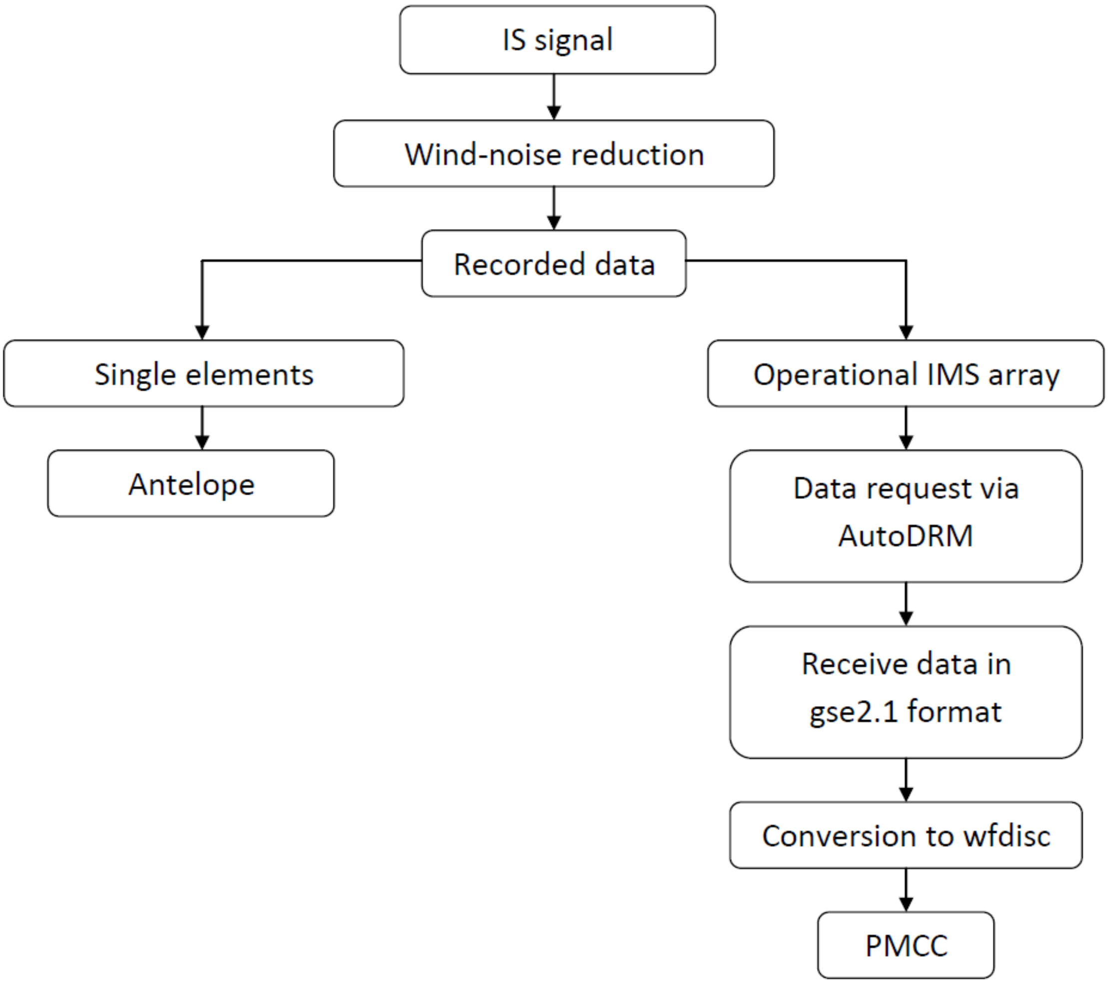

Figure 7-3: Flowchart of data processing for single elements (Conrad Observatory) and operational IMS arrays (IS26 Freyung).

Evaluation of observed datasets

8. Conrad Observatory

CO is located at a nature reserve at Trafelberg just above 1000m altitude 50km southwest of Vienna, Austria and hosts an IS test site for CTBTO. It contains four co-located pipe array elements consisting of two rosettes and two close-packed hexagonal arrays as shown in *Figure 7-1*.

8.1. CO data

The Austrian Lightning Detection and Information System (ALDIS) provided a database of strokes which occurred in the month August 2010 within a radius of 50km around CO.
There was a number of thunderstorms and high lightning activity in the area of CO in August 2010. The database contains 15697 strokes from August 1st to August 24th.

Lightning information of August 5th 2010 was chosen from ALDIS database to have a look at possible infrasonic signals at CO test site. This particular date was chosen because of the moderate lightning activity. For days with a high activity infrasonic signals are overlapping. ALDIS located 706 lightning strokes on this day, 618 CG and 88 CC strokes within a range of 50km around CO.

Based on the distance to CO a possible time window for the arrival of the infrasound signal at the station was calculated using two sound velocities (min=300m/s, max=400m/s) as described in section 0. Based on studies from Assink et al (2008) a mean velocity of 340m/s for stroke signals was assumed. All signals arriving with a velocity of 340m/s are supposed to be in the chosen timeframe.

8.2. Antelope

Antelope is a software package designed for data collection and seismic data analysis. Antelope runs for example in an UNIX environment on Sun Solaris and has an open architecture that already supports many common dataloggers and sensors, but other dataloggers, sensors, and novel devices may be integrated by the end user (Boulder Real Time Technologies, 2011).

The software package can be as well used to display IS data and was used to display IS data from Conrad Observatory in this work.

8.3. Observation of IS signals

Infrasound data from CO was depicted using the software package Antelope (chapter 8.2).

There were three different filters applied to the IS data during evaluation:

- FERN (0.3Hz-6Hz),
- NAH (>1Hz),
- HELI (1Hz-10Hz).

The channels show different parameters for each of the two elements I99V1 and I99V2:

BDA: absolute pressure,
BKO: temperature,
BWD: wind direction,
BWS: wind speed.

Figure 8-1 shows the information gathered during a 5-minutes time interval at the two arrays and the amplitudes and expected arrival times for 11 lightning strokes. The expected arrival time was calculated as shown in section 0.

Figure 8-2, *Figure 8-3* and *Figure 8-4* show a zoom into the signals around the first red line labeled “66kA” in *Figure 8-1* using the different filters described above. The expected arrival time windows were calculated for sound velocities 400m/s (T_{min}), 340m/s (T_{340}) and 300m/s (T_{max}) respectively.

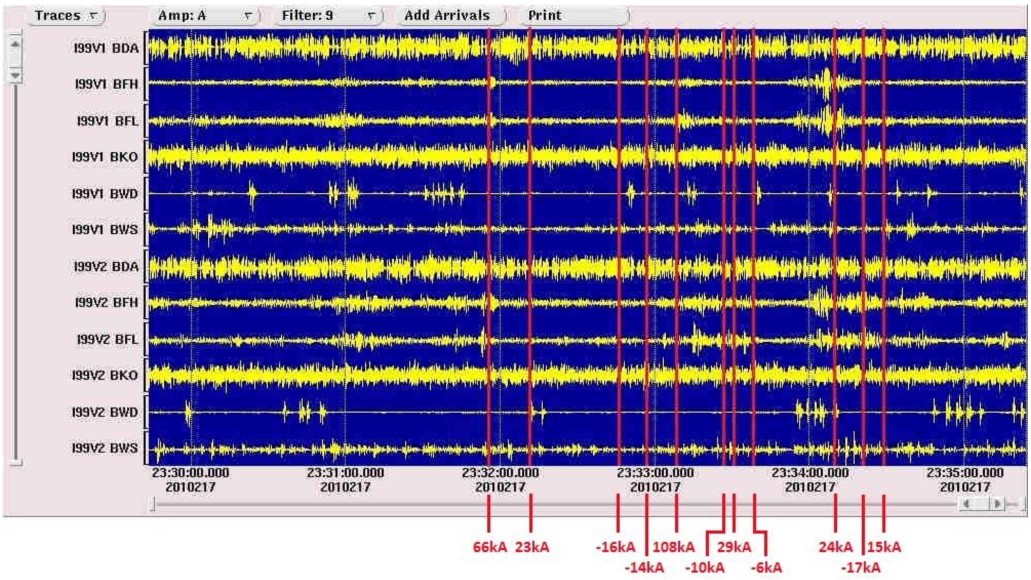

Figure 8-1: 5-minutes-interval showing the channels described above and the expected arrival times for eleven lightning strokes with their amplitudes

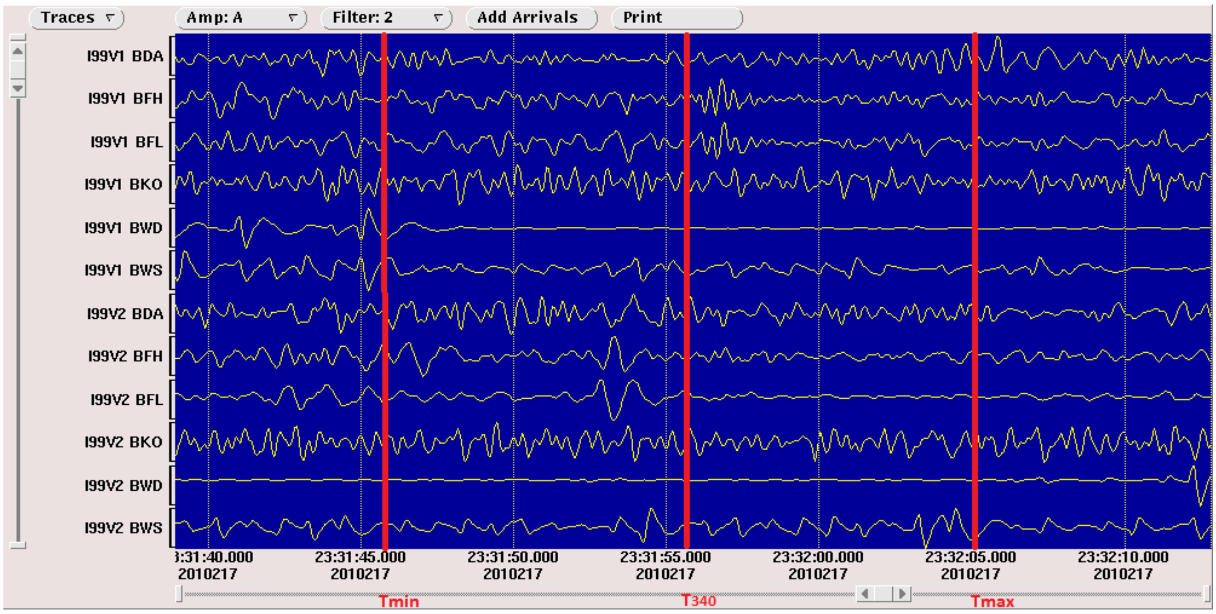

Figure 8-2: Zoom into the time frame for the lightning stroke with 66kA amplitude using Filter FERN

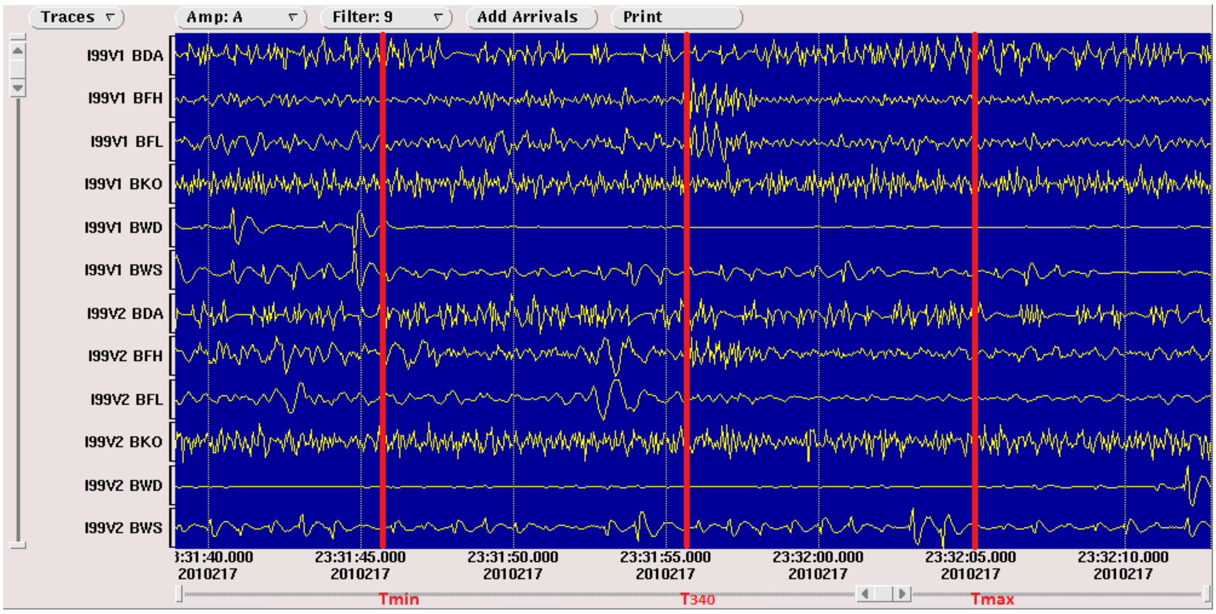

Figure 8-3: Zoom into the time frame for the lightning stroke with 66kA amplitude using Filter HELI

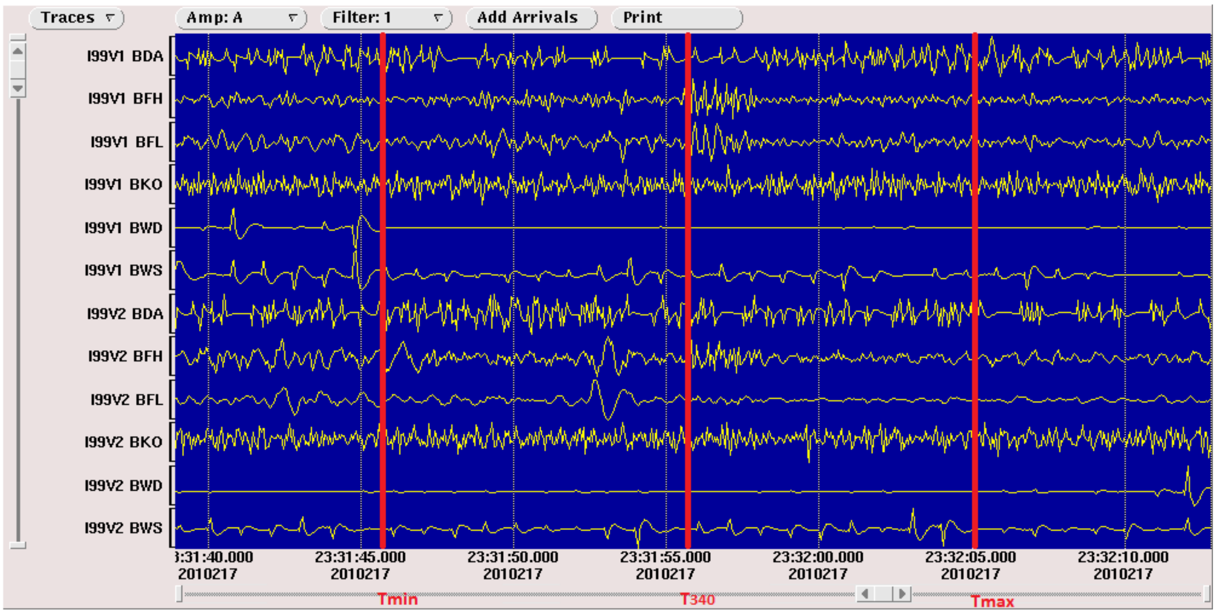

Figure 8-4: Zoom into the time frame for the lightning stroke with 66kA amplitude using Filter NAH

9. Freyung (IS26)

Infrasound Station IS26 Freyung is an infrasound monitoring station in the operating network of the CTBTO. It is located in Germany / Bavaria close to the border of Austria and Czech Republic as shown in *Figure 9-1*. IS26 is an array of 5 microbarometers H1 to H5 located in a forest to avoid background noise as much as possible. The array extends about 2.5km from east to west (H3-H5) and 2km from north to south (H2-H4) as shown in *Figure 9-2*.

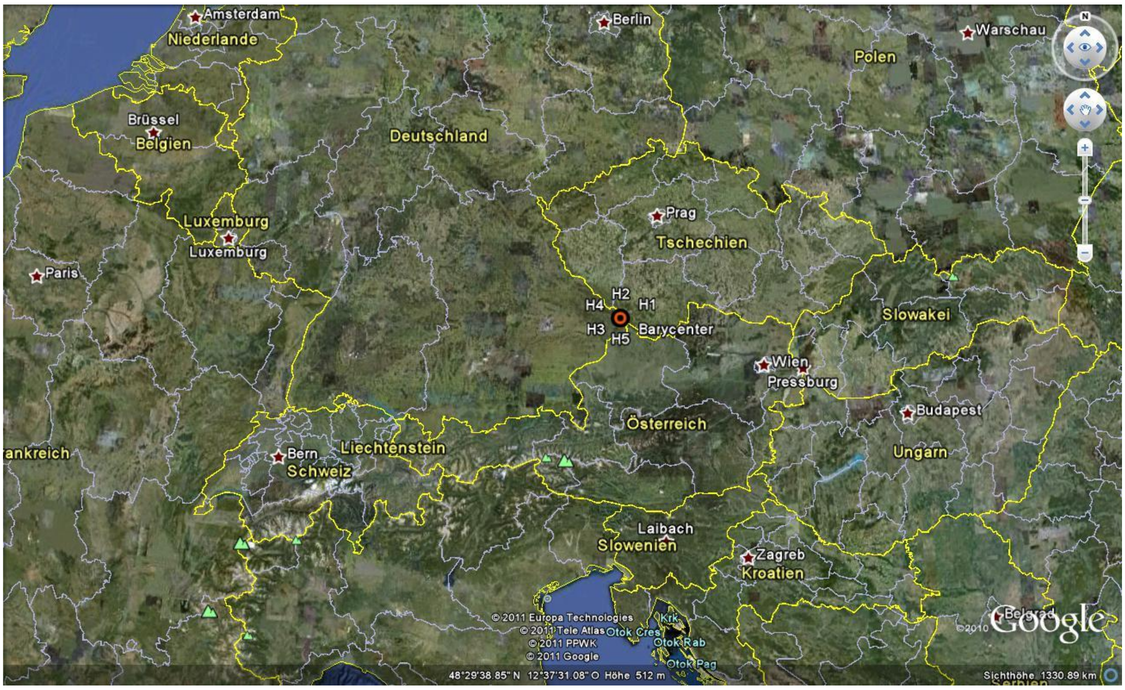

Figure 9-1: Geographical location of IS 26

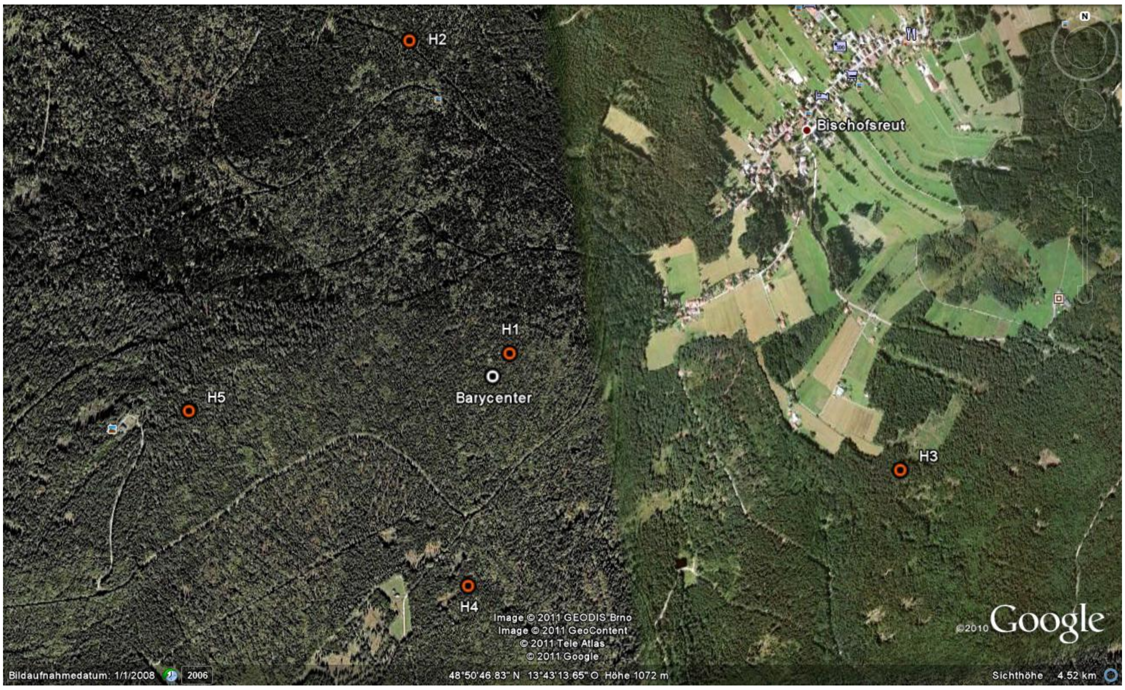

Figure 9-2: Geometry of IS 26 array with 5 elements H1, H2, H3, H4 and H5

9.1. IS26 data

The Austrian Lightning Detection and Information System (ALDIS) provided a database of strokes which occurred in the month August 2010 within a radius of 50km around IS26.
There was a number of thunderstorms and high lightning activity in the area of IS26 in August 2010. The database contains 1441 strokes from August 2nd to August 24th.

First studies were accomplished for 5th of August 2010. This particular date was chosen because of the moderate lightning activity. For days with a high activity infrasonic signals are overlapping. Altogether 387 lightning strokes were detected on the selected day of August 5th, 2010.

Based on the distance to IS26 a possible time window for the arrival of the infrasound signal at the station was calculated using two sound velocities (min=300m/s, max=400m/s) as described in section 0. Based on studies from Assink et al (2008) a mean velocity of 340m/s for stroke signals was assumed. All signals arriving with a velocity of 340m/s are supposed to be in the chosen timeframe.

9.2. Progressive Multi-Channel Correlation

9.2.1. Pre-processing of IS data

Selected IS data was obtained via AutoDRM (Automatic Data Request Manager) from the CTBTO using gse2.1 format. After conversion of the data into wfdisc format using already existing scripts in an UNIX environment the data was transferred to the program Progressive Multi-Channel Correlation (PMCC) where it was further processed.

9.2.2. PMCC (Cansi, et al., 2003)

In case of a network of IS sensors the signals can be quite different from one sensor to another. In a dense array of sensors (H1, H2, H3, H4, H5) the aperture is of the order of the wavelengths of the signals of interest and one can take advantage of the great similarity of the signals. A temporal signal s(t) is represented by its Fourier transform

$$\mathrm{S(f)} = A(f)e^{i\varphi(f)} \qquad [23]$$

A(f) …. spectral amplitude
φ(f) …. phase

The background noise is characterized by a rapid variation of both spectral amplitude and phase from one sensor to another while the signal is not deformed at all and the only difference between the signals arriving at different sensors is a time delay depending on the relative positions of the sensors. If a planar wave is assumed this time delay is the same for all frequencies and it is determined with the correlation function. The correlation function determines in a given time window the similarity of the signals when shifted in time and yields values ranging from -1 to 1. The maximum of the correlation function gives the time delay between the signals.

The analysis is initialized on the smallest group of three sensors to avoid ambiguity problems when correlating records from sensors too far apart. The correlation function yields the propagation time Δt_{ij} between sensor i and sensor j.

For each subnetwork (i,j,k) the closure relation

$$\Delta t_{ij} + \Delta t_{jk} + \Delta t_{ki} = 0 \quad [24]$$

should be obtained. Because the delays measured in case of background noise are a result of random phase combinations the closure relation shown in Eq. [24] is no longer valid.

The consistency of the set of delays obtained using all the sensors R_n is defined as the mean quadratic residual of the closure relations. A detection is observed on R_n if this consistency is below a given threshold.

To remove false detections that could be due to correlated noise and a better estimation of the wave parameters distant sensors are progressively added to increase the array aperture. The final solution is given by the biggest subnetwork. *Figure 9-3* shows the optimized configuration of 4 initial subnetworks of IS26 Freyung. Each subnetwork consists of 3 sensors building up equilateral triangles with small aperture in the best case. *Figure 9-4* shows the flowchart of the whole detection process of IS signals described above (Cansi, et al., 2003).

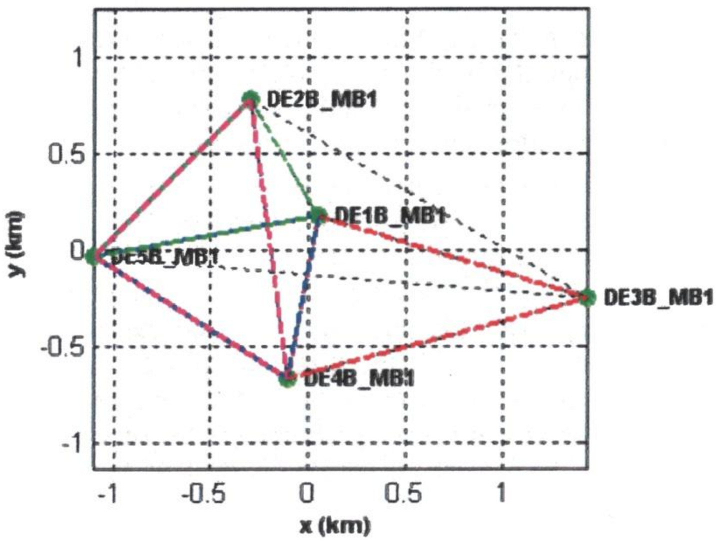

Figure 9-3: Selection of 4 initial subnetworks of the IMS Infrasound Station IS26 in Freyung **(Cansi, et al., 2003)**

Subnetwork 1: DE1B_MB1- DE2B_MB1- DE5B_MB1

Subnetwork 2: DE1B_MB1- DE4B_MB1- DE5B_MB1

Subnetwork 3: DE2B_MB1- DE4B_MB1- DE5B_MB1

Subnetwork 4: DE1B_MB1- DE3B_MB1- DE4B_MB1

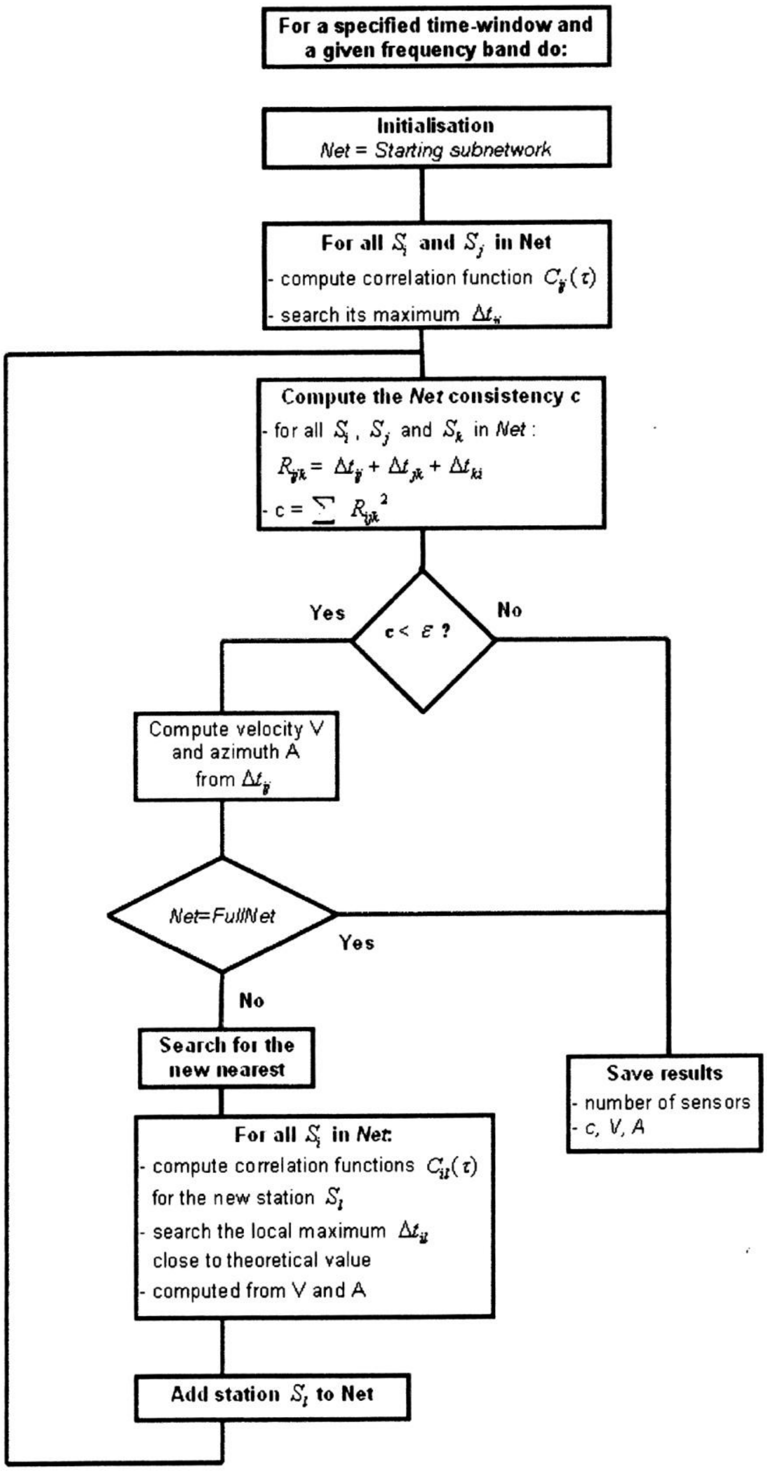

Figure 9-4: PMCC flowchart describing the process of detection of an infrasound signal (Cansi, et al., 2003)

Figure 9-5 shows the main control panel of the PMCC software. In a first step the configuration needs to be created. Detection and Filter parameters can be filled in the window “Parameters” and a filter was set to 0.1-4Hz in a first attempt. The “Network Settings” were set as shown in *Figure 9-3*. After setting the main parameters the calculation was started.

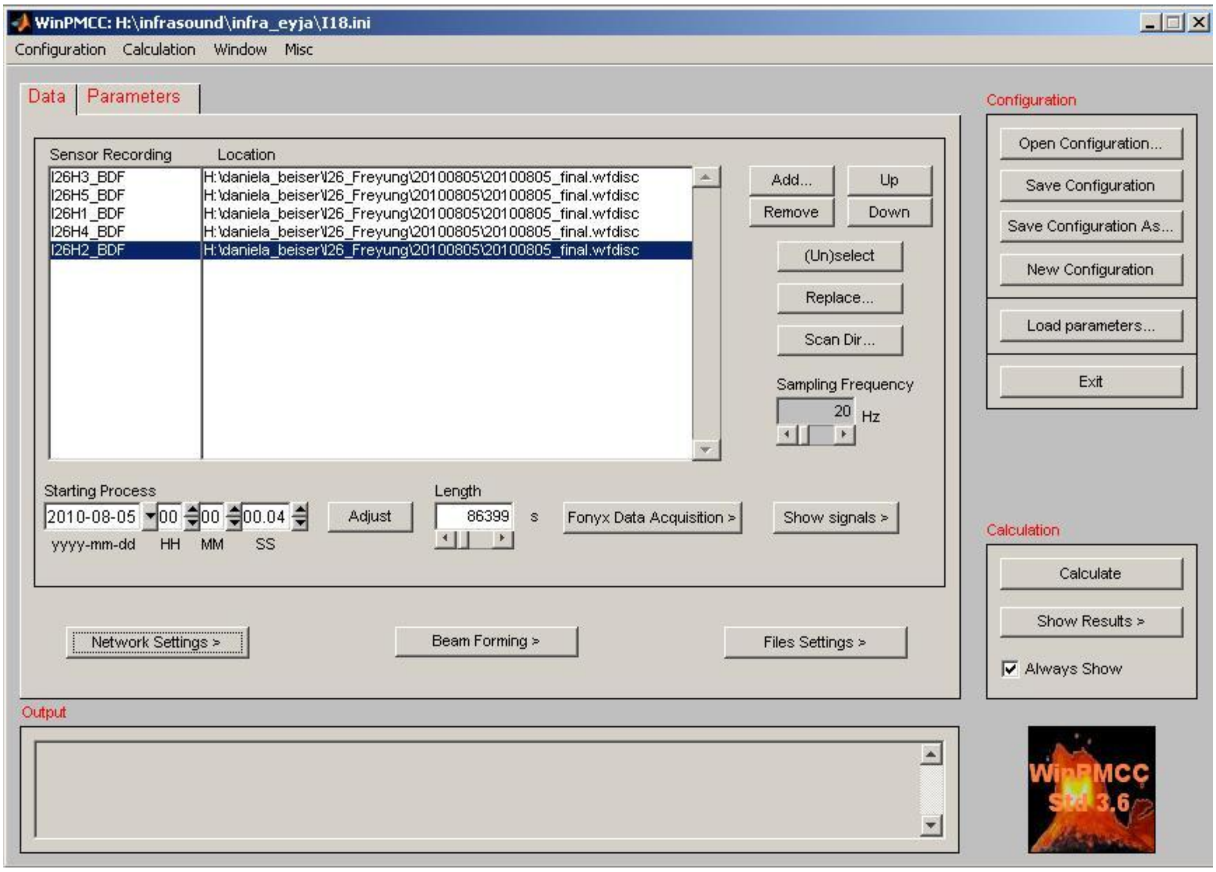

Sensor Recording	Location
I26H3_BDF	H:\daniela_beiser\I26_Freyung\20100805\20100805_final.wfdisc
I26H5_BDF	H:\daniela_beiser\I26_Freyung\20100805\20100805_final.wfdisc
I26H1_BDF	H:\daniela_beiser\I26_Freyung\20100805\20100805_final.wfdisc
I26H4_BDF	H:\daniela_beiser\I26_Freyung\20100805\20100805_final.wfdisc
I26H2_BDF	H:\daniela_beiser\I26_Freyung\20100805\20100805_final.wfdisc

Sampling Frequency 20 Hz

Starting Process 2010-08-05 00 00 00.04 (yyyy-mm-dd HH MM SS)

Length 86399 s

☑ Always Show

Figure 9-5: Main control panel of PMCC

The output of the program (a click on the button "Calculate") yields the pressure over time plot for the five sensors with applied filter settings as well as calculated azimuth and speed gained from cross-correlation as shown in *Figure 9-6* for example.

Radar plot

With this tool any of the parameters of a selected sample can be displayed in a polar plot. The distance of each point to the center of the radar ("RADIUS PARAMETER") and the color of each point ("COLORBAR PARAMETER") can depend on the following parameters:

- Time (by default),
- Frequency,
- Speed,
- Amplitude,
- Correlation,
- Consistency,
- Number of sensors.

(Pouillot, 2008)

An example for the output of this tool is shown in *Figure 9-7*.

Align waveforms

The align waveforms tool is used to display the signals from at least 2 sensors with an offset calculated to align the waveforms in time. The signals displayed in the result panel are aligned with the mean azimuth and mean speed of the selected zone (Pouillot, 2008) as shown in *Figure 10-2* for example.

Spectrogram

The spectrogram tool generates a two dimensional graph with time on the x- axis and frequency on the y- axis. A third dimension indicates the amplitude in dB of a particular frequency at a particular time using colors varying from blue to red. The amplitude in dB (P_{dB}) is calculated as follows:

$$P_{dB} = 20 * \log_{10} \frac{P}{P_0} \qquad [25]$$

P …. amplitude in Pa
P_0… reference value in Pa

An example for the output of this tool is shown in *Figure 10-5*.

9.3. Observation of IS signals

9.3.1. Relating IS to lightning measurements

The PMCC calculation as described in chapter 9.2.2 yields the pressure over time plot for all five microbarometers with applied filter settings, as well as calculated azimuth and speed of the arriving infrasonic signal in the time/frequency domain in case of coherent signals gained from cross-correlation as shown in *Figure 9-6*.

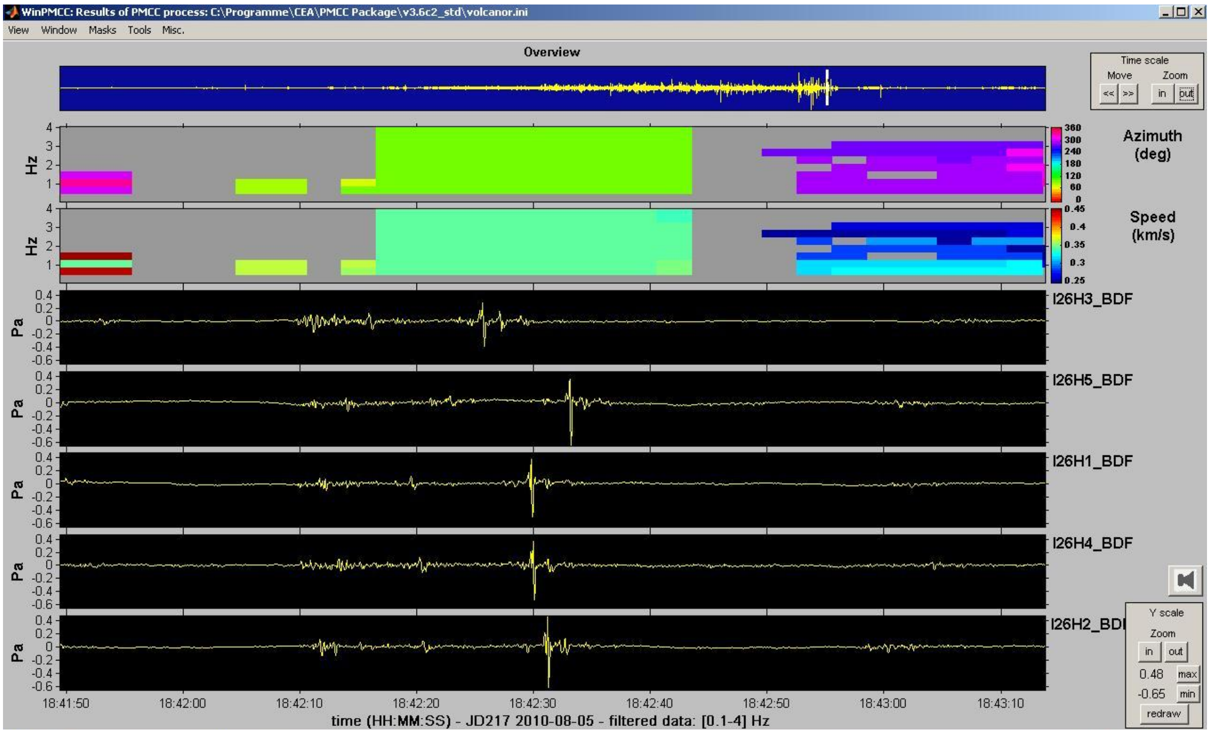

WinPMCC: Results of PMCC process: C:\Programme\CEA\PMCC Package\v3.6c2_std\volcanor.ini

Y scale: 0.48 max, -0.65 min

Figure 9-6: Pressure variations for the five sensors with azimuth and velocity.

Figure 9-7 shows the parameters speed and frequency of selected samples in a radar type plot.

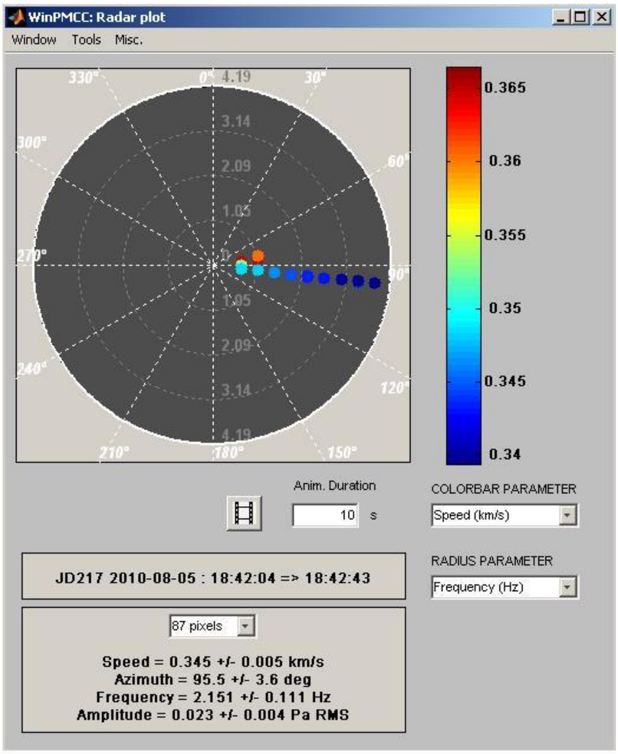

WinPMCC: Radar plot

Anim. Duration 10 s

COLORBAR PARAMETER: Speed (km/s)

RADIUS PARAMETER: Frequency (Hz)

JD217 2010-08-05 : 18:42:04 => 18:42:43

87 pixels

```
Speed = 0.345 +/- 0.005 km/s
Azimuth = 95.5 +/- 3.6 deg
Frequency = 2.151 +/- 0.111 Hz
Amplitude = 0.023 +/- 0.004 Pa RMS
```

Figure 9-7: Radar type plot for the signal shown in Figure 9-6.

The infrasonic signal shown in *Figure 9-6* and *Figure 9-7* corresponds to a positive CG flash with one stroke and a peak current of 31kA detected on the 5th of August 2010 at 18:42:02. The distance to IS26 is 13.85km and the infrasonic signal is expected to arrive in a time window between 18:42:25.73 and 18:42:33.64. If the signal travels with a mean velocity of 340m/s it should arrive at the array at 18:42:29.92. The radar plot indicates that the signal arrives slightly faster than the mean velocity with 345 m/s. Significant pressure variations in *Figure 9-6* around 18:42:30 are in good agreement with the arrival time expected.
The azimuth of the IS signal is 95.5+/-3.6 deg and agrees well to the azimuth of 104.04 deg calculated based on the ALDIS location of the flash.

According to the work of Assink (Assink, et al., 2008) the azimuth observed from the evaluation of the IS-Signal can deviate up to 10 deg compared with the azimuth calculated based on the ALDIS location of the flash.

The general structure of the pressure pulse agrees to the theory developed by Dessler and Bohannon (Bohannon, 1980) that predicts infrasonic sound signals originating from an electrostatic mechanism with the waveform shown in *Figure 3-1*.

For each lightning strike which occurred on 5th of August 2010 and its expected arrival time at station IS26 the pressure signals were examined according to the following criteria:

- Was there a coherent signal from the calculated azimuth and significant pressure variation?
- Was there only a coherent signal?
- Were there only pressure variations?

If for a given flash at least one of the former criteria was fulfilled a screenshot of the pressure signals and the corresponding radar plot was taken as documentation and for further evaluation in chapter 10.4.

9.3.2. Changing PMCC parameters

In some cases the thunder signature was superposed on very low frequency signals as shown in *Figure 9-8*. In order to reduce this low frequency noise signal the filter parameters of the bandpass filter were set to 0.4-4Hz instead of 0.1-4Hz. *Figure 9-9* and *Figure 9-10* illustrate the filter response for the observations described above and the new filter settings. *Figure 9-11* shows the same IS signal as *Figure 9-8* when the other filter settings were applied. The number of frequency bands to be processed (10) remained the same.

The number of frequency bands defines the frequency width of the pixels in the time/frequency domain and therefore is used to discretize the continuous frequency range. A reasonable number of frequency bands for a frequency range of one decade is 10 (Cansi, et al., 2003) as used throughout this work. Increasing the number of frequency bands leads to increasing resolution in the time/frequency domain but also increases the required calculation time.

Figure 9-9 and *Figure 9-10* show the differences in amplitude response and phase response occurring due to the changed filter parameters. Because of the frequency bands being equally spaced and the number of frequency bands remaining the same but the frequency range being changed, the space in between the frequency bands shown in *Figure 9-10* is slightly tighter than in *Figure 9-9*.

While the passband of band no.10 stays at the same frequency range for both filter settings the passband of band no.1 starts at 0.1Hz in *Figure 9-9* and at 0.4Hz in *Figure 9-10*.

Another option to improve the resulting signal quality was the optimization of the subnetwork configuration (*Figure 9-3*). PMCC delivers the best results for equilateral triangles (Cansi, et al., 2003).

The IS signal shown in *Figure 9-8* and *Figure 9-11*, respectively, corresponds to a positive CG flash containing one stroke with 26kA amplitude. The distance to I26 was 13.85km and the azimuth 244.14° according to ALDIS data. The flash was detected at 13:24:36 and the IS signal is expected to arrive in a time window between 13:25:10.63 and 13:25:22.18 at I26. Travelling with 340m/s it would arrive at 13:25:16.74. In *Figure 9-11* frequencies between 0.1Hz and 0.4Hz that are seen in *Figure 9-8* are filtered off to reduce the long-wave signals that are considered to be noise in this case.

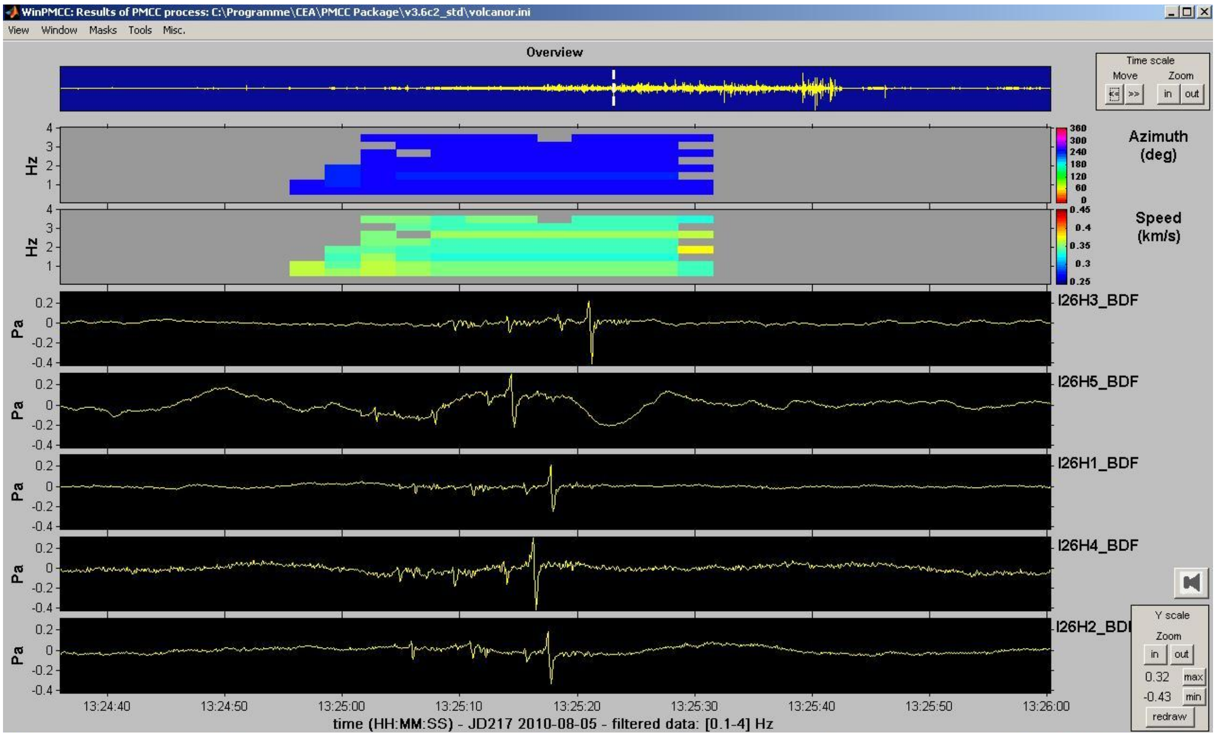

Figure 9-8: IS signature showing filtered data (0.1-4Hz)

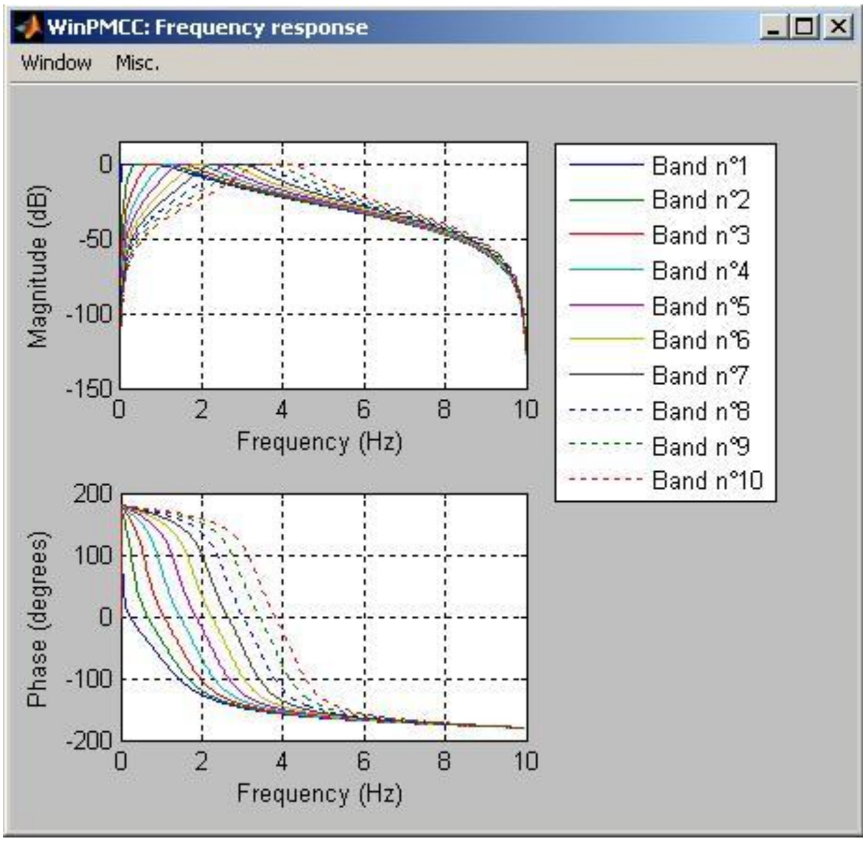

Figure 9-9: 0.1-4Hz filter response for 10 frequency bands

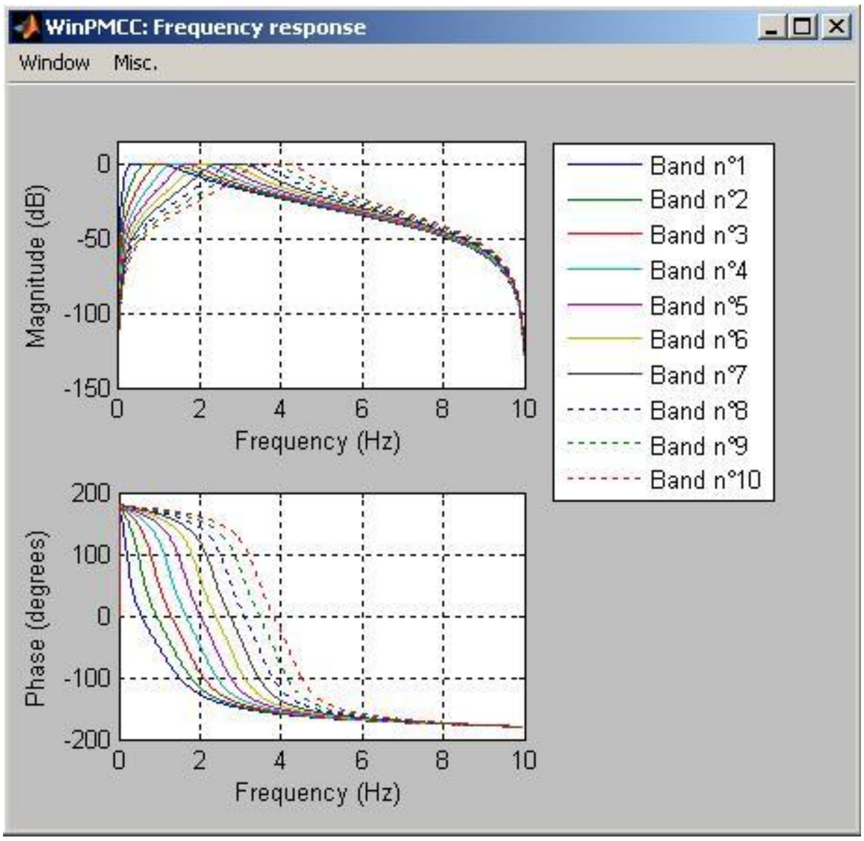

Figure 9-10: 0.4-4Hz filter response for 10 frequency bands

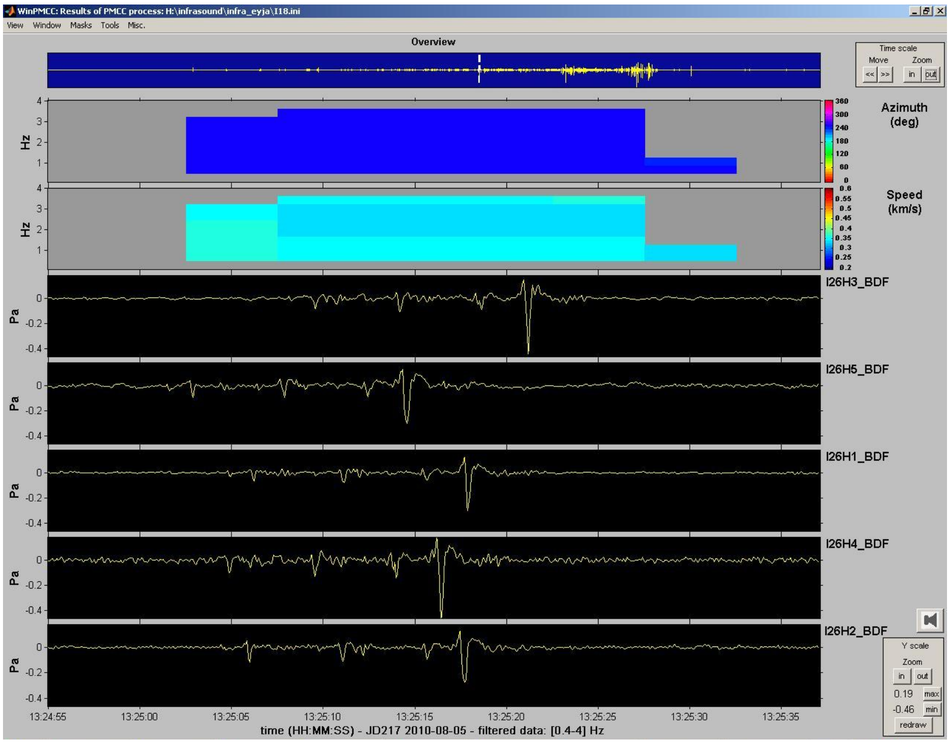

Figure 9-11: The same IS signature as shown in Figure 9-8 but filtered as shown in Figure 9-10.

10. Analysis of signals from different sources

In order to figure out if there are common characteristics in signals originating from CG/CC flashes or single/multiple stroke flashes another observation was started considering only category a) signals that are characterized by a significant pressure variation and the azimuth that agrees closely (+/-10deg) to ALDIS azimuth (chapter 10.4). PMCC configuration is set as described above.

- Pressure variations,
- time-aligned waveforms,
- radar plots with different parameters (speed as radius parameter, time as colorbar parameter and frequency as radius parameter, speed as colorbar parameter) and
- spectrograms

are plotted for a CG single stroke flash, a CG flash with two strokes and a CC discharge.

10.1. Single stroke CG flash

Figure 10-1 to *Figure 10-5* show IS signals produced by a positive single stroke flash.

Table 3: Lightning parameters from ALDIS dataset for a single stroke flash

Time (UTC)	18:42:02
Amplitude	+31kA
Distance	9.49km
Azimuth	104.04°
TOAmin (400m/s)	18:42:25,73
TOA (340m/s)	18:42:29.92
TOAmax (300m/s)	18:42:33.64

The waveform of the infrasonic rarefaction pulse generated by a positive single stroke CG flash as shown in *Figure 10-1* and *Figure 10-2* agrees to the theory of the electrostatic source as described in chapter 0. The arrival time at the IS station is in good agreement with the calculated arrival times as shown in *Figure 10-3*. *Figure 10-4* shows that the azimuth of the IS signals is in good agreement with the azimuth from ALDIS and the propagation velocity over the array is around 340m/s as it is expected to be. *Figure 10-3* and *Figure 10-4* show an additional signal from unknown source coming from slightly different azimuth, propagating faster and arriving earlier. Although the azimuth of the unknown source has been identified the distance to IS26 is still unknown. *Figure 10-5* illustrates the relatively low background noise and the IS signal standing our clearly from the background.

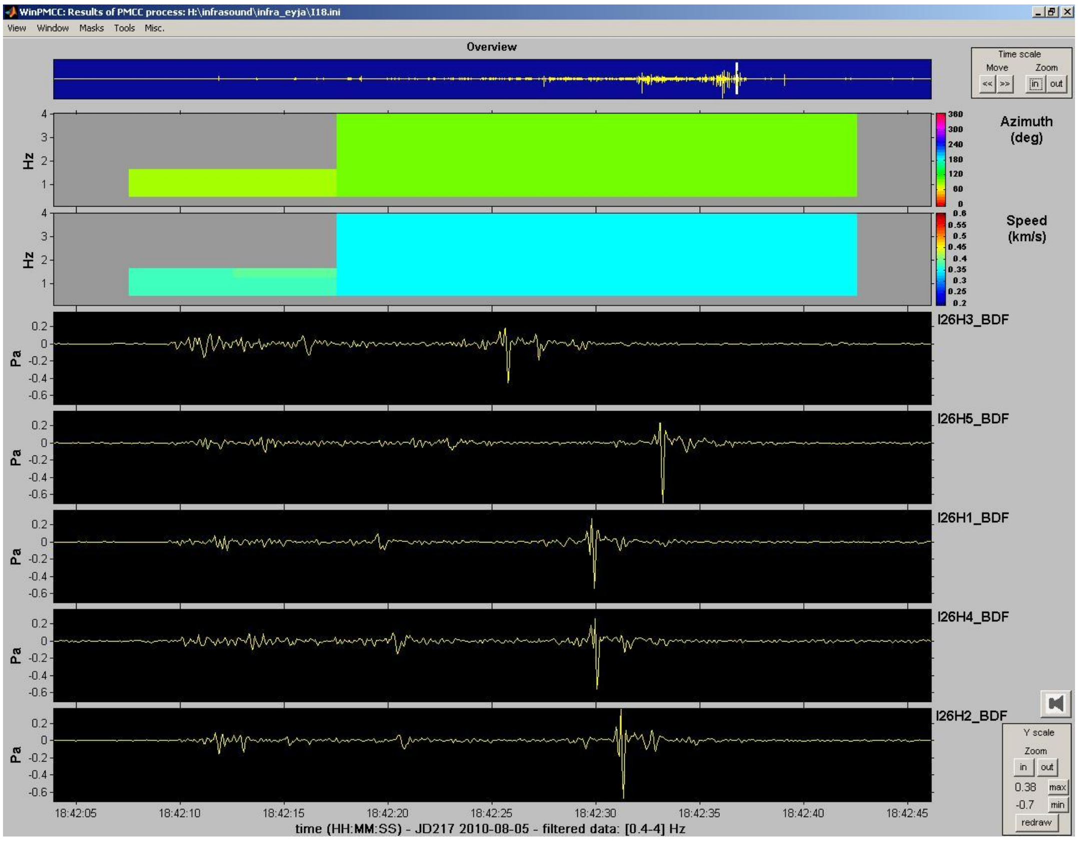

Y scale: max 0.38, min -0.7

Figure 10-1: Pressure variations generated by a single stroke flash

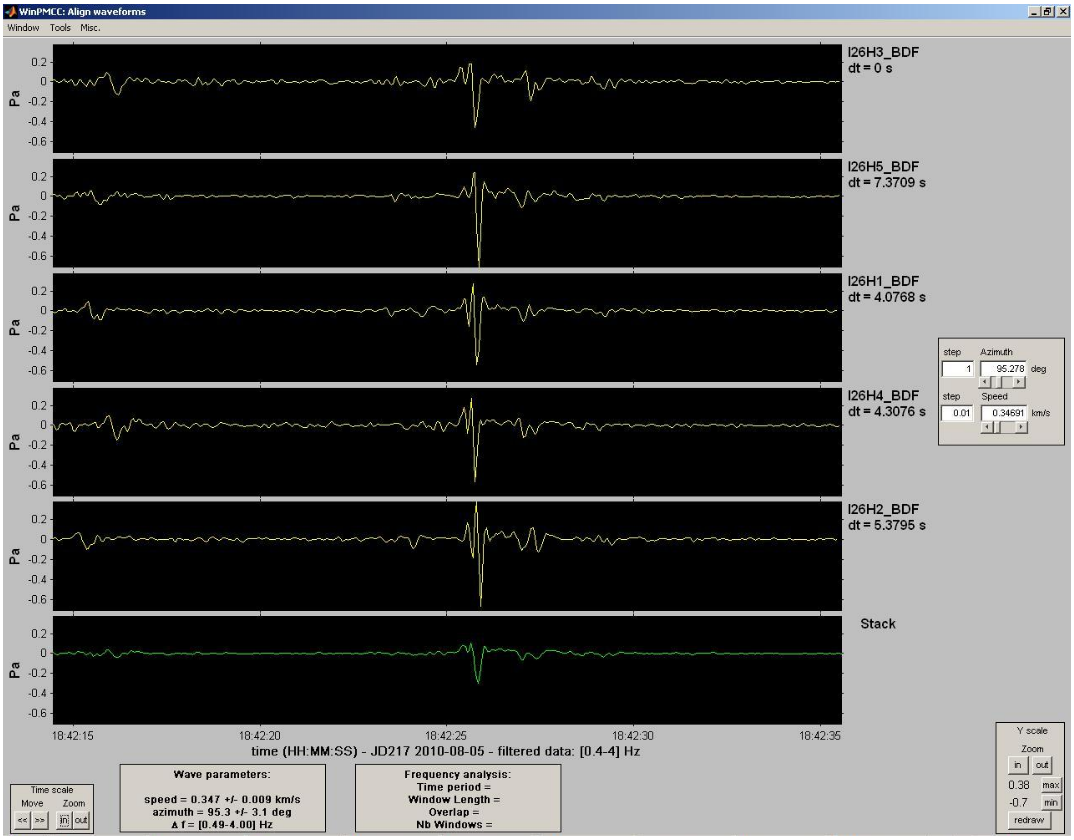

I26H3_BDF dt = 0 s

I26H5_BDF dt = 7.3709 s

I26H1_BDF dt = 4.0768 s

I26H4_BDF dt = 4.3076 s

I26H2_BDF dt = 5.3795 s

Azimuth: step 1, 95.278 deg

Speed: step 0.01, 0.34691 km/s

Y scale: max 0.38, min -0.7

Wave parameters:

speed = 0.347 +/- 0.009 km/s
azimuth = 95.3 +/- 3.1 deg
Δ f = [0.49-4.00] Hz

Frequency analysis:
Time period =
Window Length =
Overlap =
Nb Windows =

Figure 10-2: Time-aligned signals generated by a single stroke flash

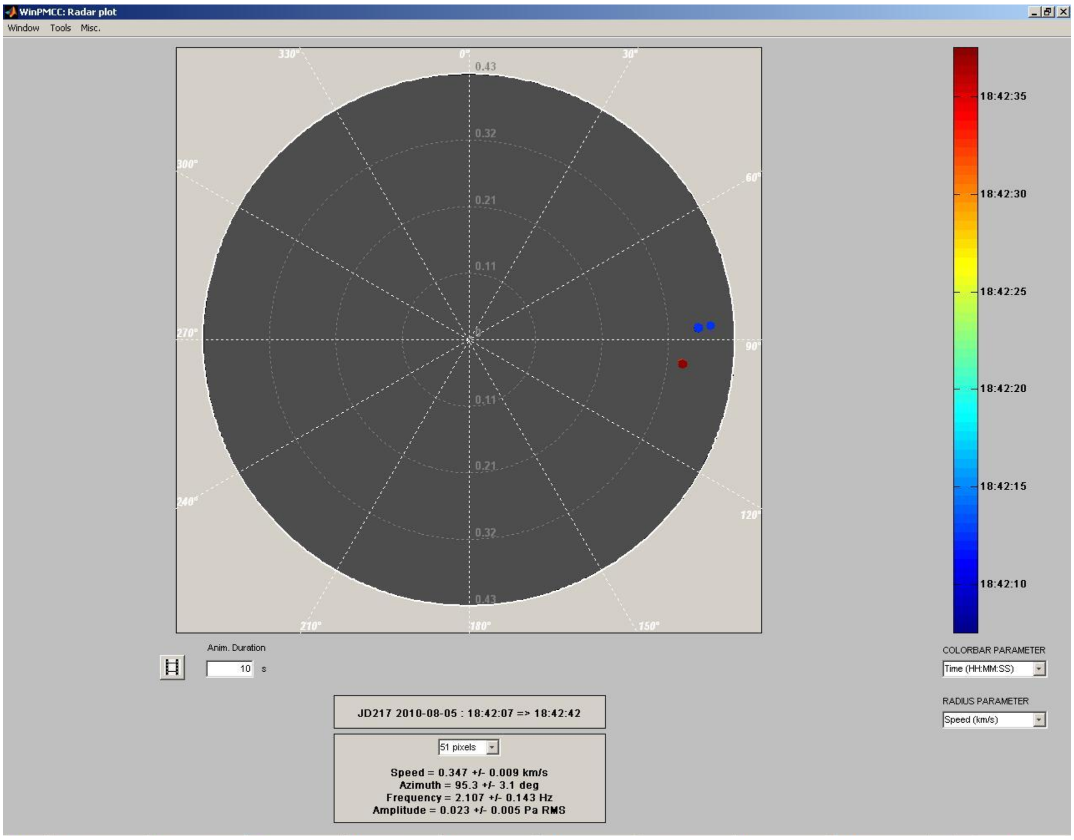

Anim. Duration 10 s

COLORBAR PARAMETER: Time (HH:MM:SS)

RADIUS PARAMETER: Speed (km/s)

```
JD217 2010-08-05 : 18:42:07 => 18:42:42
```

51 pixels

```
Speed = 0.347 +/- 0.009 km/s
Azimuth = 95.3 +/- 3.1 deg
Frequency = 2.107 +/- 0.143 Hz
Amplitude = 0.023 +/- 0.005 Pa RMS
```

Figure 10-3: Radar plot showing azimuth, speed and time of the arriving signals

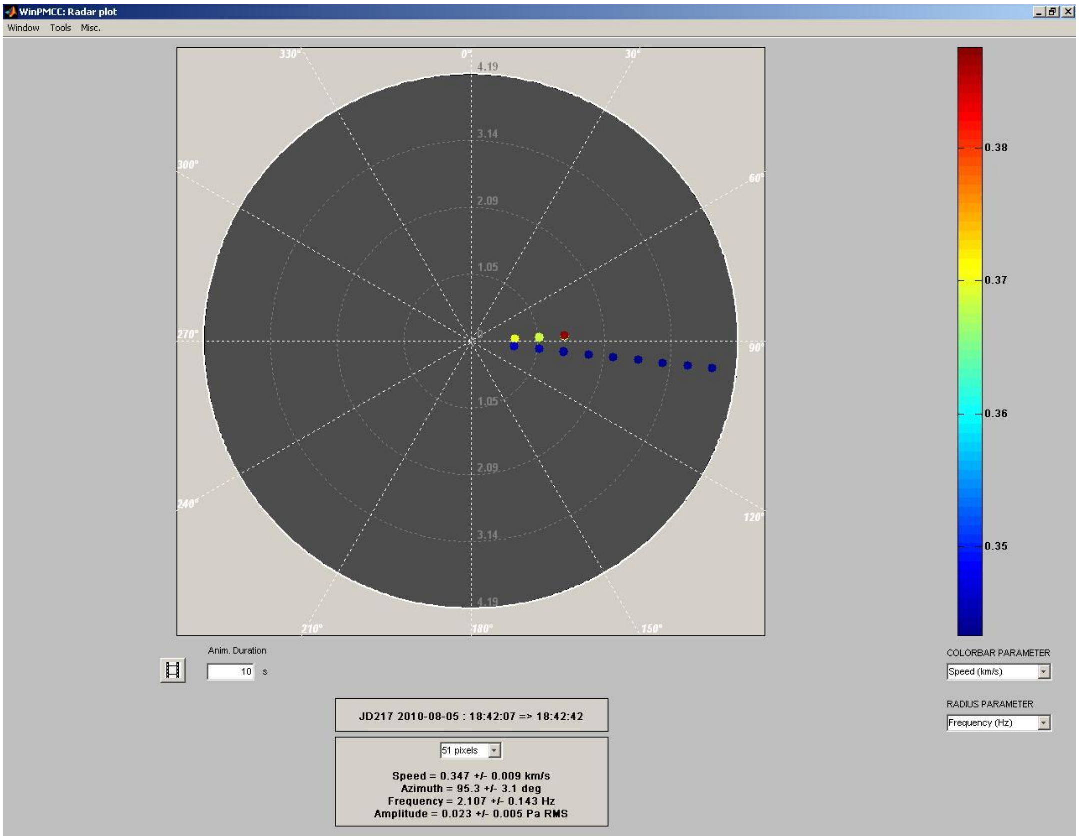

Anim. Duration 10 s

COLORBAR PARAMETER: Speed (km/s)

RADIUS PARAMETER: Frequency (Hz)

```
JD217 2010-08-05 : 18:42:07 => 18:42:42
```

51 pixels

```
Speed = 0.347 +/- 0.009 km/s
Azimuth = 95.3 +/- 3.1 deg
Frequency = 2.107 +/- 0.143 Hz
Amplitude = 0.023 +/- 0.005 Pa RMS
```

Figure 10-4: Radar plot showing azimuth, frequency and speed of the arriving signals

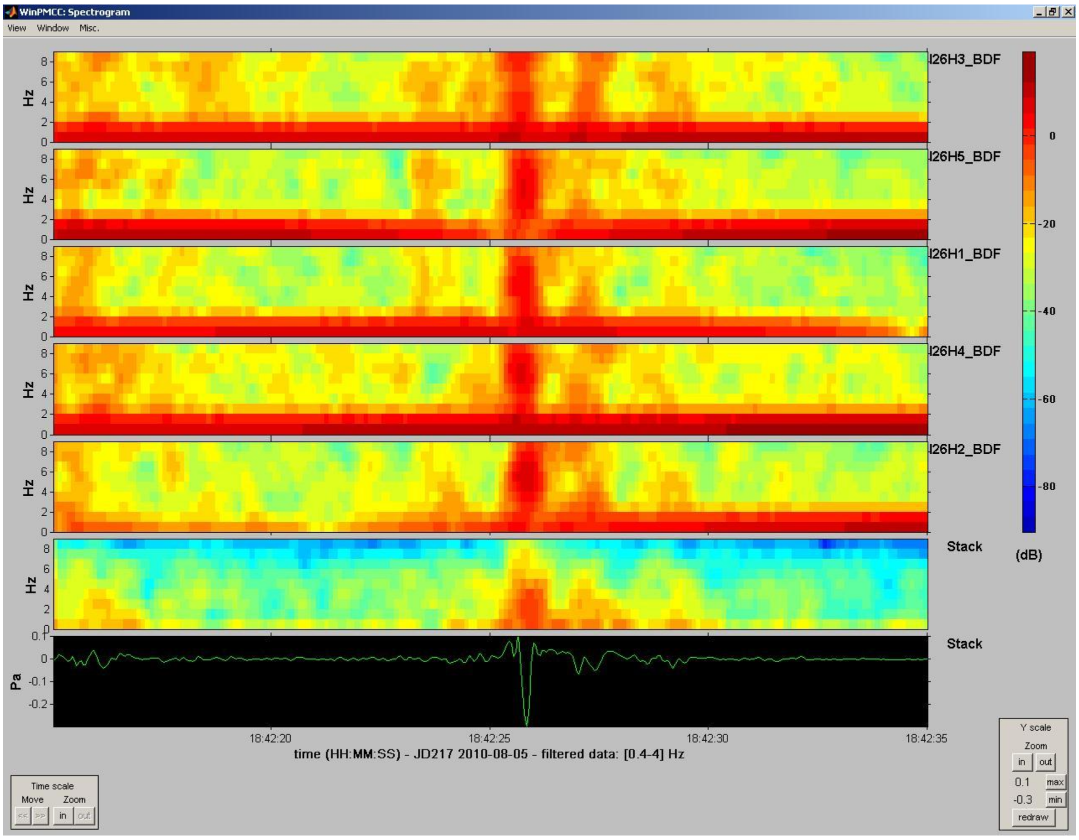

Figure 10-5: Spectrogram for signals from a single stroke flash

10.2. Multiple stroke CG flash

Figure 10-6 to *Figure 10-10* show IS signals produced by a flash with two strokes at a time interval of 115ms.

Table 4: Lightning parameters from ALDIS dataset for a flash containing 2 strokes

	Stroke 1	Stroke 2
Time (UTC)	13:34.27	13:34:27
Amplitude	26kA	-8kA
Distance	14.76km	14.11km
Azimuth	286.15°	287.25°
TOAmin (400m/s)	13:35:03.91	13:35:02.27
TOA (340m/s)	13:35:10.43	13:35:08.49
TOAmax (300m/s)	13:35:16.22	13:35:14.02

Figure 10-6 and *Figure 10-7* show the pressure variations generated by a CG flash containing two strokes. The time in between the strokes is long enough (>100ms at 20Hz sampling rate) to see two completely separated infrasonic rarefaction pulses without overlap. Although *Figure 10-8* indicates the signals arriving some seconds later than expected, the pulses appear to arrive right at the expected time in *Figure 10-6* and *Figure 10-7*. Maybe zooming into the radar plot shown in *Figure 10-8* would resolve this discrepancy. *Figure 10-9* shows two signals coming from two slightly different azimuths that are in good agreement with ALDIS azimuths. *Figure 10-10* illustrates the relatively low background noise and the IS signal standing our clearly from the background.

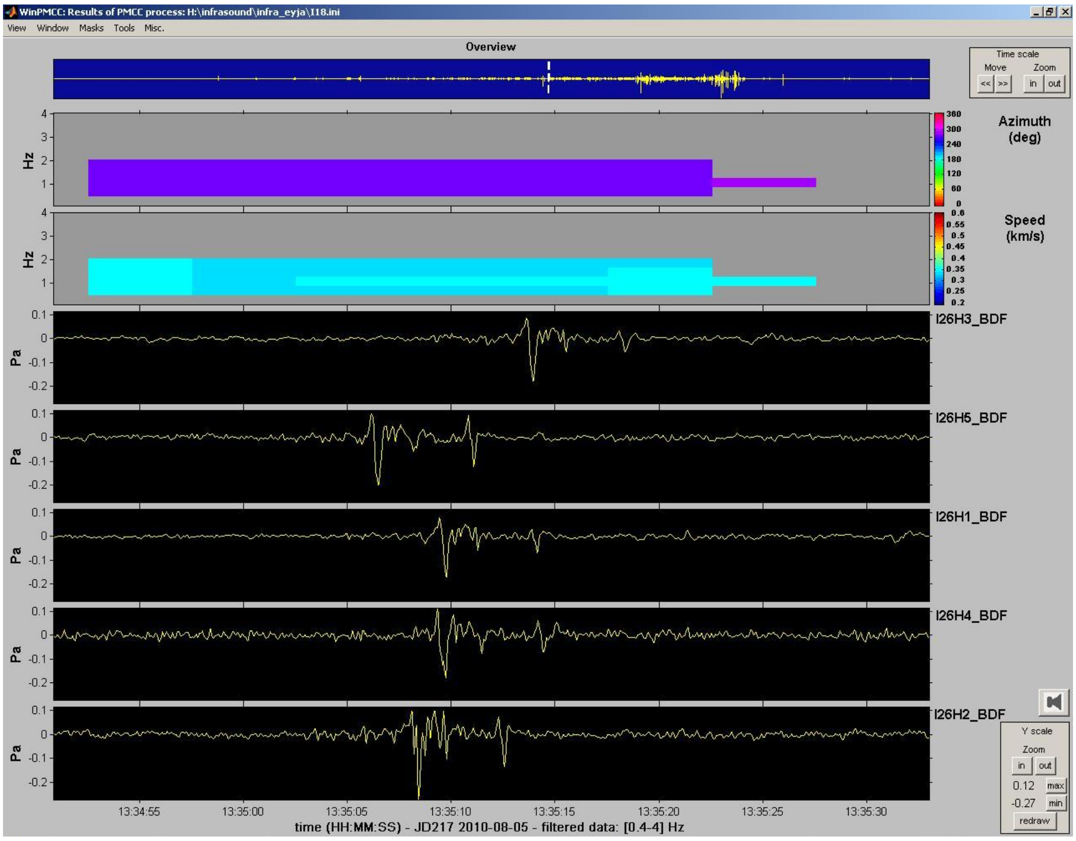

Figure 10-6: Pressure variations generated by a flash with two strokes

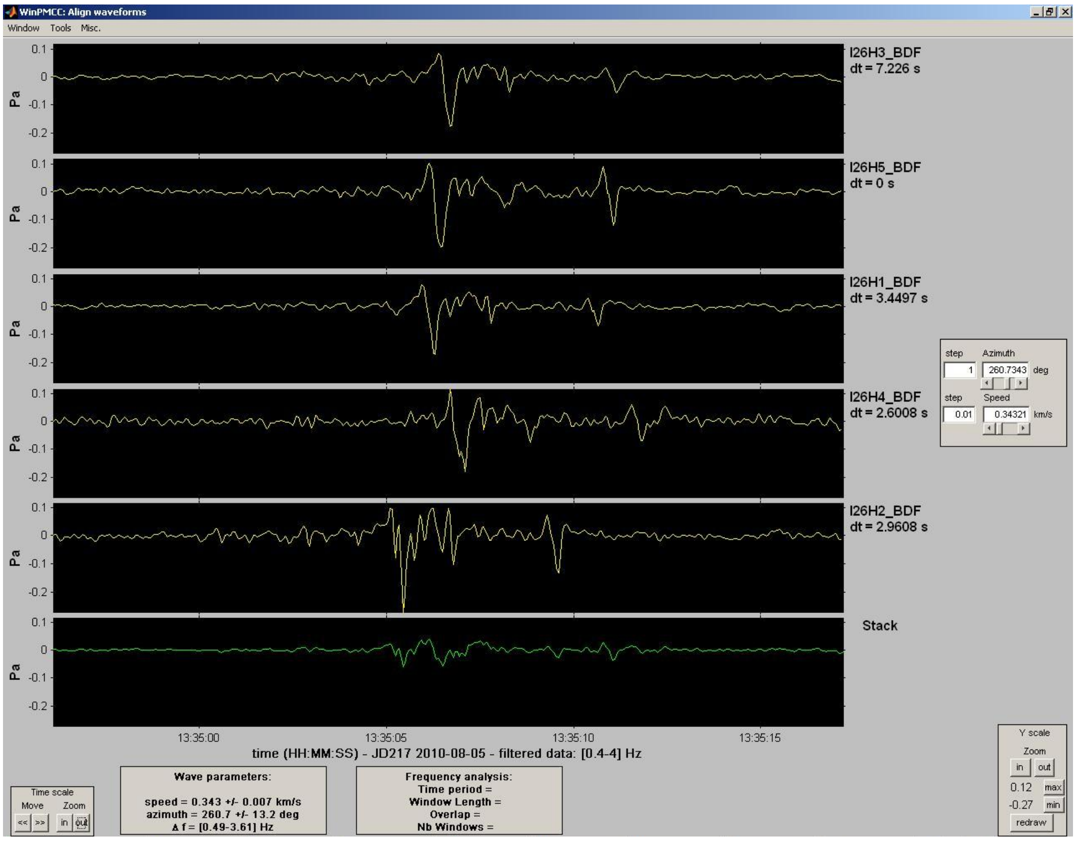

I26H3_BDF
dt = 7.226 s

I26H5_BDF
dt = 0 s

I26H1_BDF
dt = 3.4497 s

I26H4_BDF
dt = 2.6008 s

I26H2_BDF
dt = 2.9608 s

step 1
Azimuth 260.7343 deg

step 0.01
Speed 0.34321 km/s

time (HH:MM:SS) - JD217 2010-08-05 - filtered data: [0.4-4] Hz

Wave parameters:

speed = 0.343 +/- 0.007 km/s
azimuth = 260.7 +/- 13.2 deg
Δ f = [0.49-3.61] Hz

Frequency analysis:
Time period =
Window Length =
Overlap =
Nb Windows =

Y scale max 0.12
Y scale min -0.27

Figure 10-7: Time-aligned signals generated by a flash with two strokes

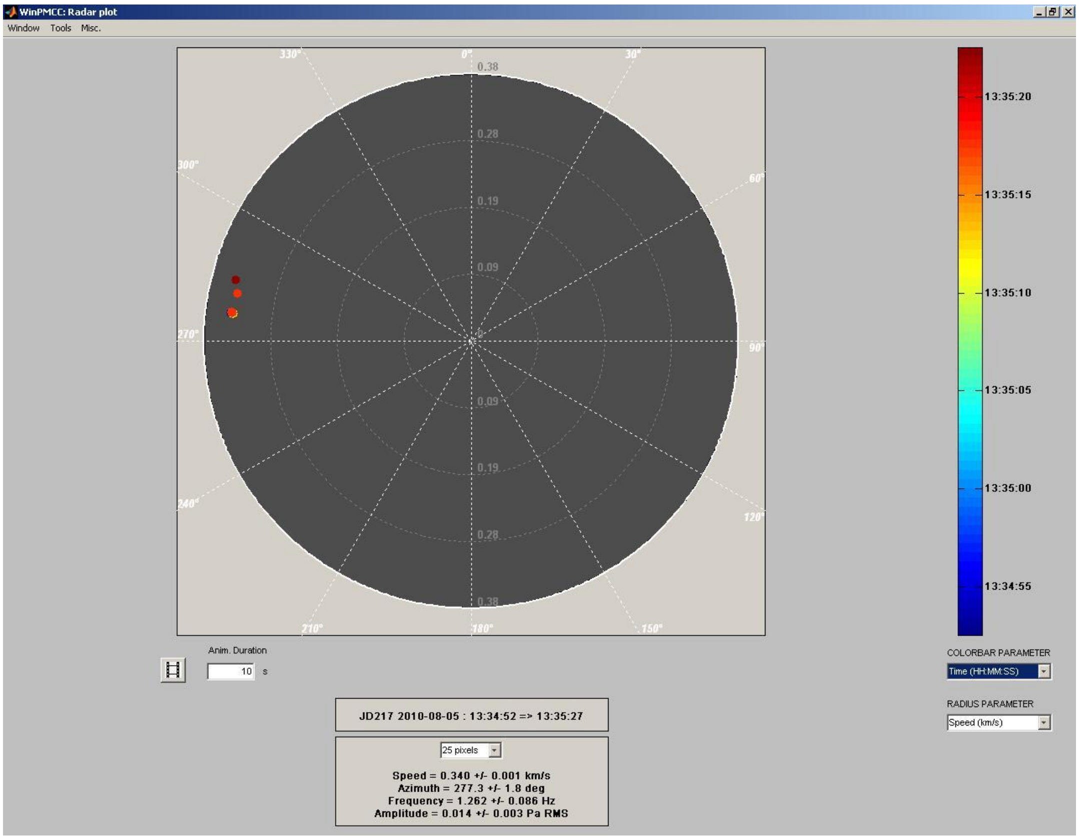

Anim. Duration 10 s

COLORBAR PARAMETER
Time (HH:MM:SS)

RADIUS PARAMETER
Speed (km/s)

JD217 2010-08-05 : 13:34:52 => 13:35:27

25 pixels

Speed = 0.340 +/- 0.001 km/s
Azimuth = 277.3 +/- 1.8 deg
Frequency = 1.262 +/- 0.086 Hz
Amplitude = 0.014 +/- 0.003 Pa RMS

Figure 10-8: Radar plot showing azimuth, speed and time of the arriving signals

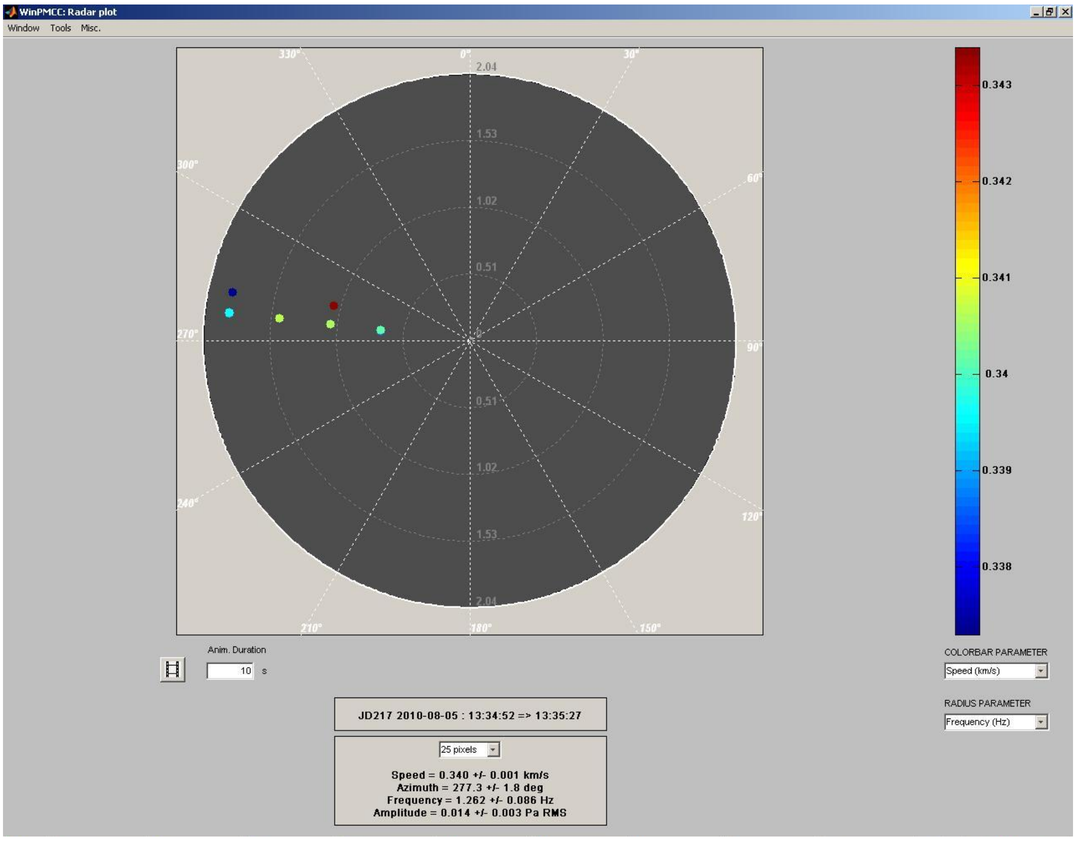

Anim. Duration 10 s

COLORBAR PARAMETER: Speed (km/s)

RADIUS PARAMETER: Frequency (Hz)

JD217 2010-08-05 : 13:34:52 => 13:35:27

25 pixels

Speed = 0.340 +/- 0.001 km/s
Azimuth = 277.3 +/- 1.8 deg
Frequency = 1.262 +/- 0.086 Hz
Amplitude = 0.014 +/- 0.003 Pa RMS

Figure 10-9: Radar plot showing azimuth, frequency and speed of the arriving signals

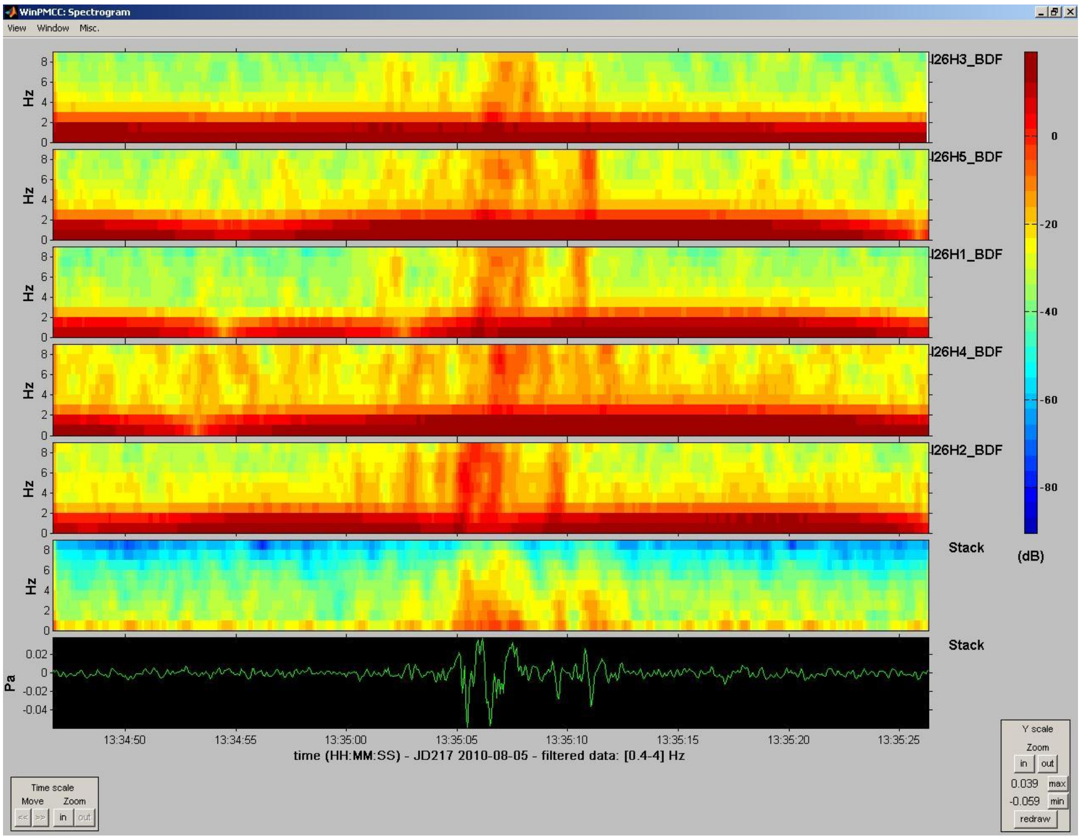

Y scale: 0.039 max, -0.059 min

Figure 10-10: Spectrogram for signals from a flash with two strokes

10.3. CC discharge

Figure 10-11 to *Figure 10-15* show IS signals produced by a CC discharge.

Table 5: Lightning parameters from ALDIS dataset for a CC discharge

Time (UTC)	16:55:07
Amplitude	-7kA
Distance	14.34km
Azimuth	241.80°
TOAmin (400m/s)	16:55:42.78
TOA (340m/s)	16:55:49:10
TOAmax (300m/s)	16:55:54.71

Figure 10-11 and *Figure 10-12* show the pressure variations generated by a CC discharge. There were only a few CC discharges included in the ALDIS dataset because the system rejected most of the CC discharges until summer 2011. The background noise level is much higher than it was for the single stroke flash and the flash with two strokes observed above. There is not only one sharp peak but a lot of pressure variations being clearly above noise level for a relatively long period of time. *Figure 10-15* shows various signals standing out clearly from the background.

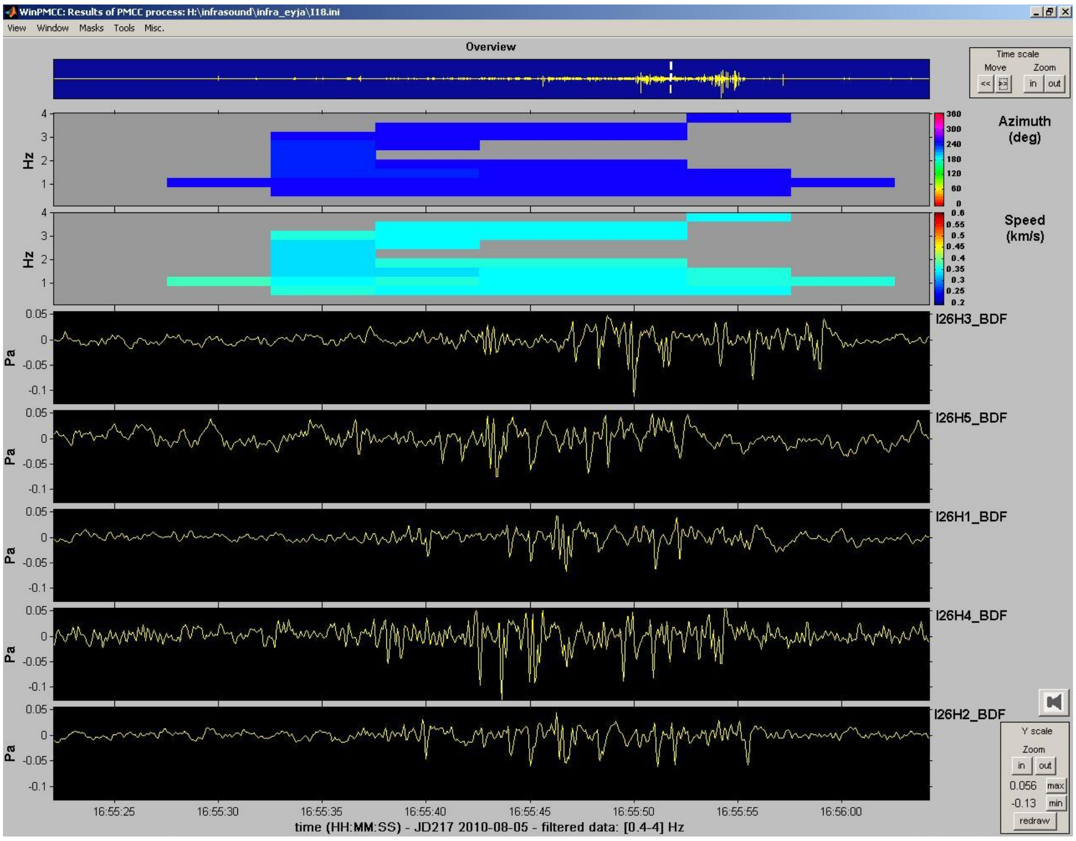

Figure 10-11: Pressure variations generated by a CC discharge

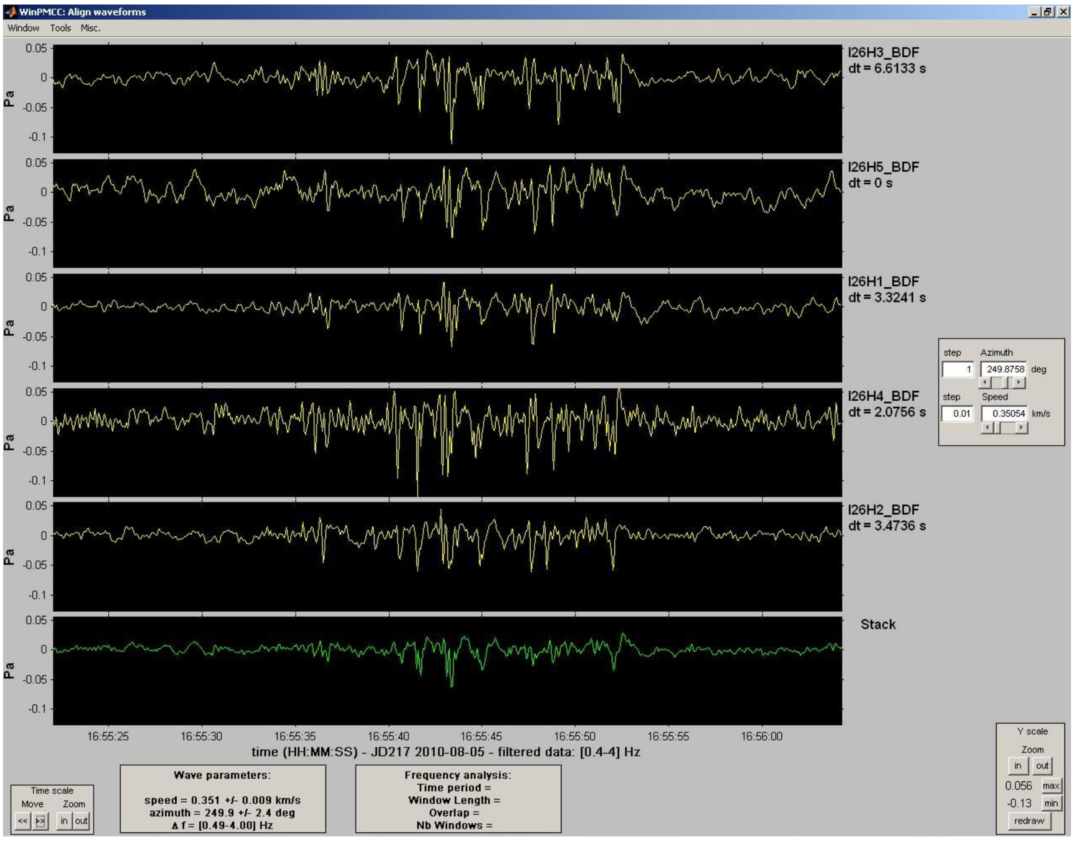

dt = 6.6133 s

dt = 0 s

dt = 3.3241 s

dt = 2.0756 s

dt = 3.4736 s

step 1 Azimuth 249.8758 deg

step 0.01 Speed 0.35054 km/s

time (HH:MM:SS) - JD217 2010-08-05 - filtered data: [0.4-4] Hz

Wave parameters:

speed = 0.351 +/- 0.009 km/s
azimuth = 249.9 +/- 2.4 deg
Δ f = [0.49-4.00] Hz

Frequency analysis:
Time period =
Window Length =
Overlap =
Nb Windows =

max 0.056
min -0.13

Figure 10-12: Time-aligned signals generated by a CC discharge

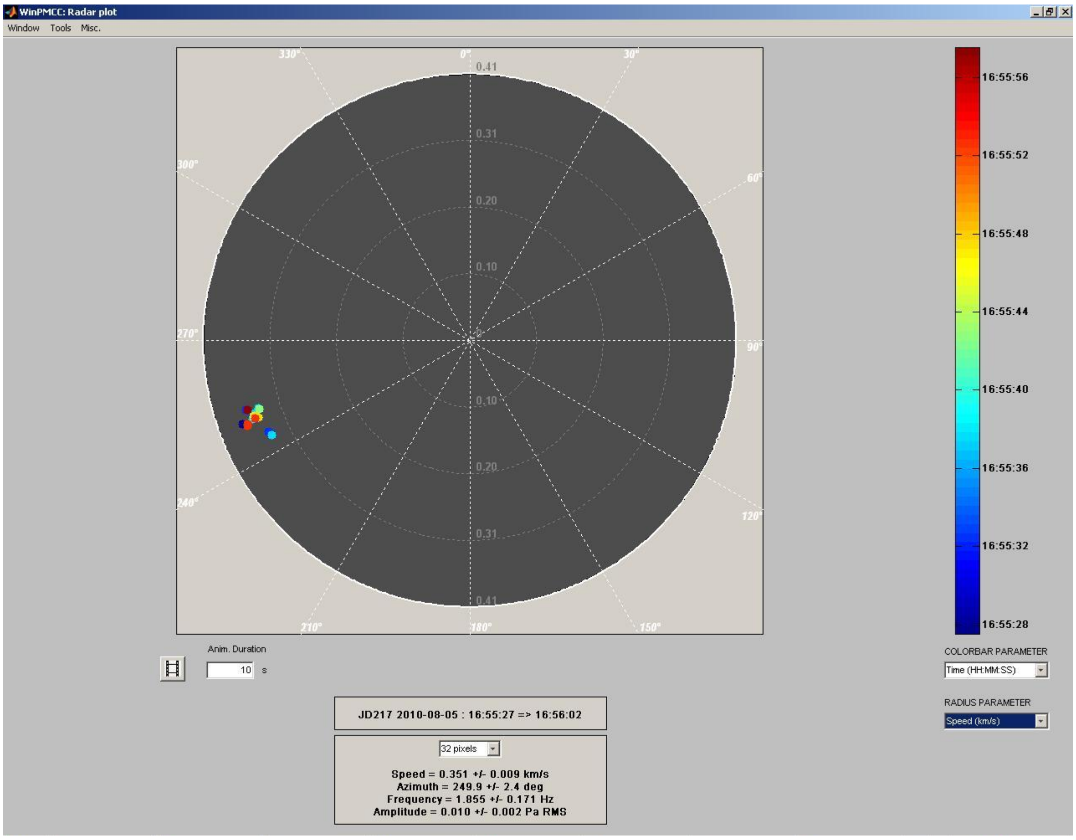

Anim. Duration 10 s

COLORBAR PARAMETER: Time (HH:MM:SS)

RADIUS PARAMETER: Speed (km/s)

JD217 2010-08-05 : 16:55:27 => 16:56:02

32 pixels

Speed = 0.351 +/- 0.009 km/s
Azimuth = 249.9 +/- 2.4 deg
Frequency = 1.855 +/- 0.171 Hz
Amplitude = 0.010 +/- 0.002 Pa RMS

Figure 10-13: Radar plot showing azimuth, speed and time of the arriving signals

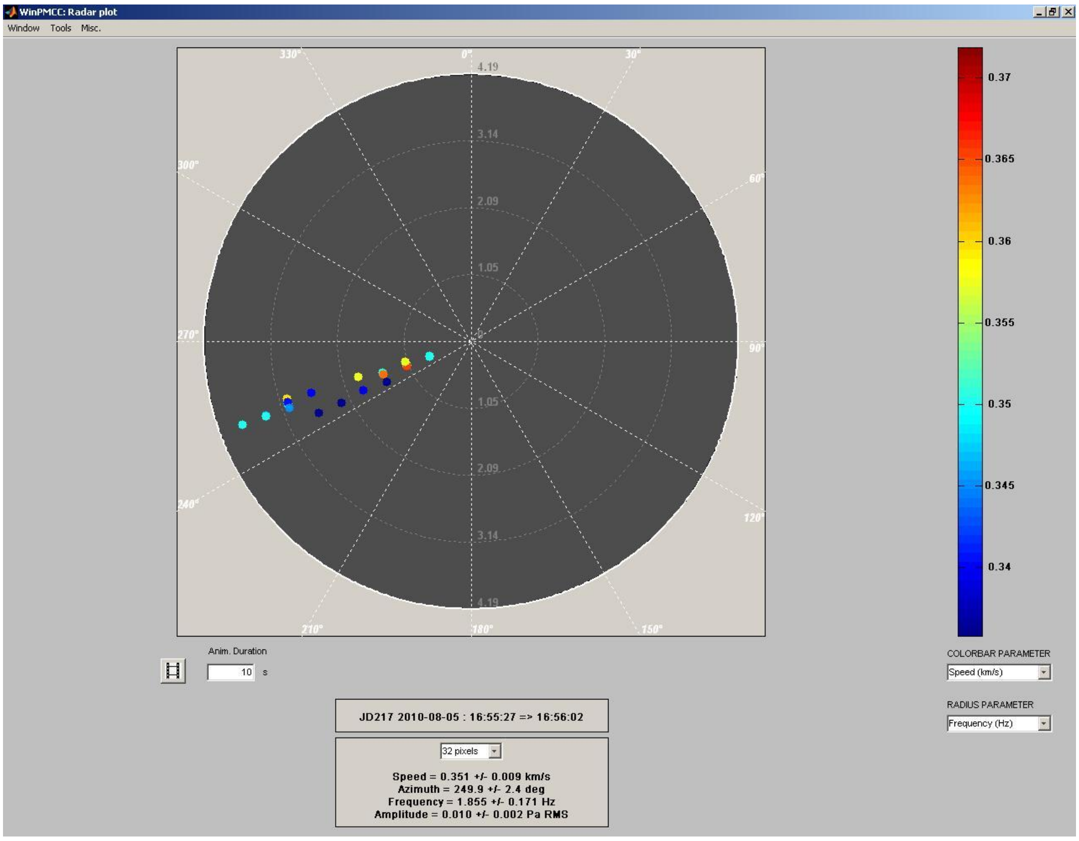

Anim. Duration 10 s

COLORBAR PARAMETER: Speed (km/s)

RADIUS PARAMETER: Frequency (Hz)

JD217 2010-08-05 : 16:55:27 => 16:56:02

32 pixels

Speed = 0.351 +/- 0.009 km/s
Azimuth = 249.9 +/- 2.4 deg
Frequency = 1.855 +/- 0.171 Hz
Amplitude = 0.010 +/- 0.002 Pa RMS

Figure 10-14: Radar plot showing azimuth, frequency and speed of the arriving signals

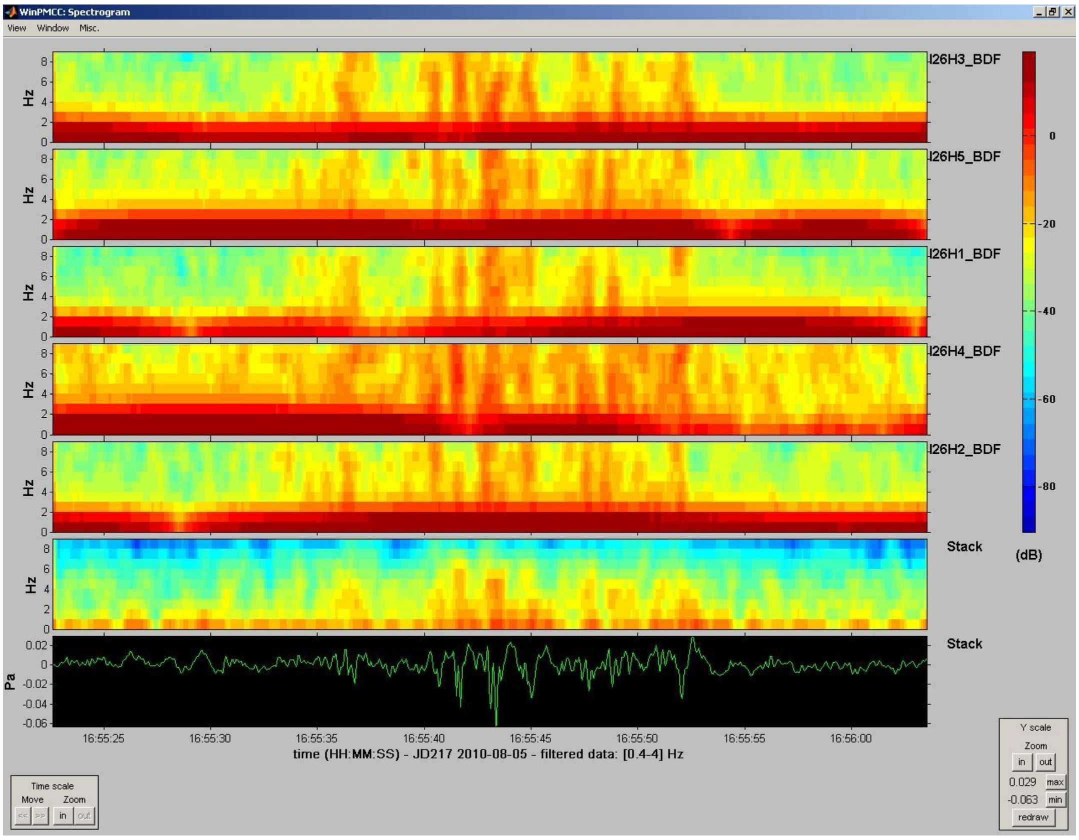

Figure 10-15: Spectrogram for signals from a CC discharge

Some additional observations of IS signals generated by single stroke CG flashes, multiple stroke CG flashes and CC flashes are given in the appendix.

10.4. Results

128 corresponding infrasonic signals from the 387 lightning strokes located by ALDIS within a radius of 50km around IS26 on August 5th 2010 could be recognized with PMCC, the other 259 lightning strokes could not be related to any infrasonic signal (*Figure 10-16*).

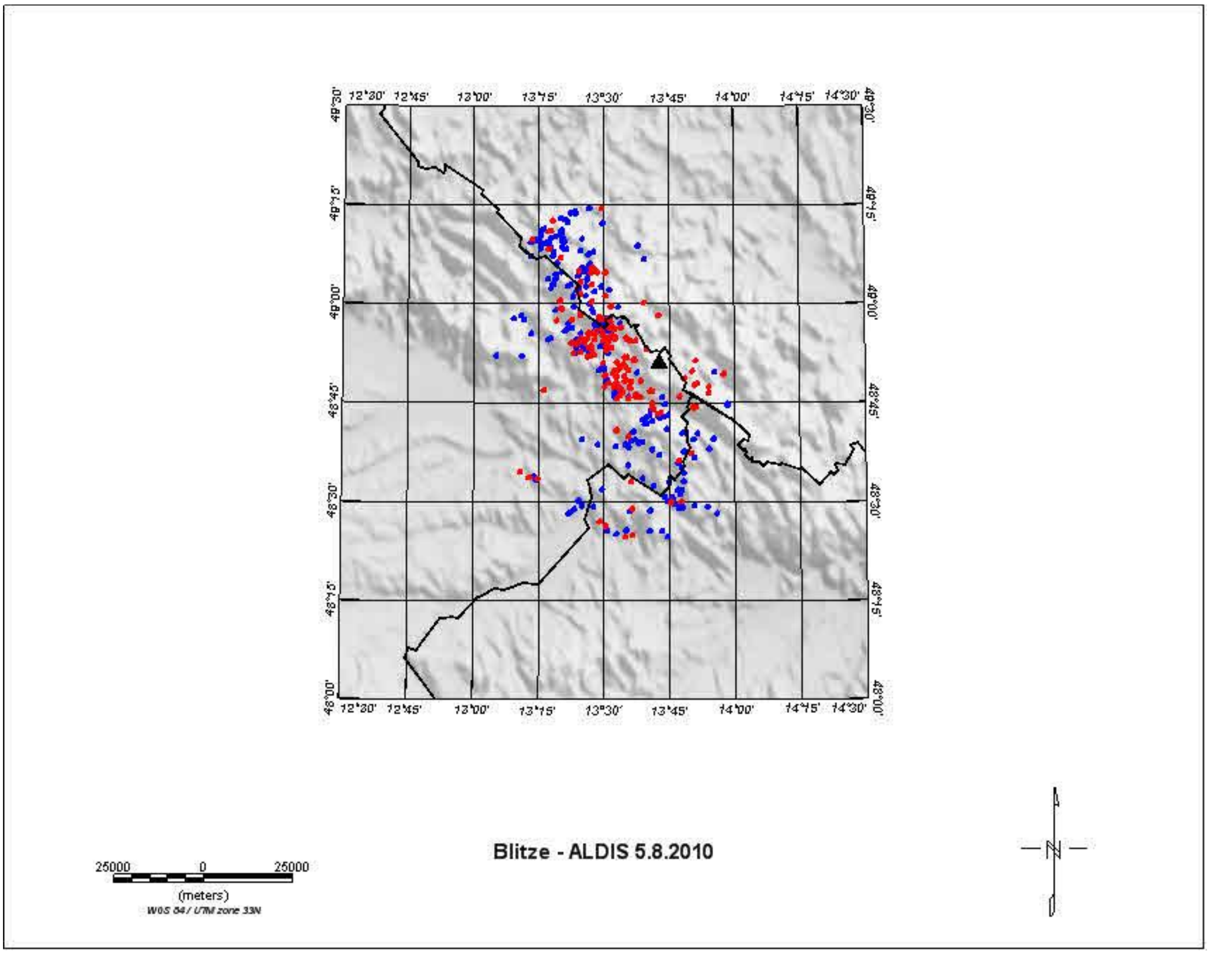

Figure 10-16: Location of Infrasound Station IS26 and located lightning on August 5th 2010 within a distance of 50km.

Red dots in *Figure 10-16* represent lightning strokes with corresponding IS signal, blue dots represent lightning strokes without corresponding IS signal, the triangle represents location of IS26. *Figure 10-16* shows a good detectability of infrasound produced by lightning for short distances. Further away from the array the number of detected IS signals decreases rapidly.

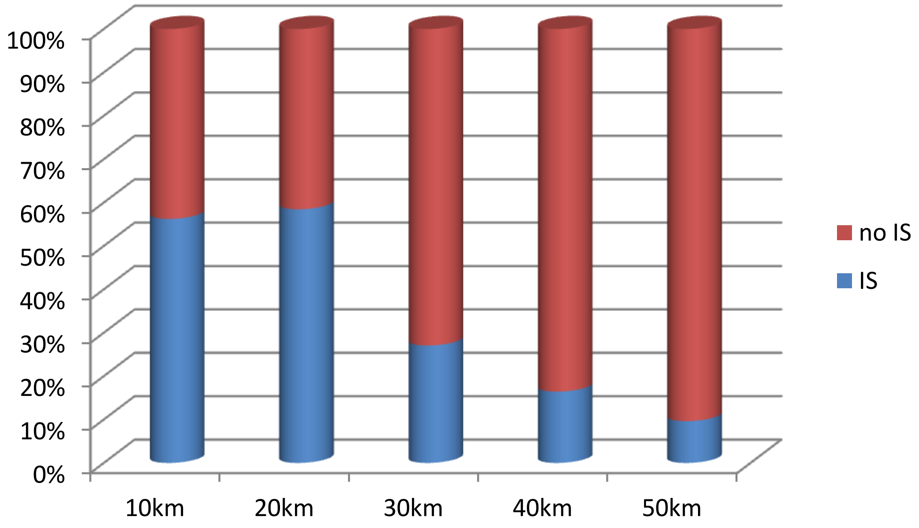

Figure 10-17: Detectability of IS depending on the distance to IS26

Figure 10-17 shows the number of flashes with detected and not detected corresponding IS signals. The detection of IS signals works well within a distance up to 20km. Further away from the station the number of detected infrasonic signals decreases rapidly.

There were 244 lightning strokes with negative current and 143 strokes with positive current. Altogether 387 lightning strokes were located by ALDIS, 63.05% negative ones and 36.95% positive ones. A short overview of ALDIS located strokes and corresponding IS detections is given in *Table 6*.

Table 6: ALDIS located strokes and corresponding IS signals for negative and positive current, respectively.

	Negative current	Positive current	Sum
ALDIS	244	143	387
Corresponding IS	80	48	128
Percentage	33	34	33

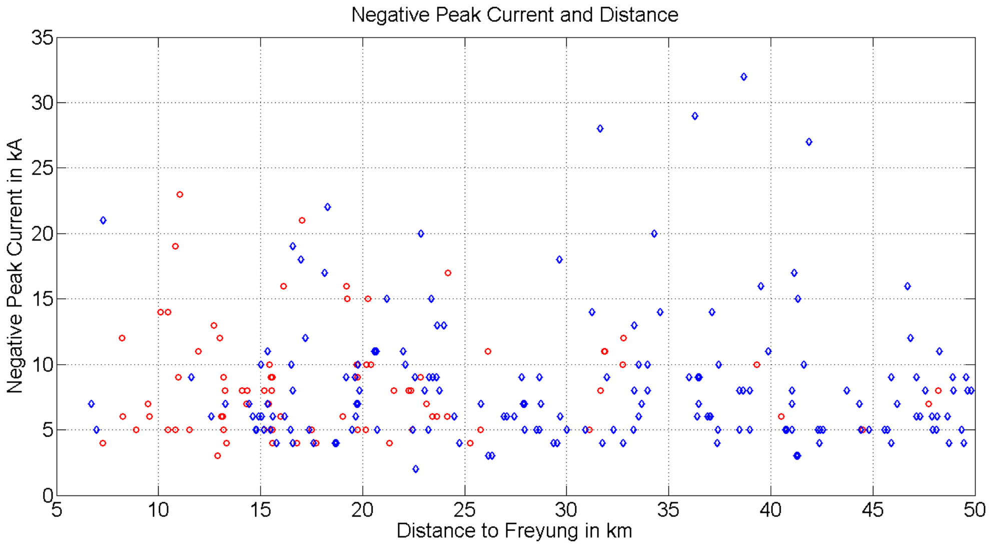

Figure 10-18: Negative peak current (ALDIS) and distance from IS26; red circles represent lightning strokes with corresponding IS signal, blue diamonds represent lightning strokes without corresponding IS signal.

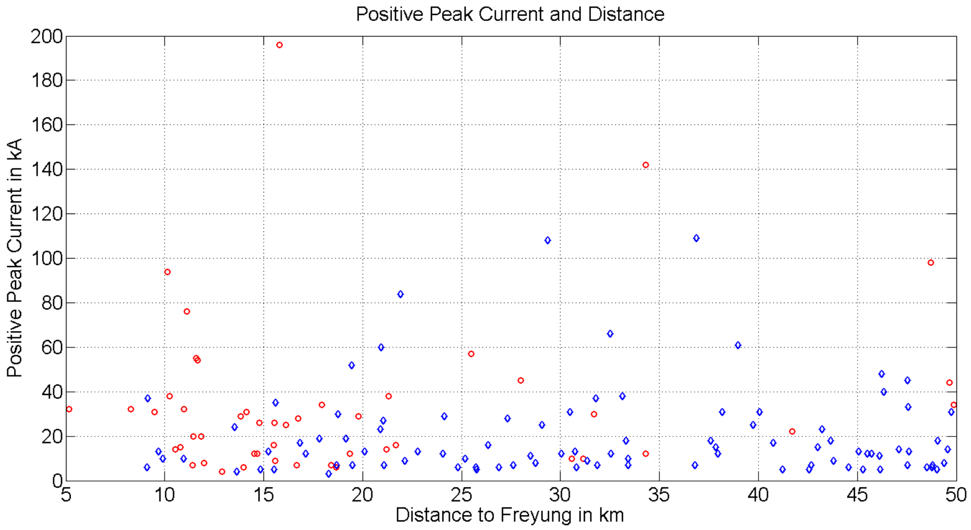

Figure 10-19: Positive peak current (ALDIS) and distance to IS26; red circles represent lightning strokes with corresponding IS signal, blue diamonds represent lightning strokes without corresponding IS signal.

Figure 10-19 shows the peak current of detected negative lightning strokes over the distance to IS26. The number of detected IS signals decreases rapidly for lightning strokes further away than 20-25km.

Figure 10-20 shows the peak current of detected positive lightning strokes over the distance to IS26. The number of detected IS signals decreases rapidly for lightning strokes further away than 20km.

ALDIS located strokes were classified based on peak current Î reported by ALDIS in 4 categories:

I. 0< |Î| <10kA

II. 10kA <= |Î| < 25kA

III. 25kA <= |Î| < 50kA

IV. |Î| >= 50kA

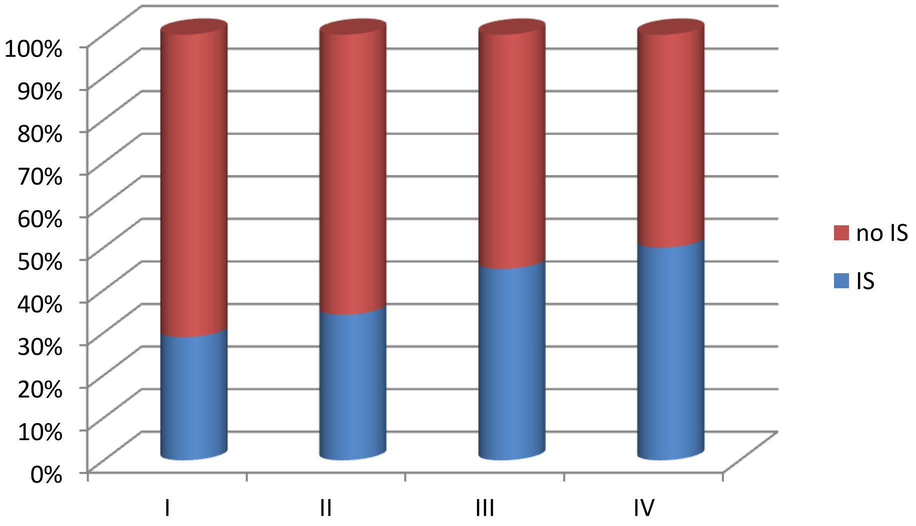

Figure 10-20: Categories of peak current as described above

Figure 10-20 shows the detectability of IS signals related to the categories of peak current as described above. Having a look at different strength of discharge (according to current amplitude) and the number of detected corresponding IS signals lead to the conclusion that the detectability of IS signals increases with increasing current of the discharge.

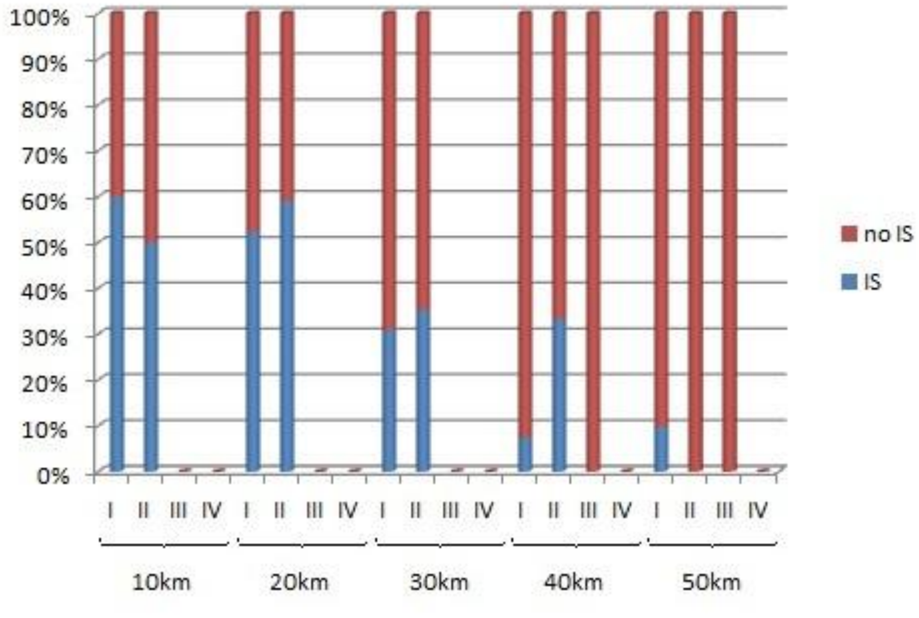

Figure 10-21: Detectability of IS signals depending on the distance and the categories of peak current for negative discharges

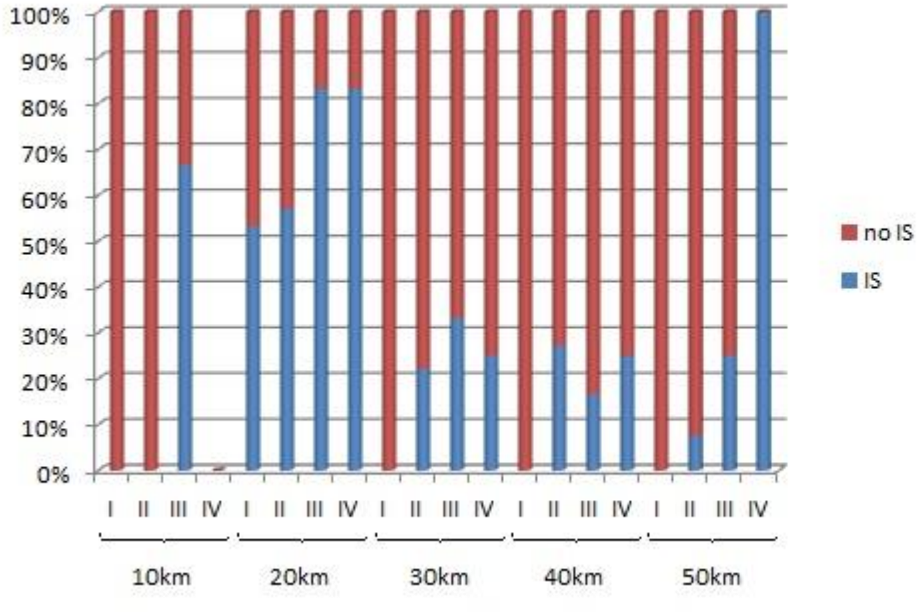

Figure 10-22: Detectability of IS signals depending on the distance and the categories of peak current for positive discharges

Figure 10-21 and *Figure 10-22* show the detectability of IS signals depending on the distance and the categories of peak current for negative and positive discharges, respectively. IS signals from positive lightning discharges within 20km from IS26 show very good detectability, especially for high current discharges (category III and IV). Beyond 20km from IS26 the detectability decreases for both negative and positive discharges. 100% detectability for positive discharges of category IV 50km away from IS26 is because there was only one discharge to consider and this one was detected.

In a further step strokes with corresponding IS signal were divided into three categories:

a) Significant pressure variation, azimuth agrees closely (+/-10deg) to ALDIS azimuth

b) Significant pressure variation, azimuth does not agree to ALDIS azimuth

c) No significant pressure variation, azimuth agrees closely to ALDIS azimuth

On the pressure over time screenshots as shown in *Figure 9-6* the peak-to-peak value of the infrasonic signals was measured with a ruler as shown in *Figure 10-23*. The measurement was possible for IS signals of type a) and b) but not for signals of type c).

Some of the observed infrasonic signals were too close to each other to separate them. Those signals were not considered in the following evaluation. 59 signals of type a) and 11 signals of type b) remain to be considered in the following figures.

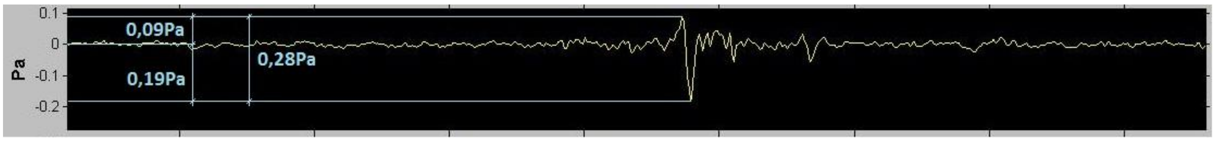

Figure 10-23: Measuring peak-to-peak pressure

Table 7: Dataset consisting of lightning parameters and associated IS parameters

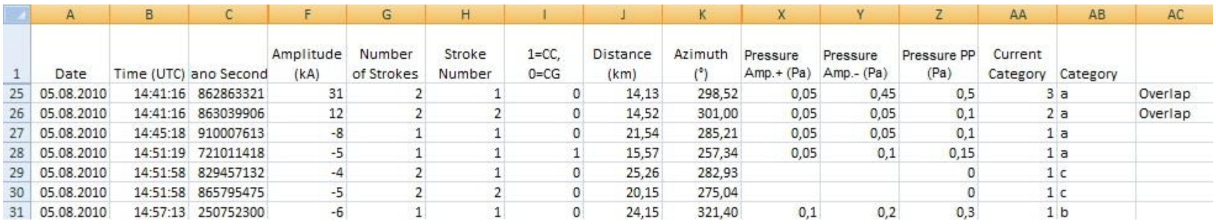

	A	B	C	F	G	H	I	J	K	X	Y	Z	AA	AB	AC
1	Date	Time (UTC)	ano Second	Amplitude (kA)	Number of Strokes	Stroke Number	1=CC, 0=CG	Distance (km)	Azimuth (°)	Pressure Amp.+ (Pa)	Pressure Amp.- (Pa)	Pressure PP (Pa)	Current Category	Category	
25	05.08.2010	14:41:16	862863321	31	2	1	0	14,13	298,52	0,05	0,45	0,5	3	a	Overlap
26	05.08.2010	14:41:16	863039906	12	2	2	0	14,52	301,00	0,05	0,05	0,1	2	a	Overlap
27	05.08.2010	14:45:18	910007613	-8	1	1	0	21,54	285,21	0,05	0,05	0,1	1	a	
28	05.08.2010	14:51:19	721011418	-5	1	1	1	15,57	257,34	0,05	0,1	0,15	1	a	
29	05.08.2010	14:51:58	829457132	-4	2	1	0	25,26	282,93			0	1	c	
30	05.08.2010	14:51:58	865795475	-5	2	2	0	20,15	275,04			0	1	c	
31	05.08.2010	14:57:13	250752300	-6	1	1	0	24,15	321,40	0,1	0,2	0,3	1	b	

Column “A” to column “K” show lightning parameters from ALDIS dataset as described in 5.2. Column “X” and column “Y” show the positive and negative pressure amplitude, respectively, measured as shown in *Figure 10-23*. Column “Z” is the measured peak-to-peak pressure of the infrasound signal. The classification of the current amplitude of the lightning discharge (column “F”) as described above is represented in column “AA”. Column “AB” shows the categories of the quality of the infrasound signal as described above. The comment “Overlap” in column “AC” indicates that the time in between the strokes of a multiple stroke flash was too short (<100ms) to separate the associated infrasound signals.

Figure 10-24 and *Figure 10-26* show the relation between the measured peak-to-peak pressure, distance to IS26 and peak current from ALDIS database for category a) signals.

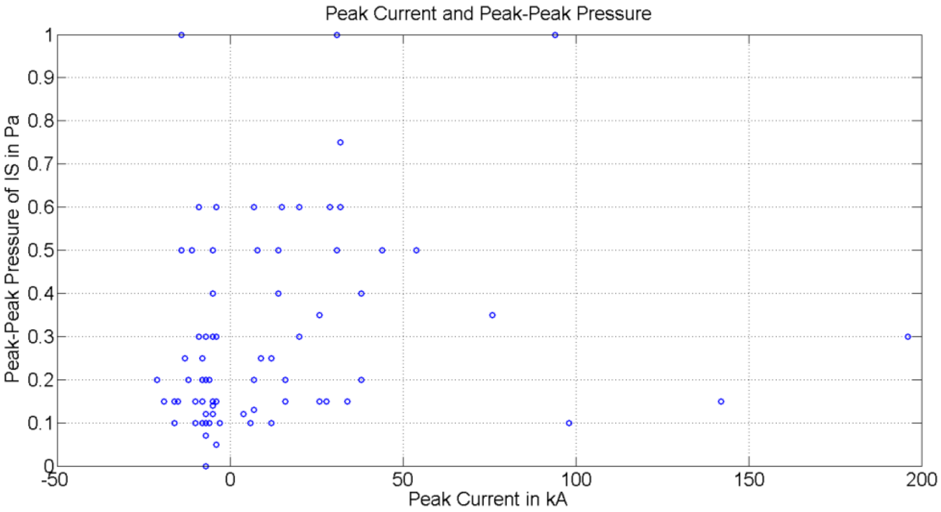

Figure 10-24: Relation between peak-to-peak pressure and peak current for category a) IS signals

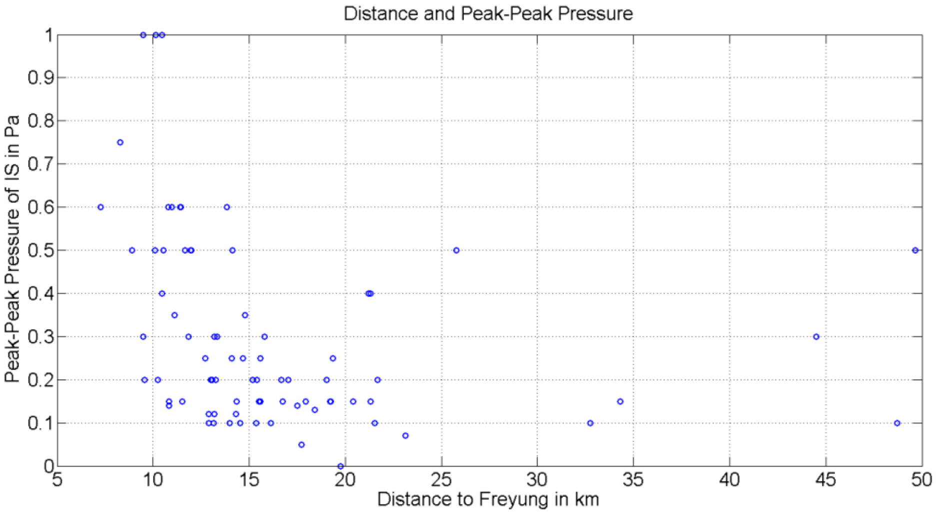

Figure 10-25: Relation between peak-to-peak pressure and distance for category a) IS signals

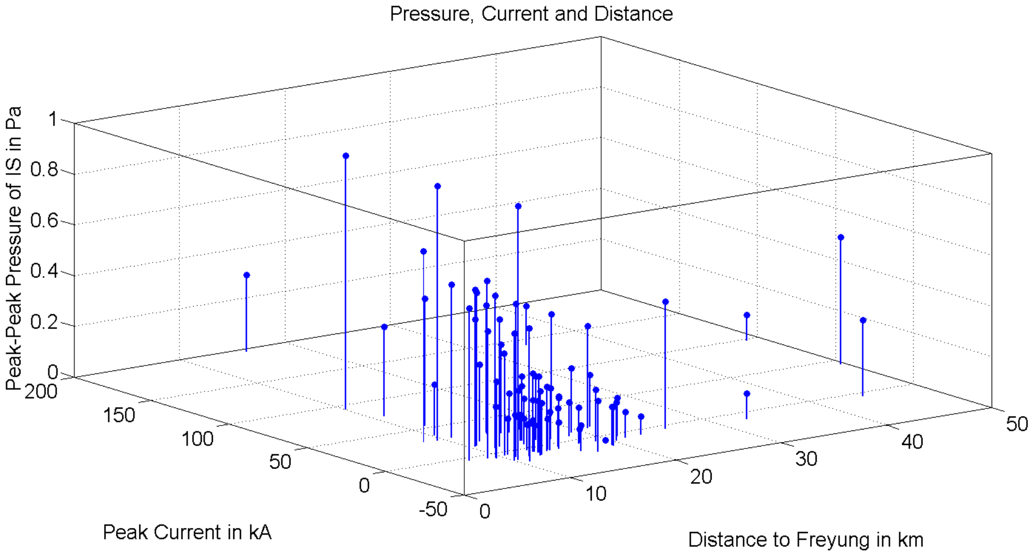

Figure 10-26: 3D plot of the relation between peak-to-peak pressure, distance and peak current for category a) IS signals

Figure 10-27 and *Figure 10-29* show the relation between the measured peak-to-peak pressure, distance to IS26 and peak current from ALDIS Database for category b) signals.

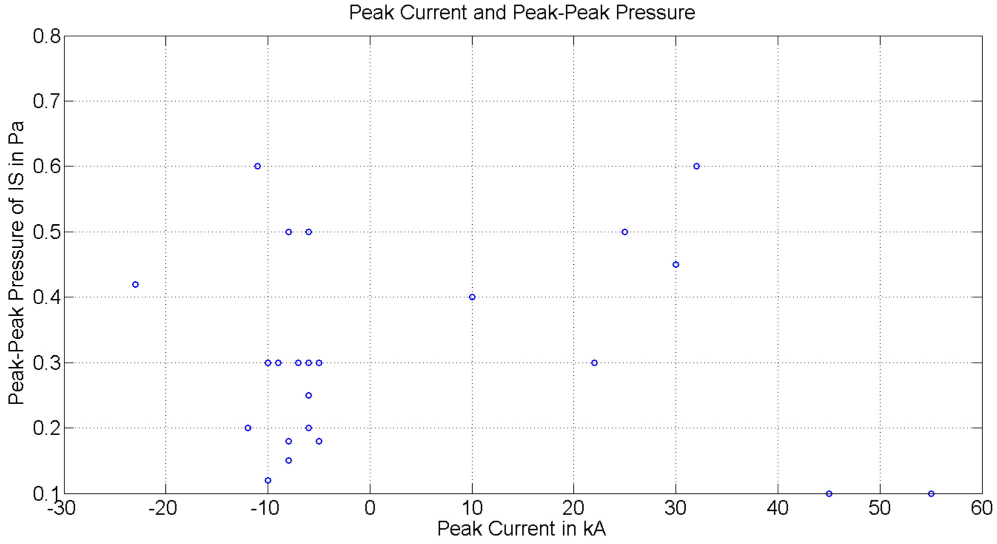

Figure 10-27: Relation between peak-to-peak pressure and peak current for category b) IS signals

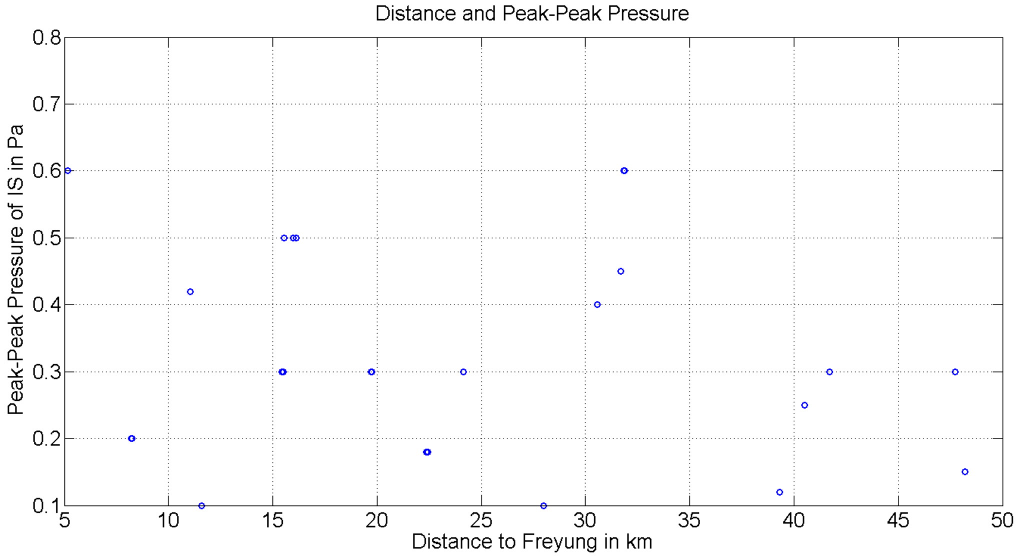

Figure 10-28: Relation between peak-to-peak pressure and distance for category b) IS signals

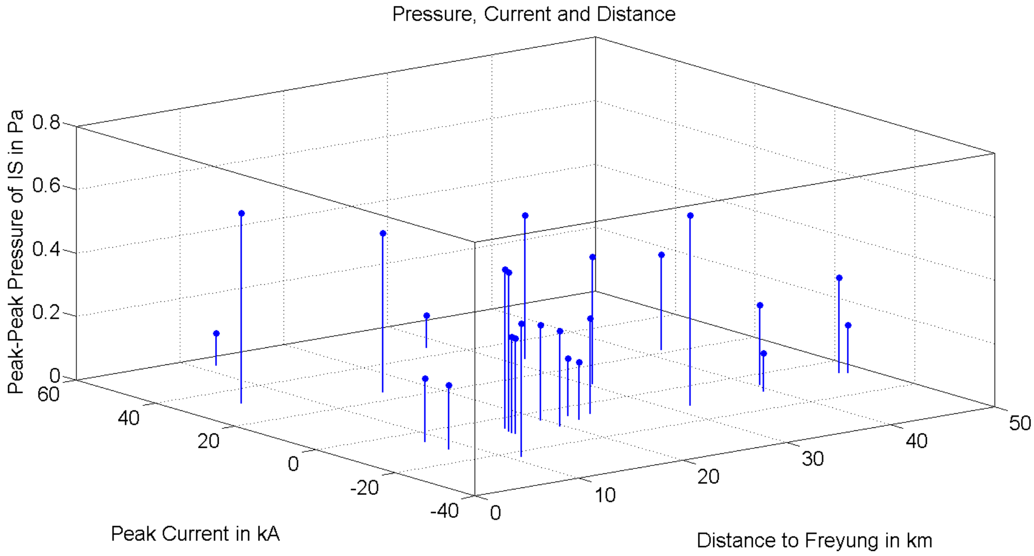

Figure 10-29: 3D plot of the relation between peak-to-peak pressure, distance and peak current for category b) IS signals

Figure 10-24 to *Figure 10-29* show relations between discharge current, measured peak-to-peak pressure of the infrasound signal and distance for category a) and b) signals, respectively. There were no obvious relations between the three parameters. *Figure 10-25* indicates a decaying trend of the peak-to-peak pressure with distance although there are still some IS signals with high pressure coming from long distance (40-50km). Because of few category b) signals a statement on the behavior of those signals is not supposed to be significant.

11. Conclusion

Obviously from *Figure 8-2*, *Figure 8-3* and *Figure 8-4* at Conrad Observatory were no signals in the infrasonic range showed any amplitudes significant higher than the background noise level of the two elements. Because they were mainly designed to investigate the wind noise reduction of different geometries and therefore they are not located in an area with very low noise the infrasonic signals produced by lightning discharges could easily be overwhelmed by the wind noise. For that reason data from the IS station at CO cannot be used for the analysis of lightning produced infrasound signals and data from a fully operational IS station with several array elements allowing more sophisticated signal processing as described in 7.3 are required.

In the next chapter data from IS26 Freyung, an operational IS station of the IMS, was used to examine possible correlations between lightning flashes and recorded signals.

Data from Station IS26 (Freyung) provided good results for observing infrasonic signals produced by lightning discharges. About one third of the flashes from the ALDIS dataset could be related to infrasonic signals. The evaluation did not yield obvious relations between current, distance to the station and the pressure amplitude, but it was shown that the detectability of IS signals produced by lightning discharges increases with lightning current and delivers good results within a radius of 20km around the station.

There were various infrasonic signals detected at IS26 which were looking like lightning associated signals, but there were no corresponding flashes in the ALDIS dataset. Those signals could be generated by CC flashes that were rejected by the ALDIS LLS in 2010 because the system was concipated mainly for the detection of CG flashes. Since summer 2011 ALDIS has has been running the LLS with updated detection criteria and more detections of CC flashes are available. Therefore further investigations should be made on this object. As well infrasound generated by lightning at the radio tower (Gaisberg) seems an interesting object to study, because direct current measurements which allow the calculation of lightning charges, is available. Comparing the charge and the associated infrasonic signal could lead to further information about the generation of the signal.

12. Summary

The first part of this work consists of important theoretical background about the lightning discharge and the generation of sound from lightning. An overview of two theories concerning the generation of sound and infrasound, acoustic radiation from hot channels and electrostatic acoustic emission, is given as well as an overview of propagation effects on acoustic signals. A short description of experiments that have been conducted is also included in the first part of this work.

The second part of this work deals with the considered data and the cooperation partners providing the data. A short overview of the organizations and their field of functions is given and the methods for gathering and processing the data used throughout this work are described.

- Lightning Location System operated by ALDIS, lightning data provided by ALDIS,
- Infrasound Stations of the International Monitoring System operated by CTBTO,
- Conrad Observatory operated by ZAMG, infrasound data provided by ZAMG.

The last part of this work is about the evaluation of observed datasets. Software tools to handle the data are described and examples of signals in the IS range are given for both locations of interest (Conrad Observatory and IS26 Freyung). Examples of signals from different sources (single stroke CG flash, multiple stroke CG flash and CC discharge) are shown and analyzed. The relation between the detectability of IS from lightning and distance from the source to the array shows that more than 50% of the lightning strokes located by ALDIS could be associated to an IS signal within a radius of 20km. Furthermore it was shown that the detectability of IS signals increases with increasing current of the lightning discharge.

More examples of IS signals from lightning discharges are given in the appendix. Signals from single stroke CG flashes, multiple stroke CG flashes and CC discharges are shown with their Radar Plots, Align Waveform Plots and Spectrograms.

In future studies, investigations on the behavior and characterization of IS generated by CC discharges seem to be an interesting object as well as infrasound generated by lightning to the Gaisberg radio tower. The latter could lead to further information about the generation of the signal.

Literature

ALDIS. 2011. ALDIS - Austrian Lightning Detection & Information System. [Online] 2011. [Cited: 09 20, 2011.] http://www.aldis.at/.

Assink, J.D., et al. 2008. Characterization of infrasound from lightning. *Geophysical Research Letters.* 2008, Vol. 35.

Balachandran, N. K. 1979. Infrasonic signals from thunder. *Journal of Geophysical Research.* 1979, Vol. 84, 1735-1745.

Barry, R. G. and Chorley, R. J. 1998. *Atmosphere, weather and climate.* London and New York : Routledge, 1998.

Bohannon, J. L. 1980. Infrasonic Thunder: Explained. *Ph.D. thesis.* Houston, Texas : Rice University, 1980.

Bohannon, J. L., Few, A. A., Dessler, A. J. 1977. Detection of infrasonic pulses from thunderclouds. *Geophysical Research Letters.* 1977, Vol. 4, 49-52.

Bohannon, J.L. 1978. Infrasonic pulses from thunderstorms. *M.S. thesis.* Houston, Texas : Rice University, 1978.

Boulder Real Time Technologies. 2011. http://www.brtt.com. [Online] 2011. [Cited: 07 18, 2011.] http://www.brtt.com/software.html.

Brode, H. L. 1956. *The Blast Wave in Air Resulting from a High Temperatur, High Pressure Sphere of Air.* Santa Monica, CA : Rand Corp., 1956. Vols. RM-1825-AEC.

Cansi, Y. and Le Pichon, A. 2003. *PMCC Progressive Multi-Channel Correlation.* s.l. : CEA/DASE, 2003.

CEA/DAM. 2009. Expertise. [Online] 2009. [Cited: 10 10, 2011.] http://www-dase.cea.fr/public/dossiers_thematiques/microbarometres/description_en.html.

CIGRE. 2000. *Cloud-to-ground lightning parameters derived from lightning location systems.* 2000.

Conrad Observatory. 2010. http://www.conrad-observatory.at/. [Online] 2010. [Cited: 07 18, 2011.] http://www.conrad-observatory.at/cmsjoomla/index.php?option=com_phocadownload&view=category&id=3%3Acobs-info&Itemid=78&lang=de.

CTBTO. 2011. [Online] 2011. [Cited: 08 04, 2011.] www.ctbto.org.

Dessler, A. J. 1973. Infrasonic thunder. *Journal of Geophysical Research.* 1973, Vol. 78, 1889-1896.

Few, A. A. 1995. Acoustic Radiations from Lightning. [book auth.] Hans Volland. *Handbook of atmospheric electrodynamics.* s.l. : Crc Pr Inc, 1995, Vol. Volume II.

Fleagle, R. G. and Businger, J. A. 1980. *An introduction to atmospheric physics.* s.l. : Academic Press, 1980.

Hill, R. D. 1979. A survey of lightning energy estimates. *Rev. Geophys. Space Phys.* 1979.

—. 1971. Channel heating in return stroke lightning. *Jounal of Geophysical Research.* 1971, Vol. 76, 637.

Holleman, I., et al. 2006. *Validation of an operational lightning detection system.* Tucson, Arizona, USA : s.n., 2006.

Holmes, C. R., Brook M., Krehbiel P., MrCrory R. 1971. On the power spectrum and mechanism of thunder. *Journal of Geophysical Research.* 1971, Vol. 76, 2106-2115.

Le Pichon, A., Blanc, E. and Hauchecorne, A. 2010. *Infrasound Monitoring for Atmospheric Studies.* Dordrecht, Heidelberg, London, New York : Springer, 2010. ISBN 978-1-4020-9507-8.

Plooster, M. N. 1968. *Shock Waves from Line Sources.* Boulder, CO : National Center for Atmospheric Research, 1968. NCAR-TN-37.

Pouillot, C., Chavy C., Quicke G. 2008. *WinPMCC User Manual.* 2008.

Sakurai, A. 1954. On the propagation and structure of the blast wave. II. *Journal of the Physical Society of Japan.* 1954, Vol. 9, p. 256.

Uman, M. A. 1971. Comparison of lightning and a long laboratory spark. *Proceedings of the IEEE.* 1971, Vol. 59, 4.

Uman, M.A. 1987. *The lightning discharge.* Orlando : Academic Press, 1987. ISBN 0-486-41463-9.

Uman, M.A. 1984. *Lightning.* New York : Dover, 1984. ISBN 0-486-64575-4.

Uman, M.A., Cookson, A.H., Moreland, J.B. 1970. Shock wave from a four-meter spark. *J. Appl. Phys.* 1970, Vol. 41, 3148.

Uman, Martin A. 2001. *The lightning discharge.* Mineola, New York : Dover Publications, Inc., 2001.

Wallace, J. M., Hobbs, P. V. 1977. *Atmospheric Science: An Introductory Survey.* s.l. : Academic Press, 1977.

Wikipedia. 2010. Shock wave. [Online] 07 07, 2010. [Cited: 07 26, 2010.] http://en.wikipedia.org/wiki/Shock_wave.

—. 2010. Speed of Sound. [Online] 2010. [Cited: 12 01, 2010.] http://en.wikipedia.org/wiki/Speed_of_sound.